D8-PRODUCT VALIDATION REPORT V2

WORLD EMISSION

Prepared by:	KAYRROS, LSCE, MPIC, ULB, GMV, BSC, CYI
Approved by:	Romain Vadon
Authorized by:	Beatriz Revilla-Romero

Code:	D8-PVR-V2
Version:	v2.0
Date:	27/10/2023
Internal code:	GMV 24765/23 V2/23

DOCUMENT STATUS SHEET

Version	Date	Pages	Changes
v1.0	20/09/2023	76	This deliverable D8v2 is an update of D8 delivered in phase 1. Changelog: – validation report has been added and completed for point source emissions for SO_2, CH_3OH, C_2H_2, C_2H_4 – validation report has been added and completed for hotspot source emissions for NO_x – validation report has been completed for regional source emissions CO_2, NO_x and CO (except for China) – validation report has been added and completed for global emissions for CH_4, NH_3, SO_2, NO_x, CO – validation report has been added for point source emissions and regional source emissions for NH_3
v2.0	27/10/2023	76	Comments from ESA implemented: – Updates in Section 3.1 – Updates in Section 3.4 – Updates in Section 4.3.2 – Updates in Section 5.2 From BSC added comparison between HERMESv3 and inverse estimates of anthropogenic CO for the region of Catalonia.

TABLE OF CONTENTS

1. INTRODUCTION 9
1.1. PURPOSE 9
1.2. SCOPE 9
1.3. ACRONYMS 9
2. REFERENCES 12
2.1. APPLICABLE DOCUMENTS 12
2.2. REFERENCE DOCUMENTS 12
3. VALIDATION OF POINT-SOURCE EMISSION INVENTORIES 17
3.1. POINT SOURCE EMISSIONS FROM INVERSION MODELS FOR METHANE (CH4) 17
3.1.1. Computation of the uncertainty intervals of the methane emission flux rates 17
3.1.2. Comparison to Spaceborne measurements 18
3.1.3. Comparison to ground-based measures 20
3.1.4. comparison to spanish e-prtr estimates 20
3.1.5. Summary 21
3.2. POINT SOURCE EMISSIONS FROM INVERSION MODELS FOR CARBON DIOXIDE (CO2) 22
3.2.1. General 22
3.2.2. Summary 24
3.3. POINT SOURCE EMISSIONS FOR NITROGEN OXIDES (NOX) AND SULPHUR DIOXIDE (SO2) 25
3.3.1. NOx point source emissions 25
3.3.1.1. Germany 25
3.3.1.2. USA 26
3.3.1.3. Spain 27
3.3.2. NOx hotspots 28
3.3.2.1. TROPOMI 28
3.3.2.2. EDGAR 28
3.3.2.3. Comparison 28
3.3.2.4. Discussion 29
3.3.3. SO2 point sources 29
3.3.3.1. India 29
3.3.4. Summary 30
3.4. POINT SOURCE EMISSIONS FROM INVERSION MODELS FOR ETHYLENE (C2H4), ACETYLENE (C2H2), AMMONIA (NH3) AND METHANOL (CH3OH) 31
3.4.1. Ethylene (C2H4) point source emissions 32
3.4.1.1. Summary 35
3.4.2. Acetylene (C2H2) point source emissions 35
3.4.2.1. Summary 36
3.4.3. Ammonia (NH_3) point source emissions 37
3.4.3.1. Self-consistency check 37
3.4.3.2. Comparison with the E-PRTR inventory 37
3.4.3.3. Summary 38
3.4.4. Methanol (CH3OH) point source emissions 39
3.4.4.1. Summary 40
4. VALIDATION OF REGIONAL SOURCE INVERSION INVENTORIES 41
4.1. REGIONAL SOURCE INVERSION FOR METHANE (CH4) 41

4.1.1. Comparing total emissions per region to inventories 41
4.1.2. Comparing regional emission factor with country-level emission factors 41
4.1.3. Correlation of retrieved gridded flux rates with bottom-up inventories 42
4.1.4. Summary 44
4.2. REGIONAL SOURCE INVERSION FOR AMMONIA (NH3) 44
4.2.1. Comparison with EDGAR v6.1 44
4.2.2. Summary 45
4.3. REGIONAL SOURCE EMISSIONS FROM INVERSION MODELS FOR CARBON DIOXIDE (CO_2), NITROGEN OXIDES (NO_X), AND CARBON MONOXIDE (CO) 46
4.3.1. Quality control with the internal diagnostics of the inversions....46
4.3.2. Quality control through comparisons to independent inventories 47
4.3.3. Summary 52
5. VALIDATION OF GLOBAL SOURCE INVERSION INVENTORIES....55
5.1. GLOBAL SOURCE INVERSIONS FOR METHANE (CH4) 55
5.1.1. Summary 60
5.2. GLOBAL SOURCE INVERSIONS FOR NITROGEN DIOXIDE (NO2) 60
5.2.1. Comparing total emissions of selected regions to inventories 61
5.2.2. Summary 62
5.3. GLOBAL SOURCE INVERSIONS FOR CARBON MONOXIDE (CO) 63
5.3.1. Summary 66
5.4. GLOBAL SOURCE INVERSIONS FOR SULPHUR DIOXIDE (SO2) 66
5.4.1. Comparing total emissions to inventories 67
5.4.2. Comparing total emissions of seleCted regions to inventories....69
5.4.3. Summary 71
5.5. GLOBAL SOURCE INVERSIONS FOR AMMONIA (NH3) 71
5.5.1. Comparing total emissions to inventories 72
5.5.2. Comparing total emissions of selected regions to inventories 73
5.5.3. Summary 75

LIST OF TABLES AND FIGURES

Table 1-1 Acronyms 9
Table 2-1 Applicable Documents 12
Table 2-2 Reference Documents 12
Table 3-1 Comparison of our flux rates estimates with [RD.10] and [RD.11] in Turkmenistan and Kazakhstan 19
Table 3-2 Inter-comparison assessment table: CH4- point source emissions 21
Table 3-3 Inter-comparison assessment table: CO2- point source emissions 24
Table 3-4 Inter-comparison assessment table: SO_2 - point source emissions 30
Table 3-5 Inter-comparison assessment table: NO_x - point source emissions 31
Table 3-6 Inter-comparison assessment table: NO_x - hotspots 31
Table 3-7 Inter-comparison assessment table: C_2H_4 - point source emissions 35
Table 3-8 Inter-comparison assessment table: C_2H_2 - point source emissions 36
Table 3-9 Inter-comparison assessment table: NH_3 - point source emissions 38
Table 3-10 Inter-comparison assessment table: CH_3OH - point source emissions 40
Table 4-1 Inter-comparison assessment table: CH_4- regional 44
Table 4-2 Inter-comparison assessment table: NH_3 - regional 45
Table 4-3 Total annual CO2 emissions at country level (Cyprus) from national inventory and project estimates 52
Table 4-4 CO2 and NOx emissions by sector (NIR, World Emission) 52
Table 4-5 Inter-comparison assessment table: CO_2- regional 52
Table 4-6 Inter-comparison assessment table: NO_x - regional 53
Table 4-7 Inter-comparison assessment table: CO - regional 54
Table 5-1 Inter-comparison assessment table: CH_4 - global 60
Table 5-2 Inter-comparison assessment table: NO_x - global 62
Table 5-3 Inter-comparison assessment table: CO - global 66
Table 5-4 Inter-comparison assessment table: SO_2 - global 71
Table 5-5 Inter-comparison assessment table: NH_3 - global 75

Figure 3-1 Histogram of the uncertainty interval radius for a set of 200 plumes 18
Figure 3-2 Quantification of emissions detected in Turkmenistan. 19
Figure 3-3 Comparison of TROPOMI-based methane flux rates with ground-based measures 20
Figure 3-4 Representation of the top down (in blue) and E-PRTR (in red) CH_4 point sources detected for Madrid (a) and Murcia (b) (Spain). 21
Figure 3-5 Retrieved emission values for OCO-2 v11 data versus the values inferred from https://globalenergymonitor.org/. The black dots form the bisector. 24
Figure 3-6 Comparison of annual mean NOx emissions from catalog v2 (y-axis) to emissions reported in PRTR, added up within 15 km radius (x-axis), for Germany. Error bars reflect the errors given in the catalogue v2. Correlation coefficients r and the ratio of mean emissions (v2 versus PRTR) are provided in the figure based on all found point source emissions as well as for the subset excluding point source near emissions cities 26

Figure 3-7 Maps of annual mean A* for catalogue rank #71 (51.0125° N, 6.6375° E), corresponding to the lignite power plants Niederaußem and Neurath. Large triangles and circles indicate the location of point source and area source emissions, respectively, based on the classification algorithm described in [RD.26]. Small triangles and circles mark the location of power plants and cities. The dashed circle indicates the integration radius of 15 km. 26

Figure 3-8 Comparison of annual mean NOx emissions from catalogue v2 (y-axis) to emissions reported in eGRID, added up within 15 km radius (x-axis), for the USA. Point source emissions close to cities are skipped, as well as eGRID values below 0.11 kg/s. Error bars reflect the errors given in v2. Correlation coefficients r and the ratio of mean emissions (v2 versus eGRID) are displayed in the figure. 27

Figure 3-9 Maps of annual mean A* for catalogue rank #890 (36.8875° N, 111.4125° W), corresponding to the Navajo coal power plant. The shutdown end of 2019 results in emissions close to zero in 2020 and 2021. 27

Figure 3-10 Comparison of annual mean NOx emissions from catalog v2 (red) to emissions reported in HERMESv3 (blue) added up within 15 km radius, for Spain. Error bars reflect the errors given in the catalogue v2. 28

Figure 3-11 Scatter plot of hotspot emissions estimated from TROPOMI (y-axis) compared to EDGAR (x-axis). Hotspots with deviations by more than a factor of 3 or 1/3 are labelled. 29

Figure 3-12 Comparison of total mean SO_2 emissions from catalog (y-axis) to emissions reported in [RD.42] (x-axis), for India. Error bars reflect the errors given in our catalogue. 30

Figure 3-13 Example of C2H4 flux calculation over Mundo Nuevo, Mexico (adapted from [RD.23])....33

Figure 3-14 Comparison between IASI-derived and EDGAR v4.3.2 emission fluxes of C2H4 (taken from [RD.23]) 34

Figure 3-15 Comparison between IASI-derived and HERMESv3 annual emissions of C2H4 in the point sources of Puertollano and Tarragona (Spain). 34

Figure 3-16 Comparison between IASI-derived and EDGAR v4.3.2 emission fluxes of C_2H_2. 36

Figure 3-17 Comparison between total average flux values, and the average of the yearly flux values for all the reported IASI NH_3 point sources....37

Figure 3-18 Comparison of IASI derived emission fluxes and EPRTR emission fluxes for fertilizer industry in Europe. Pearson's R and regression slope is also reported. 38

Figure 3-19 Comparison between IASI-derived and EDGAR v4.3.2 emission fluxes of CH_3OH. 39

Figure 4-1 Comparison of bottom-up and top-down inventories in the Permian basin 41

Figure 4-2 Comparison of emission factors derived from country-level inventories and basin-level inversions. 42

Figure 4-3 Comparison of our inversion posterior (left) with EDGARv6 oil and gas methane emissions (right) 43

Figure 4-4 Scatter plot comparison of grid cell emission rates for EDGARv6 and our inventory 43

Figure 4-5 Satellite-based emission estimates (in kg/s) for a selection of regions compared with the EDGAR v6.1 emission inventory. The dashed, dash-dotted and dotted black lines represent ratios of EDGAR emission to satellite-based emission of 1:1, 1:10 or 10:1, and 1:100 or 100:1, respectively. The coloured symbols are for selected source areas. Fluxes are calculated assuming a baseline NH3 atmospheric lifetime of 12 h; the error bars correspond to upper- and lower-bound flux estimates based on a lifetime of 1 h and 48 h, respectively. 45

Figure 4-6 Relative change (ratio between the values from the inversion and from the simulations with the Carbon Monitor - CEDS inventory) of the biases between NO_2 monthly mean tropospheric columns from CHIMERE and the TROPOMI observations (aggregated at 0.5° resolution) due to the NO_x emission inversion, in January 2019. All ratios lower than 1, in blue, indicate improvements due to the use of emission estimates from the inversion compared to the use of emission estimates from the Carbon Monitor- CEDS. 47

Figure 4-7 Estimates of the monthly budgets of CO emissions from 2019 to 2022 for the EU27+UK area from the Carbon Monitor - CEDS inventory (in grey), from the regional inversions assimilating

MOPITT CO surface observations (in green) and from the TNO-GHGco-v3 inventory for 2019 (in blue), in ktCO/month. 48

Figure 4-8 Estimates of the monthly budgets of NO_x anthropogenic emissions from 2019 to 2022 for the EU27+UK area from the Carbon Monitor - CEDS inventory (in grey) from the regional inversions assimilating TROPOMI-PAL observations (in green), and from the TNO-GHGco-v3 inventory for 2019(in blue), in $ktNO_2$/month..... 48

Figure 4-9 Estimates of monthly cycles of NO_x anthropogenic emissions for 2020 for EU27+UK and individual countries from the CAMS-REG inventory (in red) and the regional inversions assimilating TROPOMI-PAL observations (in blue). Values represent monthly weight factors (sum up to 12)..... 49

Figure 4-10 Estimates of monthly NOx anthropogenic emissions [t/month] for 2019 for Catalonia (Spain) from the HERMESv3 bottom-up inventory (in red) and the regional inversions assimilating TROPOMI-PAL observations (in blue). 50

Figure 4-11 Total reported a) CO2 (top) and b) NOx (bottom plot) emissions for Cyprus (blue bars) versus estimates from the regional inversions assimilating TROPOMI-PAL observations (orange bars) 51

Figure 5-1 Map of sites from multiple observing platforms and networks used for independent evaluation of global CH4 inversion. For the Total Carbon Column Observing Network (TCCON), only sites with data available in the GGG2014 version of the data retrievals for both 2019 and 2020 are presented. The aircraft CH4 vertical profiles are compiled from data products from NOAA's GGGRN, the In-service Aircraft for a Global Observing System and Japan Meteorological Agency and mapped on the model grids of the global inversion system (1.9°x3.75°), coloured by the number of CH4 vertical profiles. The AirCore samplings are obtained from NOAA AirCore campaigns, which are available at Boulder, US and Traînou, France in 2019 and are only available at Boulder, US in 2020. 55

Figure 5-2 The change in XCH4 between 2019 and 2020 for January–March (JFM), April–June (AMJ), July–September (JAS), and October–December (OND) at TCCON sites. Black dots are observations, Blue dots prior and red dots are posterior data. Note that values at sites between 30°N–40°N and 40°N–50°N are averaged (denoted as "LAT30" and "LAT40" respectively) for better visualization. The GGG2014 version of the TCCON retrievals is used for evaluation (site abbreviations: BREM–Bremen; BURG–Burgos; DARW–Darwin; EAST–East Trout Lake; EURE–Eureka; IZAN–Izana; LAUD–Lauder; NYAL–Ny-Alesund; REUN–Réunion Island; SODA–Sodankyla; WOLL–Wollongong; also see Figure 5-1 for site locations). 56

Figure 5-3 The latitudinal gradients of simulated versus observed vertical CH4 differences between 1–2 km and 4–5 km altitude bins for January–March (JFM), April–June (AMJ), July–September (JAS), and October–December (OND) during 2019–2020. The CH4 vertical profiles were obtained from various aircraft sampling networks and campaigns (see Fig 4.1 for locations of sampling sites). For each panel, the simulated or observed vertical CH4 differences across sampling sites were averaged by latitude bands of 10°. Error bars denote one standard deviation of the estimates across sites within a latitude band..... 57

Figure 5-4 Comparison of vertical CH4 profiles in the troposphere and lower stratosphere between in-situ Aircore sampling (black points) and the simulations of the LMDZ INCA model 58

Figure 5-5 Comparison between modeled a priori (blue) and posterior optimized after GOSAT assimilation (red) concentrations against independent Aircore measurements at different altitude bins collected by Aircore data in Boulder Colorado. The grey area is the period of analysis of the WOREM project..... 59

Figure 5-6 Left column: Daily time-series (10-day running mean) total constrained NOx (orange and green solid line for 2019 and 2020) over selected regions using TROPOMI observations and mass-balance method, and CEDS bottom-up inventories (blue solid line) for 2019. Right column: Daily time-series of difference between estimated fluxes for 2020 and 2019 from mass-balance method..... 61

Figure 5-7 Annual mean NOx fluxes for CEDS, CAMS, TROPOMI and OMI calculated over US, Europe, China, India and Middle East for (a) 2019 and (b) 2020 (unit: Tg-N/yr). 62

Figure 5-8 Spatial distribution of the independent measurements. The TCCON stations are shown with rectangles, the surface stations are shown in green circles, the MOZAIC quasi-profile overages are shown at the model grid in orange, the HIPPO profile coverage is shown at the model resolution in blue..... 63

Figure 5-9 Model-data biases along the latitudes. (a) and (b) present model biases to MOPITT Xco using INCA-OH and TransCom-OH, respectively. Dashed and solid lines represent forward and posterior model results, respectively, while color codes correspond to model versions shown in the legend. (c) and (d) present model biases to TCCON Xco measurements using INCA-OH and TransCom-OH respectively. (e) and (f) show model biases compared to ground measurements from surface network using INCA-OH and TransCom-OH respectively. Note the ordinates are different for the three observation types. 64

Figure 5-10 Zonal averages of the model bias in the vertical CO profiles. The left column shows results against MOZAIC measurements, and the right column shows results against HIPPO measurements. The error bars indicate the standard variation of the measurements. Results associated with INCA-OH are presented....65

Figure 5-11: Comparison of the daily variation of the estimated anthropogenic SO2 emissions over selected regions (sub-sampled on the common grids) using TROPOMI and OMI observations for 2019, 2020, and 2021. 67

Figure 5-12: Comparison of the monthly global estimated anthropogenic SO2 emissions over the land using TROPOMI ((a) and (b)) and OMI ((c) and (d)) observations with the emissions from CEDS and CAMS bottom-up inventories sub-sampled on the common grids for 2020 and 2021. 68

Figure 5-13: Spatial distribution of the seasonal anthropogenic SO2 emissions over the land estimated using the TROPOMI observations (left), and the corresponding sub-sampled emissions on the common grids from the CEDS (middle) and CAMS (right) bottom-up inventories for 2020. 68

Figure 5-14: Comparison of the monthly regional estimated anthropogenic SO2 emissions over the land using TROPOMI observations with the emissions from CEDS and CAMS bottom-up inventories sub-sampled on the common grids for 2020....69

Figure 5-15: Comparison of the annual regional anthropogenic SO2 emissions estimated using TROPOMI ((a) and (b)) and OMI ((c) and (d)) observations with corresponding sub-sampled emissions on the common grids from the CEDS and CAMS bottom-up inventories for, 2019, 2020 and 2021. ...70

Figure 5-16: A comparison of TROPOMI and OMI constrained SO2 emissions with the co-located point source emissions from a catalogue reported in [RD.42]. 70

Figure 5-17 Daily variation of the IASI constrained NH3 emissions over the selected regions for 2019, 2020, and 2021....72

Figure 5-18: Comparison of the monthly global estimated anthropogenic NH3 emissions over the land using IASI observations with the emissions from CEDS and CAMS bottom-up inventories sub-sampled on the common grids for 2019, 2020, and 2021. 72

Figure 5-19: Spatial distribution of the seasonal global anthropogenic NH3 emissions over the land estimated using the IASI observations (left), and the corresponding sub-sampled emissions on the common grids from the CEDS (middle) and CAMS (right) bottom-up inventories for 2020. 73

Figure 5-20: Comparison of the monthly regional estimated anthropogenic NH3 emissions over the land using IASI observations with the emissions from CEDS and CAMS bottom-up inventories sub-sampled on the common grids for 2020....74

Figure 5-21: Comparison of the annual regional anthropogenic NH3 emissions estimated using IASI observations with corresponding sub-sampled emissions on the common grids from the CEDS and CAMS bottom-up inventories for 2020 and 2021....74

1. INTRODUCTION

1.1. PURPOSE

The present document corresponds to version 2 of the deliverable D8 - Product Validation Report (PVR) of the World Emission project as part of the Work Package 500 "Full service implementation & final product validation". This task defines the processes undertaken to ensure the validation of the various emission inventories. This encompasses a validation of their technical consistency, of the consistency of their assumptions and auxiliary data, and the technical level consistency. The Product Validation Report (PVR-V2) is the update of the PVR delivered in February 2023 and details hereafter the validation processes as defined in the Product Validation Plan (PVP, document D4, [RD.4]). A brief summary of each one of the validation process outputs can also be found in the D4 document. The present document contains complete validation reports for all gases and scopes (point sources, regional sources and global emissions), except for point source and regional source emissions of NH_3 (ammonia).

1.2. SCOPE

This document is structured according to the following sections:

- Section 3, provides validation processes for point-source emission inventories.
- Section 4, provides validation processes for regional inversion inventories.
- Section 5, provides validation processes for global inversion inventories.

1.3. ACRONYMS

Acronyms used in this document and needing a definition are included in the following table:

Table 1-1 Acronyms

Acronym	Definition
AMJ	April May June
ATBD	Algorithm Theoretical Basis Document
BAMS	Bulletin of the American Meteorological Society
BREM	Bremen
BURG	Burgos
CHIMERE	CHIMERE chemistry-transport model
CIF	Community Inversion Framework
CMAS	Copernicus Atmosphere Monitoring Service
COBRA	Covariance-Based Retrieval Algorithm
DARW	Darwin
EAST	East Trout Lake
ECMWF	European Centre for Medium-Range Weather Forecasts
EPA	United States Environmental Protection Agency
EPRTR	European Pollutant Release and Transfer Register
ESA	European Space Agency
ESSD	Earth System Science Data Journal
EURE	Eureka
EXPRO+	Statement of Work ESA Express Procurement Plus
GDAS	Global Data Assimilation System
GFED	Global Fire Emissions Database
GFEI	Global Fuel Exploitation Inventory
GFS	NCEP's Global Forecast System

Acronym	Definition
GGGRN	NOAA's Global Greenhouse Gas Reference Network
GHG	Green House Gases
GMES	Global Monitoring for Environment and Security
GOSAT	Greenhouse gases Observing SATellite
HCHO	Formaldehyde
HERMES	High-Elective Resolution Modelling Emission System
HIPPO	HIAPER Pole-to-Pole Observations
HYSPLIT	HYbrid Single-Particle Lagrangian Integrated Trajectory
IAGOS	In-service Aircraft for a Global Observing System
IASI	Infrared Atmospheric Sounding Interferometer
IEA	International Energy Agency
IIR	Informative Inventory Report
INCA	INteraction with Chemistry and Aerosols
IZAN	Izana
JAS	July August September
JFM	January February March
JJA	June July August
LAUD	Lauder
LMDZ	Atmospheric Global Circulation Model of the Laboratoire de Météorologie Dynamique with a zoom capability
LPS	Large point source
MAM	March April May
MEGAN	Model of Emissions of Gases and Aerosols from Nature
MITERD	Ministerio para la Transición Ecológica y el Reto Demográfico (Spanish Ministry of Environment)
MODIS	Moderate Resolution Imaging Spectroradiometer
MOPITT	Measurement of Pollution in the Troposphere
NIR	Near-infrared
NMVOC	Non-Methane Volatile Organic Compound
NOAA	National Oceanic and Atmospheric Administration
NYAL	Ny-Alesund
OCO	Orbiting Carbon Observatory
OMI	Ozone Monitoring Instrument
OND	October November December
PAL	Products Algorithm Laboratory
PVP	Product Validation Plan
PVR	Product Validation Report
PYVAR	A regional atmospheric inversion system developed at LSCE
REG	Regional
REUN	Réunion Island
SKW	Stickstoffwerke Piesteritz
SODA	Sodankyla
SOW	Statement of Work
TCCON	Total Carbon Column Observing Network
TNO	Netherlands Organisation for Applied Scientific Research
VCD	Vertical Column Density
WDCC	World Data Center for Climate

Acronym	Definition
WOLL	Wollongong

2. REFERENCES

2.1. APPLICABLE DOCUMENTS

The following documents, of the exact issue shown, form part of this document to the extent specified herein. Applicable documents are those referenced in the Contract or approved by the Approval Authority. They are referenced in this document in the form [AD.x]:

Table 2-1 Applicable Documents

Ref.	Title	Code	Version	Date
[AD.1]	Statement of Work. ESA Express Procurement Plus - [EXPRO+] World Emission	EOP-SD-SOW-2019-0101 Tender Reference ESA AO/1-10482/21/I-EF	1	15/04/2021
[AD.2]	World Emission Proposal	GMV 12175/21	2	7/12/2021
[AD.3]	ESA Contract No. 4000137291/22/I-EF	4000137291/22/I-EF	1	15/02/2022

2.2. REFERENCE DOCUMENTS

The following documents, although not part of this document, amplify or clarify its contents. Reference documents are those not applicable and referenced within this document. They are referenced in this document in the form [RD.x]:

Table 2-2 Reference Documents

Ref.	Title	Code	Version	Date
[RD.1]	D1 - User Requirements Document	GMV 22331/22 V2/22	2	01/09/2022
[RD.2]	D2 - Technical Specification Document	GMV 22695/22 V2/22	2	01/09/2022
[RD.3]	D3 - Algorithm Theorical Basis Document v3	GMV 24675/23 V2/23	2	27/10/2023
[RD.4]	D4 – Product Validation Plan	GMV 23837/22 V2/22	2	27/09/2022
[RD.5]	D5- System Specifications Document v2	GMV 24765/23 V1/23	1	20/09/2023
[RD.6]	D6 – System Verification Report v2	GMV 24765/23 V1/23	1	20/09/2023
[RD.7]	Lauvaux, T., Giron, C., Mazzolini, M., D'Aspremont, A., Duren, R., Cusworth, D., Shindell, D. &, Ciais, P. (2022). Global assessment of oil and gas methane ultra-emitters, Science, 10.1126/science.abj4351	-	-	2022
[RD.8]	Stein, A.F., Draxler, R.R, Rolph, G.D., Stunder, B.J.B., Cohen, M.D., and Ngan, F., (2015). NOAA's HYSPLIT atmospheric transport and dispersion modelling system, Bull. Amer. Meteor. Soc., 96, 2059-2077, http://dx.doi.org/10.1175/BAMS-D-14-00110.1	-	-	2015
[RD.9]	Pandey, S., Ritesh Gautam, Sander Houweling, Hugo Denier van der Gon, Pankaj Sadavarte, Tobias Borsdorff, Otto Hasekamp, Jochen Landgraf, Paul Tol, Tim van Kempen, Ruud Hoogeveen, Richard van Hees, Steven P. Hamburg, Joannes D. Maasakkers, Ilse Aben: Satellite observations reveal extreme methane leakage from a natural gas well blowout, Proceedings of the National Academy of Sciences Dec 2019, 116 (52) 26376-26381; DOI:10.1073/pnas.1908712116.	-	-	2019

Ref.	Title	Code	Version	Date
[RD.10]	Varon, D. J., Jacob, D. J., McKeever, J., Jervis, D., Durak, B. O. A., Xia, Y., & Huang, Y. (2018). Quantifying methane point sources from fine-scale satellite observations of atmospheric methane plumes. Atmospheric Measurement Techniques, 11, 5673–5686. https://doi.org/10.5194/amt-11-5673-2018	-	-	2018
[RD.11]	Ehret, T., et al. (2021). Global Tracking and Quantification of Oil and Gas Methane Emissions from Recurrent Sentinel-2 Imagery, https://doi.org/10.48550/arXiv.2110.11832	-	-	2021
[RD.12]	Varon, D. J., McKeever, J., Jervis, D., Maasakkers, J. D., Pandey, S., Houweling, S., et al. (2019). Satellite discovery of anomalously large methane point sources from oil/gas production. Geophysical Research Letters, 46, 13507– 13516. https://doi.org/10.1029/2019GL083798	-		2019
[RD.13]	Chevallier, F., B. Zheng, et al. (2020), Local anomalies in the column-averaged dry air mole fractions of carbon dioxide across the globe during the first months of the coronavirus recession, Geophys. Res. Lett, doi:10.1029/2020GL090244	-	-	2020
[RD.14]	Zheng, B., Chevallier, F., Ciais, P., Broquet, G., Wang, Y., Lian, J., and Zhao, Y.: Observing carbon dioxide emissions over China's cities and industrial areas with the Orbiting Carbon Observatory-2, Atmos. Chem. Phys., 20, 8501–8510, doi:10.5194/acp-20-8501-2020, 2020	-	-	2020
[RD.15]	Rey-Pommier, A., Chevallier, F., Ciais, P., Broquet, G., Christoudias, T., Kushta, J., Hauglustaine, D., and Sciare, J.: Quantifying NOx emissions in Egypt using TROPOMI observations, Atmos. Chem. Phys. Discuss. [preprint], https://doi.org/10.5194/acp-2021-1051, in review, 2022.	-	-	2022
[RD.16]	Van Damme, M., Clarisse, L., Whitburn, S., Hadji-Lazaro, J., Hurtmans, D., Clerbaux, C., Coheur, P.-F. Industrial and agricultural ammonia point sources exposed. Nature 564, 99-103, doi: 10.1038/s41586-018-0747-1, 2018	-	-	2018
[RD.17]	Chevallier, F., Broquet, G., Zheng, B., Ciais, P., & Eldering, A. (2022). Large CO2 emitters as seen from satellite: Comparison to a gridded global emission inventory. Geophysical Research Letters, 49, e2021GL097540. https://doi.org/10.1029/2021GL097540	-	-	2022
[RD.18]	Berchet, A., Sollum, E., Thompson, R. L., Pison, I., Thanwerdas, J., Broquet, G., Chevallier, F., Aalto, T., Berchet, A., Bergamaschi, P., Brunner, D., Engelen, R., Fortems-Cheiney, A., Gerbig, C., Groot Zwaaftink, C. D., Haussaire, J.-M., Henne, S., Houweling, S., Karstens, U., Kutsch, W. L., Luijkx, I. T., Monteil, G., Palmer, P. I., van Peet, J. C. A., Peters, W., Peylin, P., Potier, E., Rödenbeck, C., Saunois, M., Scholze, M., Tsuruta, A., and Zhao, Y.: The Community Inversion Framework v1.0: a unified system for atmospheric inversion studies, Geosci. Model Dev., 14, 5331–5354, https://doi.org/10.5194/gmd-14-5331-2021, 2021.	-	-	2021
[RD.19]	Deeter, M. N., Edwards, D. P., Francis, G. L., Gille, J. C., Mao, D., Martínez-Alonso, S., Worden, H. M., Ziskin, D., and Andreae, M. O.: Radiance-based retrieval bias mitigation for the MOPITT instrument: the version 8 product, Atmos. Meas. Tech., 12, 4561–4580, https://doi.org/10.5194/amt-12-4561-2019, 2019.	-	-	2019

Ref.	Title	Code	Version	Date
[RD.20]	Fortems-Cheiney, A., Pison, I., Broquet, G., Dufour, G., Berchet, A., Potier, E., Coman, A., Siour, G., and Costantino, L.: Variational regional inverse modeling of reactive species emissions with PYVAR-CHIMERE-v2019, Geosci. Model Dev., 14, 2939–2957, https://doi.org/10.5194/gmd-14-2939-2021, 2021.	-	-	2021
[RD.21]	Levelt, P. F., Joiner, J., Tamminen, J., Veefkind, J. P., Bhartia, P. K., Stein Zweers, D. C., Duncan, B. N., Streets, D. G., Eskes, H., van der A, R., McLinden, C., Fioletov, V., Carn, S., de Laat, J., DeLand, M., Marchenko, S., McPeters, R., Ziemke, J., Fu, D., Liu, X., Pickering, K., Apituley, A., González Abad, G., Arola, A., Boersma, F., Chan Miller, C., Chance, K., de Graaf, M., Hakkarainen, J., Hassinen, S., Ialongo, I., Kleipool, Q., Krotkov, N., Li, C., Lamsal, L., Newman, P., Nowlan, C., Suleiman, R., Tilstra, L. G., Torres, O., Wang, H., and Wargan, K.: The Ozone Monitoring Instrument: overview of 14 years in space, Atmos. Chem. Phys., 18, 5699–5745, https://doi.org/10.5194/acp-18-5699-2018, 2018.	-	-	2018
[RD.22]	Menut, L., Bessagnet, B., Khvorostyanov, D., Beekmann, M., Blond, N., Colette, A., Coll, I., Curci, G., Foret, G., Hodzic, A., Mailler, S., Meleux, F., Monge, J.-L., Pison, I., Siour, G., Turquety, S., Valari, M., Vautard, R., and Vivanco, M. G.: CHIMERE 2013: a model for regional atmospheric composition modelling, Geosci. Model Dev., 6, 981–1028, https://doi.org/10.5194/gmd-6-981-2013, 2013.	-	-	2013
[RD.23]	Franco, B., Clarisse, L., Van Damme, M., Hadji-Lazaro, J., Clerbaux, C., and Coheur, P.: Ethylene industrial emitters seen from space, Nat. Comm., 13, 6452, https://doi.org/10.1038/s41467-022-34098-8, 2022.	-		2022
[RD.24]	Huang, G., Brook, R., Crippa, M., Janssens-Maenhout, G., Schieberle, C., Dore, C., Guizzardi, D., Muntean, M., Schaaf, E., and Friedrich, R.: Speciation of anthropogenic emissions of non-methane volatile organic compounds: a global gridded data set for 1970–2012, Atmos. Chem. Phys., 17, 7683–7701, https://doi.org/10.5194/acp-17-7683-2017, 2017.	-		2017
[RD.25]	Beirle, S., Borger, C., Jost, A., and Wagner, T.: Catalog of NOx point source emissions (version 2), World Data Center for Climate (WDCC) at DKRZ, https://doi.org/10.26050/WDCC/No_xPointEmissionsV2, 2023.	-		2023
[RD.26]	Beirle, S., Borger, C., Jost, A., Wagner, T.: Improved catalog of NOx point source emissions (version 2), submitted to ESSD.	-		2023
[RD.27]	PRTR Germany: Pollutant Release and Transfer Register for Germany, Umweltbundesamt, https://thru.de/fileadmin/SITE_MASTER/content/Dokumente/Downloads/01_Topthemen/PRTR-Daten_2020/XLSX_PRTR-Export_GERMANY_2022-04-29.zip, 2022.	-		2022
[RD.28]	eGRID: Emissions & Generation Resource Integrated Database, United States Environmental Protection Agency (EPA), Washington, DC: Office of Atmospheric Programs, Clean Air Markets Division. Available from EPA's eGRID web site: https://www.epa.gov/egrid. 2022.	-		2022
[RD.29]	Zheng, B., Geng, G., Ciais, P., Davis, S.J., Martin, R.V., Meng, J., Wu, N., Chevallier, F., Broquet, G., Boersma, F. and van der A, R., 2020. Satellite-based estimates of decline and rebound in China's CO2 emissions during COVID-19 pandemic. Science Advances, 6(49), p.eabd4998.	-		2020

Ref.	Title	Code	Version	Date
[RD.30]	Zhang, Y. et al. Quantifying methane emissions from the largest oil-producing basin in the United States from space. Sci. Adv. 6, eaaz5120 (2020)	-		2020
[RD.31]	EPA. Inventory of U.S. Greenhouse Gas Emissions and Sinks: 1990-2019. United States Environmental Protection Agency (2021).	-		2021
[RD.32]	Scarpelli, Tia R.; Jacob, Daniel J., 2019, "Global Fuel Exploitation Inventory (GFEI)", https://doi.org/10.7910/DVN/HH4EUM, Harvard Dataverse, V2	-		2019
[RD.33]	EDGARv6, Joint Research Center (2019), https://edgar.jrc.ec.europa.eu/	-		2019
[RD.34]	Fortems-Cheiney, A., and Broquet, G. (2022): Final re-analysis of the national scale CO2 anthropogenic emissions over 2055-2015, VERIFY public deliverable D2.12, https://verify.lsce.ipsl.fr/index.php/repository/public-deliverables/wp2-verification-methods-for-fossil-co2-emissions/d2-12-final-re-analysis-of-the-national-scale-co2-anthropogenic-emissions-over-2005-2015	-		2022
[RD.35]	Veefkind, J., et al. (2012) TROPOMI on the ESA Sentinel-5 Precursor: A GMES Mission for Global Observations of the Atmospheric Composition for Climate, Air Quality and Ozone Layer Applications. Remote Sensing of Environment, 120, 70-83. https://doi.org/10.1016/j.rse.2011.09.027	-		2012
[RD.36]	Guenther, A., Karl, T., Harley, P., Wiedinmyer, C., Palmer, P. I., and Geron, C.: Estimates of global terrestrial isoprene emissions using MEGAN (Model of Emissions of Gases and Aerosols from Nature), Atmos. Chem. Phys., 6, 3181–3210, https://doi.org/10.5194/acp-6-3181-2006, 2006.	-		2006
[RD.37]	Gilbert, J. C., and C. Lemaréchal: Some numerical experiments with variable-storage quasi-Newton algorithms, Math. Program., 45, 407–435, 1989. https://link.springer.com/article/10.1007/BF01589113	-		1989
[RD.38]	D8 - Product Validation Report (PVR)	GMV 24765/23 V1/23	V1.2	12/04/2023
[RD.39]	Lamsal, L. N., Martin, R. V., Padmanabhan, A., Van Donkelaar, A., Zhang, Q., Sioris, C. E., Chance, K., Kurosu, T. P., & Newchurch, M. J. (2011). Application of satellite observations for timely updates to global anthropogenic NOx emission inventories. Geophysical Research Letters, 38(5). https://doi.org/10.1029/2010GL046476			2011
[RD.40]	Cooper, M., Martin, R. V., Padmanabhan, A., & Henze, D. K. (2017). Comparing mass balance and adjoint methods for inverse modeling of nitrogen dioxide columns for global nitrogen oxide emissions. Journal of Geophysical Research: Atmospheres, 122(8), 4718–4734. https://doi.org/10.1002/2016JD025985			2017
[RD.41]	Hoesly, R., O'Rourke, P., Braun, C., Feng, L., Smith, S. J., Pitkanen, T., Seibert, J. J., Vu, L., Presley, M., Bolt, R., Goldstein, B., & Kholod, N. (2019). Community Emissions Data System. https://doi.org/10.5281/ZENODO.3592073			2019

Ref.	Title	Code	Version	Date
[RD.42]	Fioletov, V.E., McLinden, C.A., Griffin, D., Abboud, I., Krotkov, N., Leonard, P.J., Li, C., Joiner, J., Theys, N. and Carn, S., 2023. Version 2 of the global catalogue of large anthropogenic and volcanic SO2 sources and emissions derived from satellite measurements. Earth System Science Data, 15(1), pp.75-93.			2023
[RD.43]	Guevara, M., Tena, C., Porquet, M., Jorba, O., and Pérez García-Pando, C.: HERMESv3, a stand-alone multi-scale atmospheric emission modelling framework – Part 2: The bottom–up module, Geosci. Model Dev., 13, 873–903, https://doi.org/10.5194/gmd-13-873-2020, 2020.			2020
[RD.44]	Oliveira, K., M. Guevara, O. Jorba, X. Querol and C. Pérez García-Pando: A new NMVOC speciated inventory for a reactivity-based approach to support ozone control strategies in Spain. Science of the Total Environment, 161449, doi:10.1016/j.scitotenv.2023.161449, 2023.			2023
[RD.45]	Guevara, M., Petetin, H., Jorba, O., Denier van der Gon, H., Kuenen, J., Super, I., Jalkanen, J.-P., Majamäki, E., Johansson, L., Peuch, V.-H., and Pérez García-Pando, C.: European primary emissions of criteria pollutants and greenhouse gases in 2020 modulated by the COVID-19 pandemic disruptions, Earth Syst. Sci. Data, 14, 2521–2552, https://doi.org/10.5194/essd-14-2521-2022, 2022.			2022
[RD.46]	Dammers, E., McLinden, C. A., Griffin, D., Shephard, M. W., Van Der Graaf, S., Lutsch, E., ... & Erisman, J. W.: NH3 emissions from large point sources derived from CrIS and IASI satellite observations. Atmospheric chemistry and physics, 19(19), 12261-12293, 2019.			2019
[RD.47]	Noppen, L., Clarisse, L., Tack, F., Ruhtz, T., Merlaud, A., Van Damme, M., ... & Coheur, P.: Constraining industrial ammonia emissions using hyperspectral infrared imaging. Remote Sensing of Environment, 291, 113559, 2023.			2023
[RD.48]	Giglio, L., Schroeder, W. & Justice, C. O. The collection 6 MODIS active fire detection algorithm and fire products. Remote Sens. Environ. 178, 31–41, 2016.			2016
[RD.49]	Clarisse, L., Van Damme, M., Clerbaux, C., and Coheur, P.-F.: Tracking down global NH3 point sources with wind-adjusted superresolution, Atmos. Meas. Tech., 12, 5457–5473, https://doi.org/10.5194/amt-12-5457-2019, 2019.			2019
[RD.50]	Watine-Guiu, M., Varon, D. J., Irakulis-Loitxate, I., Balasus, N., and Jacob, D. J.: Geostationary satellite observations of extreme methane emissions from a natural gas pipeline, [preprint] https://doi.org/10.31223/X5K661, 2023.			2023

3. VALIDATION OF POINT-SOURCE EMISSION INVENTORIES

3.1. POINT SOURCE EMISSIONS FROM INVERSION MODELS FOR METHANE (CH4)

Section 3.1.1 details how uncertainty measures are computed for flux rate estimates; sections 3.1.2 and 3.1.3 detail how the flux rate quantifications have been compared and validated against third-party spaceborne and ground-based measures. Additional technical details for both sections are also available in [RD.7].

3.1.1. COMPUTATION OF THE UNCERTAINTY INTERVALS OF THE METHANE EMISSION FLUX RATES

Uncertainty in flux rate estimates mainly stems from sensitivity in the flux rate quantification model input parameters. We adapt the ensemble approach of research papers [RD.9], [RD.10] to estimate the sensitivity of the flow rate estimates. The sources of uncertainty in our flux rate estimates are:

- uncertainty on the Sentinel-5 Precursor measurements,
- errors in meteorological data driving our HYSPLIT simulations,
- sensitivity of the background quantification method,
- sensitivity of the longitude and latitude of the source location estimation,
- sensitivity of the quantification method itself (mass balance)

Our sensitivity analysis is applied on a set of 200 plumes randomly selected among the methane plumes assigned to oil and gas activities and detected in 2019-2020. We build an ensemble of simulations and flux rate quantifications. The sensitivity associated with each parameter is taken as the standard deviation of the ensemble and is further summed in quadrature with 1-sigma uncertainty on the data (meteorological and gas concentration data). For each methane plume detected, the ensemble of flux rates estimates is built on the following ensemble of parameters:

- latitude and longitude vary from one reprojected Sentinel-5 Precursor pixel variation around the estimated source, to evaluate sensitivity from source location. This leads to a set of 9 flow rate estimates for each plume;
- Two meteorological driver data sources are used to estimate the 1-sigma error associated with meteorological data: GFS 0.25 degree, GDAS 1 degree;
- Simulation start times are offset by ± 2 hours - with an hourly sampling - around the estimated optimal start time (determined by the human labeller);
- Methane enhancements are computed using 4 different background value estimates (means and medians, with and without exclusion window).
- The TROPOMI uncertainty on the methane concentration measure is propagated through the whole flux rate quantification process.

Assuming these parameters contribute independently to the overall uncertainty, individual parameters contributions are summed in quadrature to obtain the overall uncertainty:

$$\sigma_{total} = \sqrt{\sigma^2_{location} + \sigma^2_{measure} + \sigma^2_{weather} + \sigma^2_{offset\,hour} + \sigma^2_{background}}$$

The results of this study on a set of 200 plumes are shown on Figure 3-1. The average relative uncertainty interval radius is 45%.

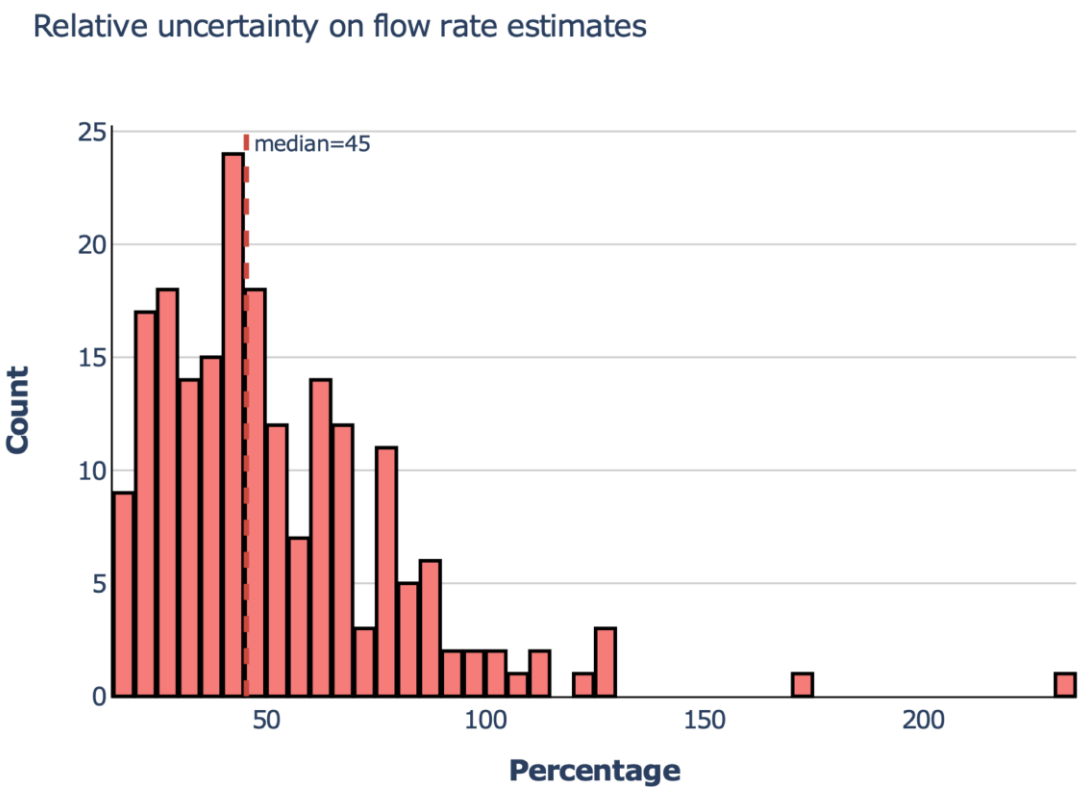

Figure 3-1 Histogram of the uncertainty interval radius for a set of 200 plumes

3.1.2. COMPARISON TO SPACEBORNE MEASUREMENTS

To validate our flow rate quantification process, we compared our estimated flux rate with those published in research papers ([RD.10],[RD.11], [RD.50]). Using images from both GHGSat and TROPOMI, [RD.10] detected and quantified methane emissions from a compressor station of the Korpezhe pipeline in Turkmenistan. This study sheds light on recurring massive methane emissions throughout the year 2018 and in January 2019. We compared our detections and quantifications with theirs when both studies overlap (i.e., January 2019). Outputs of this comparison are shown on [Figure 3-2] below. During the month of January 2019, the average of our measures is 83t/h (± 27t/h), whereas the average of the flow rates measured by [RD.10] is around 77t/h (± 35t/h) using TROPOMI and 47t/h (± 29t/h) using GHGSat (on different periods). It should be noted that our TROPOMI measurements days do not match exactly all measurements from [RD.10] for various reasons detailed hereafter. While [RD.10] quantified emissions from TROPOMI images selected by hand, our approach consists in detecting automatically plumes. Hence, on January 13th, the methane enhancement in the vicinity of the compressor station has not been detected by our plume detection algorithm. This is due to a second large methane anomaly in the area. This second, larger plume in the vicinity contribute to a large local standard deviation which prevents the detection of this smaller plume by our detection algorithm. On January 24h, our algorithm detected the methane plumes quantified by [RD.10] but the HYSPLIT [RD.8] simulation does not match the observed plume; the quantification has therefore not been accepted by the human labelling process. On January 27th, the detection is filtered out because of the strong discrepancy between the main direction of the observed plume and the ECMWF ERA-5 wind direction data. On a monthly-aggregated basis, our estimates and the estimates from [RD.10] have a relative difference of 7%.

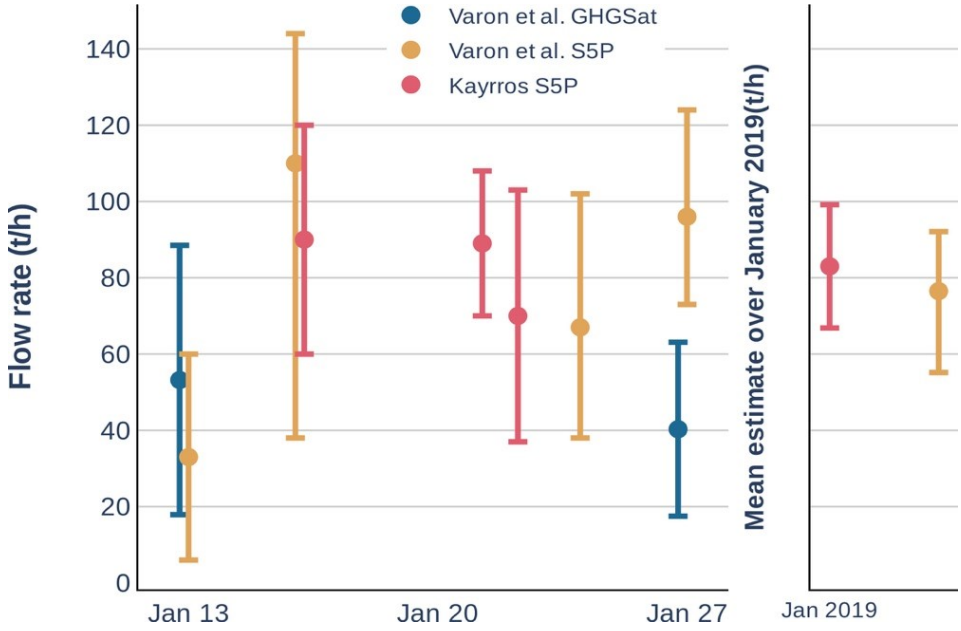

Figure 3-2 Quantification of emissions detected in Turkmenistan.

[RD.11] provides methane plume flux rate estimates based on Sentinel-2 images which can also be used to compare with our TROPOMI-based estimates. A plume detected by [RD.11] in Kazakhstan on September 21st. 2020 provides an ideal comparison point as the same point has been overpassed by both Sentinel-2 and Sentinel-5P on the same day (with about 3 hours delay between both) and the point source emission area (a pipeline compressor station) is far from oil and gas production facilities, coal mines, cities or natural methane sources (e.g., wetlands) which could have contaminated the Sentinel-5P flux rate quantification. The Sentinel-2 flux rate estimate for this plume is 63 t/h whereas the TROPOMI-based estimate it 112 t/h. The relative difference between both estimate is 43%, which is significant although not unusual for a gas emission flux rate estimated from satellite data. The difference might also stem from the difference in overpass time between both satellites (about 3 hours). Also, the main assumption in both quantification method is the fact that the flux rate is constant, which is obviously false in this case of pipeline blowdown and might disrupt the flux rate quantification.

The comparison of the quantified plumes in [RD.10] and [RD.11] in Turkmenistan and Kazakhstan is summarized in the following table:

Table 3-1 Comparison of our flux rates estimates with [RD.10] and [RD.11] in Turkmenistan and Kazakhstan

Metric	Value
Mean of absolute differences	19.0 metric tons per hour
Mean of relative differences	19.0%
Standard deviation of absolute differences	18.8 metric tons per hour
Standard deviation of relative differences	16.3%
Absolute bias	8.5 metric tons per hour
Relative bias	7.2%
Mean uncertainty radius*	27.3 metric tons per hour
Mean relative uncertainty	+/-45% [RD.7]

*The radius is the half of the amplitude of the confidence interval.

Relative difference between third-part research papers and our results is below 20%. This is significantly below the mean relative uncertainty on the flux rate estimates (45% [RD.7]). Likewise, the bias between our estimates and third-party estimates can be considered as non-significant as it is significantly lower than the mean relative uncertainty (7.2%). These figures, which are consistent with

what can be found in third-party research papers, overall emphasize that the estimates are to be considered as orders of magnitude of the flux rates rather than as exact quantifications.

In [RD.50], Watine et al. detect and quantify an extremely large methane plume on May 12th, 2019 in Durango, Mexico using geostationary satellite data from the Geostationary Operational Environmental Satellite (GOES-R). Although GOES-R has a poor sensitivity to methane, it is able to produce measures with a 5 minutes revisit, hence providing very complementary data to the aforementioned satellites (Sentinel-5P, Sentinel-2 and GHGSat). [RD.50] provides a series of measures based on GOES-R data, in the range of [260-550] metrics tons per hour over three hours, in line with our estimated 372 metric tons per hour [201-543 t/h]. In addition, [RD.50] provide an estimate of the flux rate based on TROPOMI data and the IME method. The resulting flux rate is 460 metric tons per hour (+/- 90t/h), still in line with our TROPOMI estimate.

3.1.3. COMPARISON TO GROUND-BASED MEASURES

On images sensed on May 24th, 2021, and June 4th, 2021, we detected large methane plumes located in the vicinity of Russian pipelines, respectively in the Republic of Bashkortostan and in Tatarstan. Their flow rates have been quantified at respectively 214 t/h (± 186t/h) and 395 t/h (± 97t/h). The emission detection on May 24th coincide with maintenance operations on the Urengoy-Petrovsk pipeline during which 900,000 cubic meters (610 tons) of methane have been released, whereas the detection on June 4th, 2021 coincides with a release of 2.7 million cubic meters of methane (1830 tons) which occurred during an emergency repair at the Urengoy-Center 1 pipeline (see Bloomberg article). The release durations used in the HYSPLIT model for estimating the flux rate and that best fit both observed plumes are respectively 4 and 3 hours. To compare our estimated flux rates with emissions communicated by the pipeline operator, we derive total emissions values by multiplying the estimated flux rate by these estimated emission durations. Total methane emission estimates are 846 tons ± 743 tons (resp.1796 tons ± 1560 tons) for the May 24th detection and 1185 tons ± 292 tons (resp. 2488 tons ± 612 tons). These results are in line with the amounts reported by the pipeline operator, as can be visualized on Figure 3-3. The unusually high relative uncertainty on the flow rate on May 24th (relative uncertainty of 87%) is due to a very high uncertainty on the methane concentration measured by the sensor, which is propagated through our quantification process.

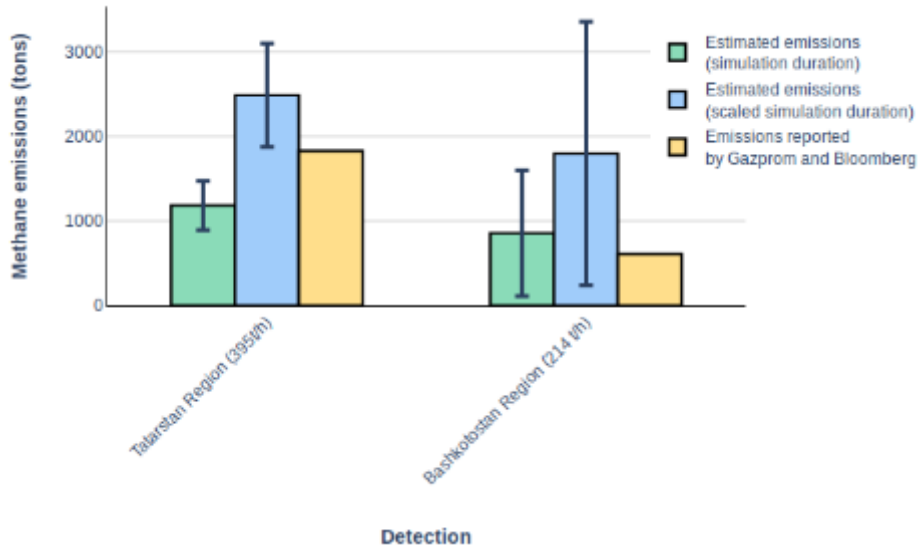

Figure 3-3 Comparison of TROPOMI-based methane flux rates with ground-based measures

3.1.4. COMPARISON TO SPANISH E-PRTR ESTIMATES

The CH_4 point sources detected for Spain in 2021 were compared against E-PRTR official estimates. There are a total of 4 sources reported for Spain, 3 located in Madrid and 1 in Murcia. Flux emission rates were successfully estimated only for the detection in Murcia (4.49 t/h), while for the 3 detections in Madrid the fluxes could not be retrieved due to issues with data quality and/or unfavourable meteorological/atmospheric conditions (e.g., wind speed too high or too low, typically > 5m/s or <2

m/s). The four sources detected are related to waste management activities, mainly landfills. The three identified CH_4 sources in Madrid spatially coincide with the top 1 and top 3 E-PRTR CH_4 emitters (< 5km), while the CH_4 point source retrieved in Murcia is 22km away from the E-PRTR Spanish top 2 emitter and 11km from the top 14 emitter (Figure 3-4). Considering the typical spatial uncertainty observed on the source location from CH_4 inverse estimates (i.e., 15km and up to 50km in the worst cases), it is likely that the retrieved emission rate in Murcia is related to these two sources. Assuming that the flux rate retrieved in Murcia is constant through the year, the inverse CH_4 estimate is 67% larger than the sum of annual emissions reported by the two E-PRTR facilities.

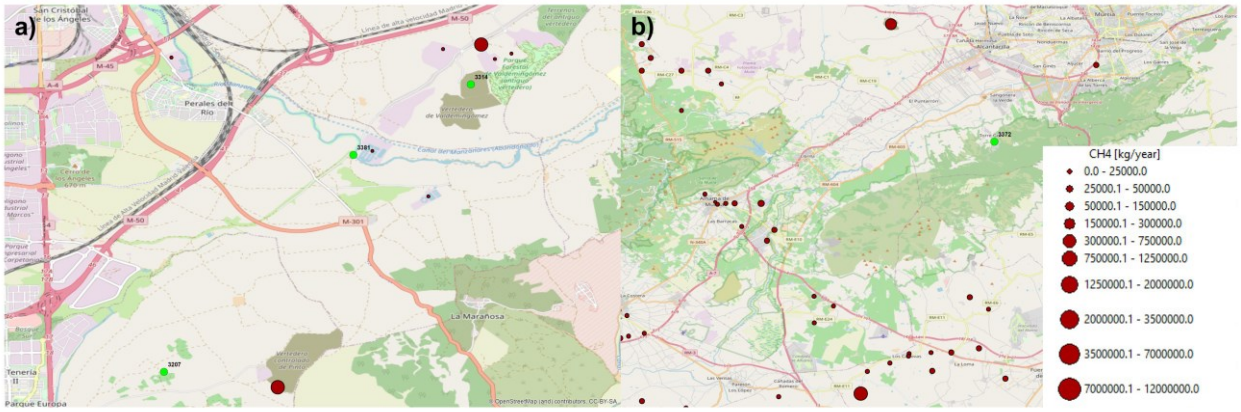

Figure 3-4 Representation of the top down (in blue) and E-PRTR (in red) CH_4 point sources detected for Madrid (a) and Murcia (b) (Spain).

3.1.5. SUMMARY

Table 3-2 Inter-comparison assessment table: CH4- point source emissions

CH_4 – point sources emissions	
Specie	CH_4
Target level region	Point source emissions
Target geographic region	Worldwide, subject to satellite data availability and availability of ground truth data
Type of Validation	Qualitative and quantitative comparison
Parameter(s) to be validated / Test objective	Emission flux rate
Validation description/Method	Points will be compared one-for-one against state-of-the-art research paper which provide satellite-based point sources emissions detections and quantifications. Comparison will also be compared to the very few existing ground-truth data for large methane point source emissions. Statistics (mean absolute error, mean relative error, bias, standard deviations) will be generated on the differences of flux rate retrievals between our method and other methods, and between our estimates and "ground-truth" measures.
Validation data	Varon et al. 2019 (GHGSat and TROPOMI measures), Ehret et al. 2022 (Sentinel-2 measures), ground truth when available in Bloomberg articles, Spanish E-PRTR database
Time period	2019-2021
Extrapolation to other regions	-
Comments	Given the very poor availability of ground truth data, validation will mainly focus on comparing results with state-of-the-art research papers.
Results	Our point-source inversion in Turkmenistan have been compared with [RD.12]. They show consistent result for the month and days of overlap between our study and [RD.12]. Likewise, [RD.11] can be used to compare our TROPOMI-based estimates with methane plume flux rate estimates based on Sentinel-2 methane detection capabilities. On a particular example [RD.11] in Kazakhstan on the 21st of September 2020, we find both

CH_4 – point sources emissions

estimates in the same order of magnitude, although the relative difference of more than 40% can be explained by various factors (change in emission rate between both satellite overpasses, sensitivity of the measure).

The following table wraps up the comparison of our flux rate estimates with those from the scientific literature in Turkmenistan and Kazakhstan:

Metric	Value
Mean of absolute differences	19.0 metric tons per hour
Mean of relative differences	19.0%
Standard deviation of absolute differences	18.8 metric tons per hour
Standard deviation of relative differences	16.3%
Absolute bias	8.5 metric tons per hour
Relative bias	7.2%
Mean uncertainty radius	27.3 metric tons per hour
Mean relative uncertainty radius	45% [RD.7]

These figures show a relative difference below 20% between third-part research papers and our results. This is significantly below the mean relative uncertainty on the flux rate estimates (45% [RD.7]). Likewise, the bias between our estimates and third-party estimates can be considered as non-significant as it is significantly lower than the mean relative uncertainty (7.2%). These figures, which are consistent with what can be found in third-party research papers, overall emphasize that the estimates are to be considered as orders of magnitude of the flux rates rather than as exact quantifications. On a specific, extreme emission event, we also find consistent flux rates with those derived by geostationary satellite data from GOES-R.

We compared our measure to ground-based emission figures provided by an oil and gas operator. Making reasonable assumptions of the emission duration, we also find that our estimates fall in the same order of magnitude as ground-based figures.

Last, we compared the point sources detected for Spain in 2021 against E-PRTR official estimates. The 4 sources reported are located in Madrid (3) and Murcia (1), all of them close to the top 3 E-PRTR CH_4 emission sources.

Both validation processes (against space borne measures and reported data) show consistency between our estimates and third-party numbers. Although sometimes significant, the difference between our numbers and other space borne or reported data are mostly contained within the uncertainty intervals. This validates the relevance of our approach to estimate the order of magnitude of the detected point source emissions.

3.2. POINT SOURCE EMISSIONS FROM INVERSION MODELS FOR CARBON DIOXIDE (CO2)

3.2.1. GENERAL

This product is provided by the EC Copernicus CoCO2 project in which it is directly evaluated. We copy here the corresponding documentation in CoCO2's D6.6 "Fitness for Purpose Document".

The method was developed by [RD.14] and [RD.13], [RD.15] who could demonstrate its skill. In particular, they compared their results with a global gridded and hourly inventory. They found that the corresponding OCO-2 and OCO-3 emission retrievals explain more than one third of the inventory variance at the corresponding cells and hours. Further, they binned the data at diverse time scales

from the year (with OCO-2) to the average morning and afternoon (with OCO-3), and saw consistent variations of the median emissions, indicating that the retrieval-inventory differences (with standard deviations of a few tens of percent) are mostly random and that trends can be calculated robustly in areas of favourable observing conditions, when there is enough data.

The implementation of the algorithm is very similar to the one of [RD.15] and the analysis of temporal variability has therefore not been repeated. The main change consisted in replacing the Emissions Database for Global Atmospheric Research (EDGAR), v6.0, used for the enhancement selection, by the coal-fired power plant and steel plant data from the Global Energy Monitor (https://globalenergymonitor.org/). The advantage of this database is its monitoring of the plants much closer to real time than EDGAR (months behind real time rather than years). It is restricted to coal-fired power plants and steel plants, but [RD.15] noticed that the isolated enhancements selected in the OCO data originated mostly from large emitters in the power-industry sector and, to a smaller extent, in the combustion-for-manufacturing sector; the other sectors, like road transport, had a smaller share. By using the Global Energy Monitor data rather than EDGAR, we also lose the sub-annual temporal variability of this dataset, in particular for emissions from the power sector, but we assume that when an OCO sees a coal-fired power plant plume, this plant operates at the maximum of its capacity.

This evolution of the production chain and the data that it generated have been quality-controlled by a comparison between the retrieved emissions and those of the Global Energy Monitor cumulated in the footprint of each emission retrieval and assuming a capacity factor of 100% at observation time. This comparison is shown in Figure 3-5 in the case of the OCO-2 data, v11. 424 enhancements have been selected by the automated algorithm. The cloud of points overall stretches along the bisector, with a slope of 0.91 and an r^2 of 0.42. The figure actually displays the cloud of points with both axes on logarithmic scales because the retrieval values are distributed heterogeneously over three orders of magnitude. If we take the logarithm of the emissions, as is done in practice in the figure, r^2 increases up to 0.53; the slope is then 0.83. There is usually more than one large emitter in the plume footprint and the agreement is for the total, not for one specifically. For OCO-2 v10 data, 304 enhancements have been selected by the automated algorithm, over longer period of time than that allowed by v11. The r^2 is of 0.44 and 0.42, without and with logarithm scale, respectively. For OCO-3 data, 65 enhancements have been selected by the automated algorithm. The r^2 is of 0.42, either with or without logarithm scale.

These r^2 values are larger than those reported in [RD.15] when comparing the emission retrievals to EDGAR, despite the lack of temporal variability in the plant emissions and the lack of neighbouring emissions from other sectors, when using the Global Energy Monitor.

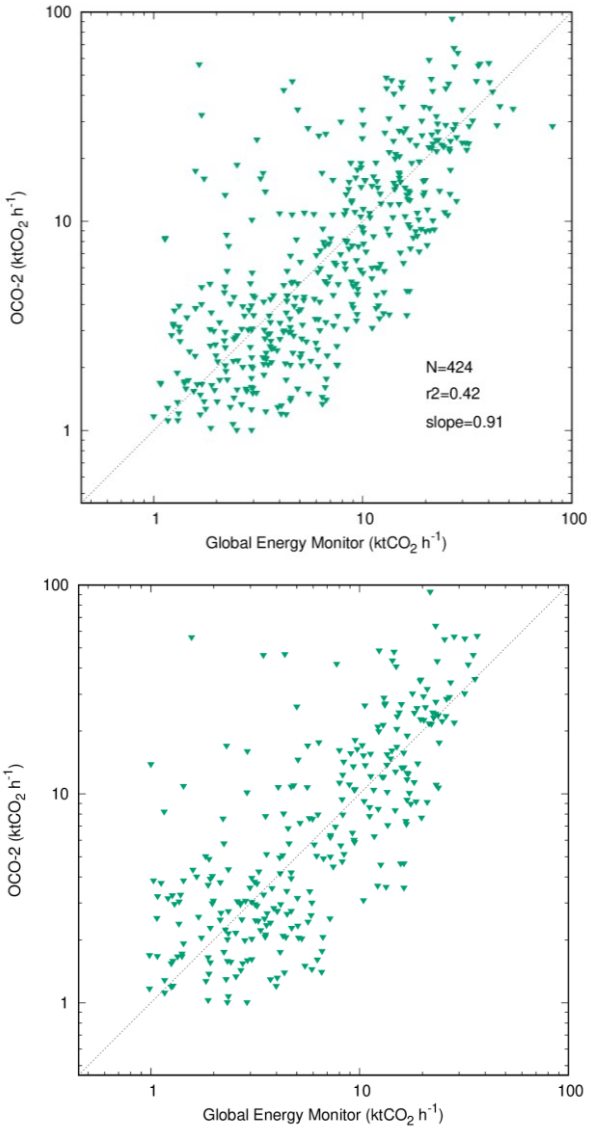

Figure 3-5 Retrieved emission values for OCO-2 v11 data versus the values inferred from https://globalenergymonitor.org/. The black dots form the bisector.

3.2.2. SUMMARY

Table 3-3 Inter-comparison assessment table: CO2- point source emissions

CO_2 - point source emissions	
Specie	CO_2
Target level region	Point source
Target geographic region	Globe
Type of Validation	Qualitative
Parameter(s) to be validated / Test objective	Precision and trueness
Validation description/Method	The product has been already evaluated in the EC Copernicus CoCO2 project by comparison to independent inventories (EDGAR v6.0 and Global Energy Monitor). As the product is simply extended in time but its algorithm not evolving, and because of the lack of evaluation data for this type of pioneer product, no further evaluation is planned at this stage.

CO_2 - point source emissions	
Validation data	EDGAR v6.0, Global Energy Monitor
Time period	Full archive
Extrapolation to other regions	No
Comments	N/A
Results	We see consistent variations of the median emissions between the emission retrievals and the global gridded and hourly inventory EDGAR v6.0, indicating that the retrieval-inventory differences (with standard deviations of a few tens of percent) are mostly random. We also see a significant correlation (r2 ~0.4) with the inventory data, despite large uncertainty in the latter at this scale.

3.3. POINT SOURCE EMISSIONS FOR NITROGEN OXIDES (NOX) AND SULPHUR DIOXIDE (SO2)

3.3.1. NOX POINT SOURCE EMISSIONS

NO_x point source emissions were identified and localized based on the temporal mean of the advection A^*, i.e., the scalar product of horizontal wind fields and the gradient of NO_2 VCDs (A), corrected for topography (*). The respective emissions were derived by spatial integration within 15 km radius. The resulting catalogue of point source NO_x emissions (v2) is publicly available [RD.25] and described in detail in [RD.26]. Below we validate the derived NO_x emissions by comparison to regional emission datasets.

3.3.1.1. Germany

We compare the NOx emissions of the catalog v2 to PRTR emissions reported by UBA for Germany [RD.27]. For all 13-point source emissions over Germany listed in the catalogue v2, matches PRTR sources were found. As PRTR emissions are reported on annual basis (available for 2018-2020), we compare the annual catalog emissions to the integrated PRTR emissions within 15 km for the respective year.

In Figure 3-6, the catalogue emissions are compared to matching PRTR emissions. A Pearson correlation coefficient of 0.81 was found between annual emissions from catalog v2 and PRTR. The ratio of mean catalogue to mean PRTR emissions over all point source emissions and years was found to be 1.19.

For several point source emissions, however, interference with other emissions (in particular from traffic) have to be expected due to nearby cities, causing a high bias of the catalog emissions. Thus, we also performed a comparison only for point source emissions without large cities nearby. This selection of six-point sources (mostly lignite power plants) increases the correlation to 0.96, while the ratio of emissions decreases to 0.83, i.e., catalogue emissions are on average 17% lower than those reported in PRTR.

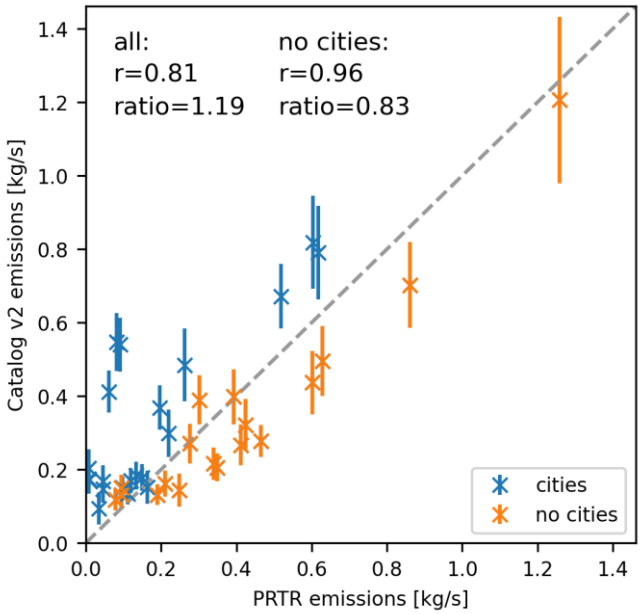

Figure 3-6 Comparison of annual mean NOx emissions from catalog v2 (y-axis) to emissions reported in PRTR, added up within 15 km radius (x-axis), for Germany. Error bars reflect the errors given in the catalogue v2. Correlation coefficients r and the ratio of mean emissions (v2 versus PRTR) are provided in the figure based on all found point source emissions as well as for the subset excluding point source near emissions cities.

The highest annual emissions of 1.2 kg/s were found for the lignite power plants Niederaußem and Neurath, catalogue rank #71, in the year 2018. In 2019 and 2020, these emissions decreased to 0.7 kg/s and 0.5 kg/s, respectively, in the catalogue. This decrease is also reflected in the annual maps of *A** ([Figure 3-7]). A similar reduction is reported in PRTR as well.

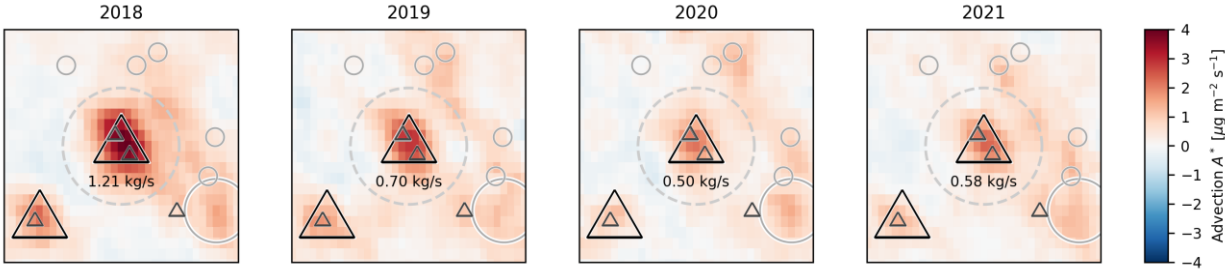

Figure 3-7 Maps of annual mean A* for catalogue rank #71 (51.0125° N, 6.6375° E), corresponding to the lignite power plants Niederaußem and Neurath. Large triangles and circles indicate the location of point source and area source emissions, respectively, based on the classification algorithm described in [RD.26]. Small triangles and circles mark the location of power plants and cities. The dashed circle indicates the integration radius of 15 km.

3.3.1.2. USA

The eGRID dataset [RD.28] lists NO_x emissions related to power generation but does not cover other NO_x sources from cement plants or metal/chemical/mineral industries. Thus, it has to be expected that the catalogue emissions are higher than those reported by EPA whenever significant emissions from cities or industrial activities other than power generation occur within 15 km.

For a meaningful comparison between catalogue v2 and eGRID, we thus focus on

- point source emissions that do not coincide with a large city, and

- eGRID emissions above the derived detection limit, i.e., 0.11 kg/s.

This selection keeps 41-point source emissions. Figure 3-8 displays the corresponding comparison of annual NO_x emissions between eGRID and catalogue v2, resulting in a correlation coefficient of 0.64,

and a ratio of mean emissions of 0.78. In some cases, catalogue emissions are larger than those reported by eGRID, probably due to interfering emissions from sources other than power plants. In few cases, the catalogue emissions are considerably lower than eGRID.

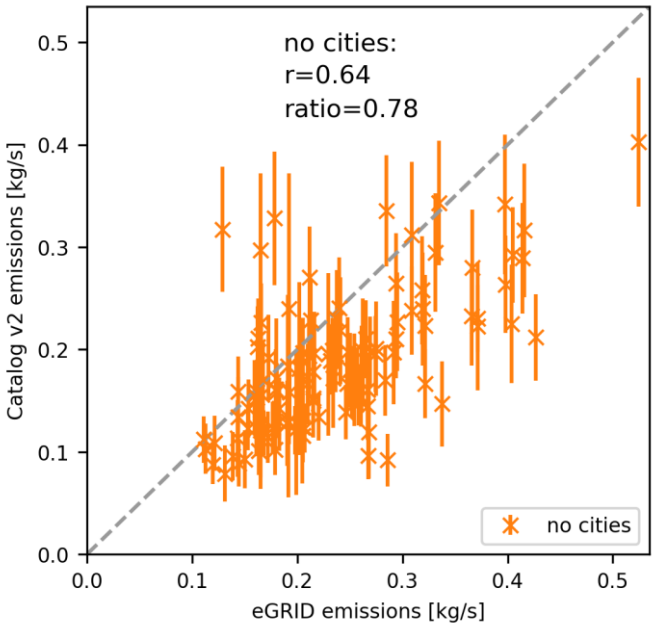

Figure 3-8 Comparison of annual mean NOx emissions from catalogue v2 (y-axis) to emissions reported in eGRID, added up within 15 km radius (x-axis), for the USA. Point source emissions close to cities are skipped, as well as eGRID values below 0.11 kg/s. Error bars reflect the errors given in v2. Correlation coefficients r and the ratio of mean emissions (v2 versus eGRID) are displayed in the figure.

The Navajo power plant was one of the top NOx emitters in 2019 but is only listed at rank #890 in the catalogue v2. This is due to the shutdown of the Navajo power plant end of 2019. This shutdown is well reflected in the annual emissions in v2 of the catalogue (Figure 3-9).

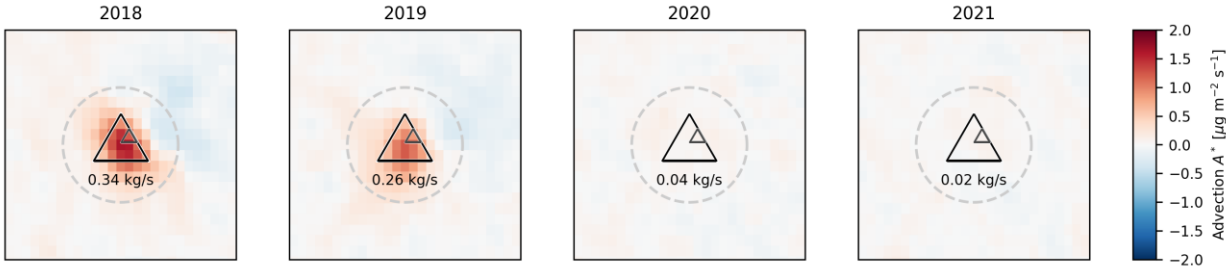

Figure 3-9 Maps of annual mean A* for catalogue rank #890 (36.8875° N, 111.4125° W), corresponding to the Navajo coal power plant. The shutdown end of 2019 results in emissions close to zero in 2020 and 2021.

3.3.1.3. Spain

We compare the NOx emissions of the catalog v2 for the year 2019 to the HERMESv3 Spanish point source database, which includes information of industrial emissions from the national LPS and PRTR databases. As done for Germany, we compare the annual catalog emissions to the integrated local emissions within 15km (Figure 3-10). There is a total of 6 point sources identified for Spain in the catalog, three of them located in the peninsular Spain and three others in the Canary islands. The three sources identified in the peninsular Spain (i.e., ranks 434, 526 and 1012) are located in large, industrialised regions close to port areas (i.e., Bilbao, Gijon and Cartagena), which could explain why the satellite-derived emissions tend to be larger than the HERMESv3 results. Two of the three point sources located in the Canary Islands (i.e., ranks 395, 508) coincide with the top two NO_x Spanish emitters according to HERMESv3; the Punta Grande and Salinas oil-fired power plants. For these two

sources, a good agreement between the catalog v2 and HERMESv3 is observed (differences of -13% and -6%, respectively). The third and last point source in reported by the catalog in the Canary Islands (i.e., rank 451) is located next to the port of Santa Cruz de Tenerife, where no relevant industries can be identified within 15km. Therefore, it is likely that this source from the catalogue is mainly reporting emissions from the shipping activity in this port, which is the largest in Spain in terms of sea passengers.

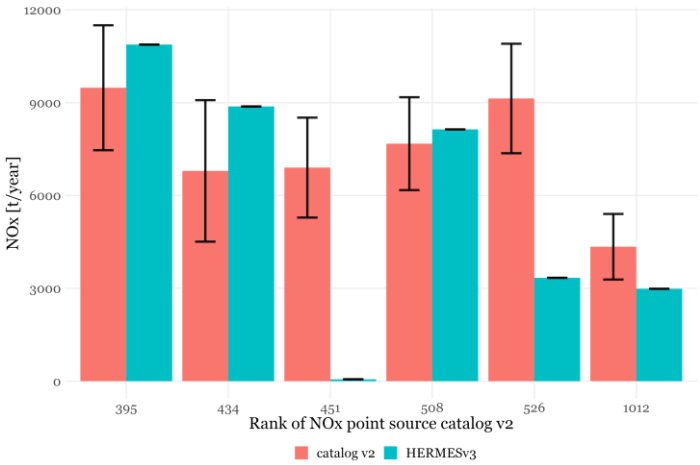

Figure 3-10 Comparison of annual mean NOx emissions from catalog v2 (red) to emissions reported in HERMESv3 (blue) added up within 15 km radius, for Spain. Error bars reflect the errors given in the catalogue v2.

3.3.2.NOX HOTSPOTS

3.3.2.1. TROPOMI

The TROPOMI estimate for NOx emissions and hotspots like megacities and conurbations are derived from a simultaneous fit of the observed VCD patterns for different wind directions (see the ATBD - document D3, [RD.3], for details). As this approach requires good sampling for multiple wind directions in order to retrieve robust estimates, strict selection criteria were applied, resulting in 100 hotspots (out of initially 700 megacities) where a valid estimate could be derived.

The emission estimate was performed for seasonal means. For the comparison to EDGAR, the seasonal hotspot emissions are averaged first in order to derive total emissions.

3.3.2.2. EDGAR

The hotspot emissions derived from TROPOMI are compared to EDGAR emissions. Here we use gridded EDGAR data (0.1° grid), version 6.1, for the year 2018.

For each hotspot, the gridded EDGAR emissions are integrated within +/- 50 km in x and y, corresponding to the distance of 50 km used for the calculation of line densities (cross-wind) as well as for the integration of total emissions (along-wind).

3.3.2.3. COMPARISON

Figure 3-11 displays a comparison of the derived emissions compared to EDGAR. Overall, the comparison is reasonable; the emissions from both data sources show a correlation of R=0.76. On average, the ratio TROPOMI/EDGAR is 1.0 (mean of individual ratios) and 0.84 (ratio of means), respectively.

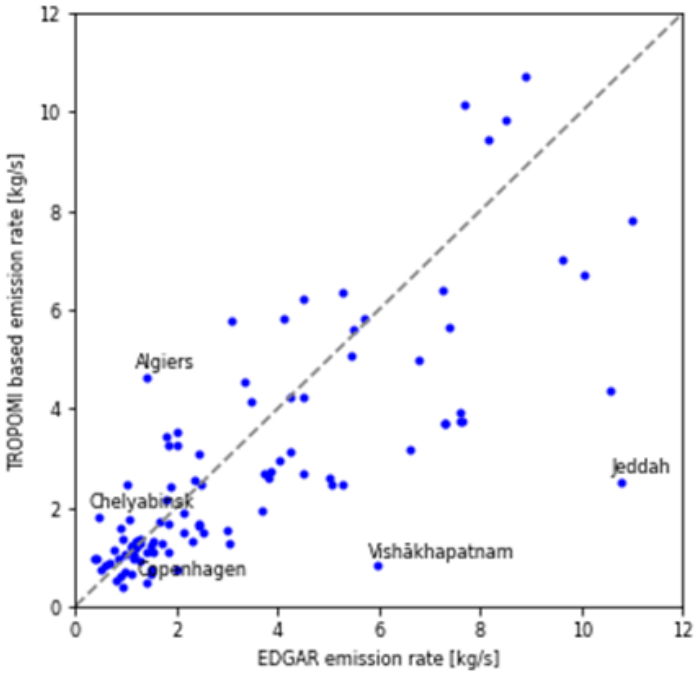

Figure 3-11 Scatter plot of hotspot emissions estimated from TROPOMI (y-axis) compared to EDGAR (x-axis). Hotspots with deviations by more than a factor of 3 or 1/3 are labelled.

3.3.2.4. DISCUSSION

There are some aspects that have to be kept in mind when interpreting the comparison to EDGAR:

- EDGAR emissions are provided for the year 2018, while the TROPOMI estimate is derived for the time range covered by PAL (2019-2022), thus deviations have to be expected in case of recent changes in emissions. This is particularly the case for the massive lockdowns in 2020 and 2021.
- The seasonal estimates were averaged for the comparison; however, since in most cases only 2 or 1 seasonal estimates are available, this average cannot be considered to be representative in case of strong seasonality.

3.3.3.SO2 POINT SOURCES

SO_2 point source emissions were also identified and localized based on the temporal mean of the advection A* (see section 3.3.1). The respective emissions were derived by spatial integration within 15 km radius. Below, we validate the derived SO_2 emissions by comparison to a global emission dataset and regional emission reports.

3.3.3.1. INDIA

We compare the SO_2 emissions of the catalog to emissions reported by [RD.42] for India. A total of 48 point source matches have been found. As the SO_2 emissions in [RD.42] are reported on annual basis, we compare our total emissions for each point source in the catalog to the respective averaged emissions for the same time period.

In Figure 3-12, the catalogue emissions are compared to matching emissions in [RD.42]. A Pearson correlation coefficient of 0.82 was found between emissions from our catalog and [RD.42]. The ratio of mean catalogue to mean [RD.42] emissions over all point source emissions in India was found to be 1.36, i.e., our catalogue emissions are on average 36% larger.

However, interference from other emissions has to be expected for a number of point source emissions because of the presence of neighboring cities and power plants, leading to a bias of the catalog emissions.

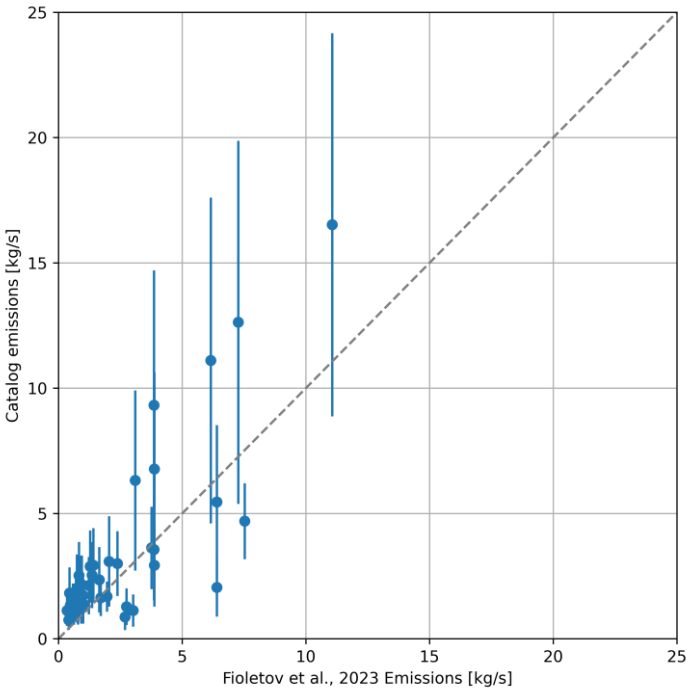

Figure 3-12 Comparison of total mean SO_2 emissions from catalog (y-axis) to emissions reported in [RD.42] (x-axis), for India. Error bars reflect the errors given in our catalogue.

3.3.4. SUMMARY

Table 3-4 Inter-comparison assessment table: SO_2 - point source emissions

SO_2 – point source emissions	
Specie	SO_2
Target level region	Point source
Target geographic region	India
Type of Validation	Qualitative & Quantitative
Parameter(s) to be validated / Test objective	Point source location Point source emissions
Validation description/Method	For each identified point source, the following comparisons will be performed: 1. The location of point sources will be compared to validation data 2. The emissions of point sources will be compared to validation data
Validation data	Fioletov et al., 2023
Time period	2018-2022 total mean and annual means
Extrapolation to other regions	-
Comments	Over Europe, SO_2 from point source emissions might be below TROPOMI detection limit.
Results	Point sources could be identified and localized very precisely. Point source emissions compare well to Fioletov et al., 2023 (R=0.82). Our estimates are about 36% higher for India.

Table 3-5 Inter-comparison assessment table: NO_x - point source emissions

NO_x – point source emissions	
Specie	NO_x
Target level region	Point source
Target geographic region	Point sources (globally)
Type of Validation	Qualitative & Quantitative
Parameter(s) to be validated / Test objective	Point source location Point source emissions
Validation description/Method	For each identified point source, the following comparisons will be performed: 1. The location of point sources will be compared to validation data 2. The emissions of point sources will be compared to validation data
Validation data	E-PRTR; eGRID; SASOL report, HERMESv3
Time period	2018-2021 total mean and annual means
Extrapolation to other regions	-
Comments	-
Results	Point sources could be identified and localized with an accuracy of about 2-3 km. Comparison to regional emission data reveals agreement of NO_x emissions within 20% on average.

Table 3-6 Inter-comparison assessment table: NO_x - hotspots

NO_x – hotspots (megacities and conurbations)	
Specie	NO_x
Target level region	Hotspots (megacities and conurbations)
Target geographic region	Megacities and conurbations (globally)
Type of Validation	Quantitative
Parameter(s) to be validated / Test objective	Total NOx emissions
Validation description/Method	Comparison of total NO_x emissions to bottom-up inventories
Validation data	EDGAR v6.1 for 2018
Time period	2018-2021 seasonal means
Extrapolation to other regions	-
Comments	NOx emissions and effective lifetimes will be derived for seasonal means. Due to unfavourable viewing conditions in winter, a higher uncertainty and potential bias has to be expected for winter estimates.
Results	Hotspot emissions compare well to EDGAR v6.1 (R=0.76). On average, the TROPOMI-based estimates are about 16% lower compared to EDGAR, which might be related to the lockdown measures in 2020/2021. .

3.4. POINT SOURCE EMISSIONS FROM INVERSION MODELS FOR ETHYLENE (C2H4), ACETYLENE (C2H2), AMMONIA (NH3) AND METHANOL (CH3OH)

To the best of our knowledge, the state-of-the-art EDGAR v4.3.2 anthropogenic inventory [RD.24] is the only database available providing gridded bottom-up emission fluxes of C_2H_4 and C_2H_2 at the global

scale. The EDGAR emissions are provided at a spatial resolution of 0.1° × 0.1° for several NMVOC species, including C_2H_4 and C_2H_2, and for different sectors. To calculate the EDGAR bottom-up emissions of such compounds, speciation profiles were applied to disaggregate the total NMVOC emissions available in existing databases (e.g., national emission inventories) into sector-specific emissions of individual NMVOCs (or of similar NMVOCs lumped together). This disaggregation is a significant source of uncertainties in the EDGAR fluxes, first because of the lack of speciation profiles representative for all the emission sectors, types of fuels, and geographical areas, and also because of the large uncertainties associated with the total NMVOC emissions on which the speciation profiles are applied. Therefore, the following results should not be interpreted as a validation of the IASI-derived emissions of C_2H_4 and C_2H_2, but rather as an inter-comparison.

For C2H4, IASI-derived point source emissions were also compared to the bottom-up estimates provided for Spain by the HERMESv3 system [RD.43]. The system combines total NMVOC annual industrial emissions derived from the Spanish LPS and PRTR databases with state-of-the-art and activity specific NMVOC speciation profiles reported by [RD.44]. The comparison was performed for the two point sources detected with IASI in Spain, which are located in the refinery and petrochemical industrial complexes of Puertollano and Tarragona, respectively.

We are not aware of other emission data, nor emission estimates derived from spaceborne or ground-based measurements, that could be used for the purpose of a validation exercise of the IASI-derived NMVOC emissions over anthropogenic point source emissions.

For the NH3 and NMVOC point sources, we present top-down emission fluxes averaged over the entire 2008-2021 IASI time series. In the case of NH3 point sources, we also provide annual emission fluxes. Based on these annual fluxes, we have observed that the emissions remain relatively constant throughout the time series for most of the point sources. However, significant variations in the emissions of a point source can occur, for example, following the opening or closure of an industry or factory, the expansion of industrial or agricultural activities, or the implementation of new technologies aimed at reducing gas leaks and pollutant emissions.

3.4.1.ETHYLENE (C2H4) POINT SOURCE EMISSIONS

The following results obtained for C_2H_4 have been published recently in [RD.23]. In total, the emissions from 57 global point source emissions of C_2H_4 were quantified with the IASI measurements, representative of the different source categories and the global distribution of hotspots identified from space. The annual top-down fluxes analysed here were derived from the averaged IASI data over the 2007-2020 time period. For these point source emissions, we calculated the C_2H_4 emission fluxes prescribed by EDGAR v4.3.2, using the data for the most recent available years (2010–2012). For each of the selected hotspots, we computed the C_2H_4 fluxes by summing up the contribution of the EDGAR pixels located over and in the direct vicinity of the presumed point source emissions. An example is displayed in Figure 3-13 for the C_2H_4 point source emissions detected by IASI over the petrochemical cluster of Mundo Nuevo (Mexico). Figure 3-13a shows the IASI column distribution over the point source emissions (delimited in white) and the area used to calculate the C_2H_4 background level shaded in semi-transparent. Figure 3-13b shows the IASI distribution after subtracting the background column. The 2010-2012 EDGAR emission fluxes of C_2H_4 are displayed in Figure 3-13c and Figure 3-13d. The pixels inside the red square are used to calculate the EDGAR emissions. The typical C_2H_4 point source emissions being isolated, the contribution of the pixels around the hotspot is small. However, other sources close to the presumed emitter might also contribute to the C_2H_4 enhancement detected by IASI, especially in a large industrial or urban area. Therefore, we also accounted for the EDGAR pixels directly around the point source emissions. The EDGAR C_2H_4 fluxes are available for 16 emission sectors [RD.24]. Because most point sources emissions identified from space are related to heavy industries, we calculated the EDGAR fluxes over all these sectors as well as over the industrial sectors only (e.g., oil refineries, fuel exploitation, transformation industry, power industry).

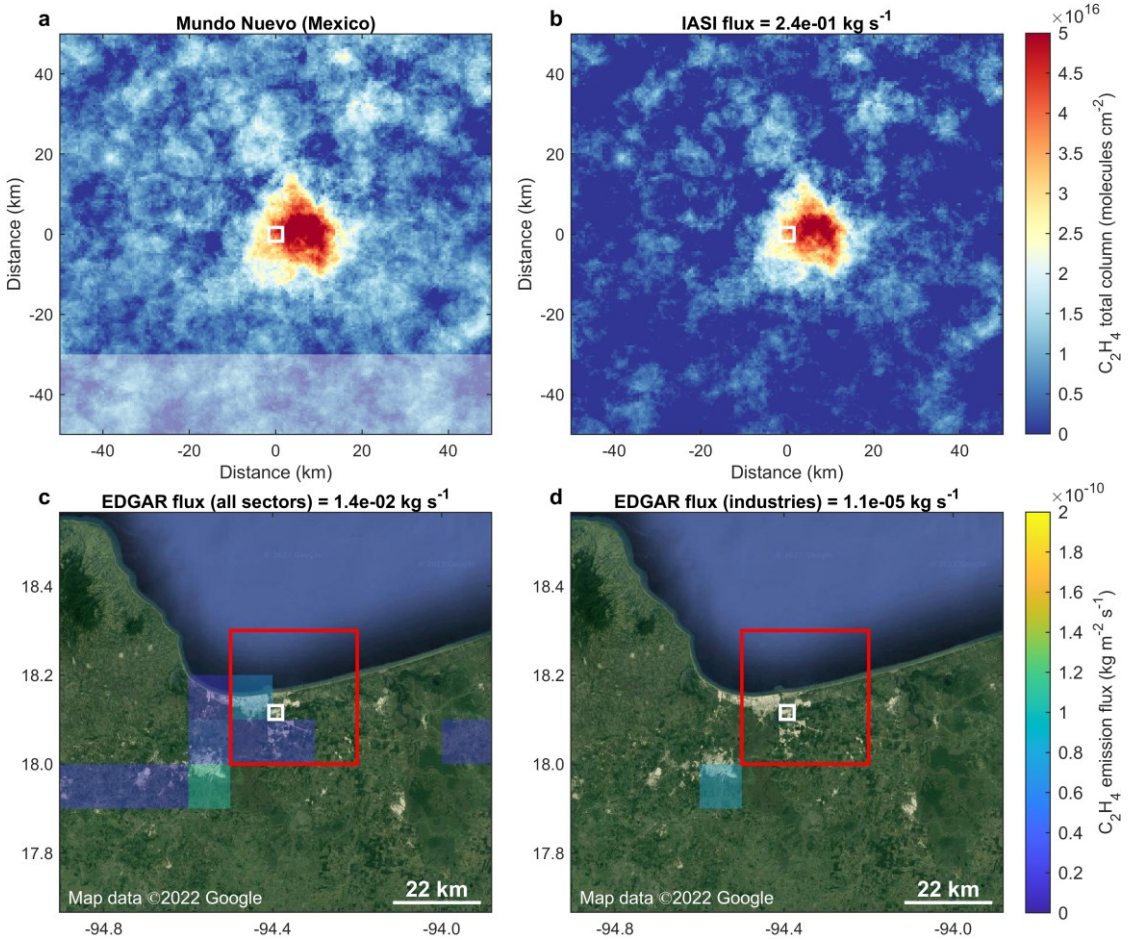

Figure 3-13 Example of C2H4 flux calculation over Mundo Nuevo, Mexico (adapted from [RD.23])

The comparison between the IASI-derived and EDGAR emissions of C_2H_4 is summarized in Figure 3-14a. It appears that the top-down fluxes are largely underestimated by the EDGAR emissions taken from all the sectors together; ~50% of the IASI hotspots are underpredicted by at least one order of magnitude). The discrepancy is even larger for a comparison involving only the industrial sectors of EDGAR; ~75% and ~38% of the hotspots are underestimated, respectively, by at least one and two orders of magnitude. It is likely that these biases are even larger since IASI tends to underestimate the gas content in the lowermost tropospheric layers.

Beyond these discrepancies on the emission fluxes, important mismatches between IASI and EDGAR are observed too. First, for 35 (66%) out of the 53 industrial C_2H_4 hotspots detected by IASI and studied here, EDGAR predicts no or negligible industrial fluxes. For instance, this is the case for the hotspot corresponding to the Dahej petrochemical hub (Gujarat, India) displayed in Figure 3-14b. This indicates that major industrial hotspots are absent in the anthropogenic inventory. Another genre of mismatch is represented in Figure 3-14c; the type and magnitude of C_2H_4 fluxes from the strong emitter – here, the industrial Fangshan District (Beijing, China) – are misrepresented by EDGAR since the predicted emissions there are dominated by the transport and residential sectors. This issue likely stems – at least partially – to the difficulty of bottom-up inventories to disaggregate total NMVOC emissions into spatially resolved fluxes of C_2H_4 (and of other NMVOCs) because the speciation profiles are often uncertain and fragmentary [RD.23]. The example in Figure 3-14c also highlights a limitation of the top-down emissions. Indeed, EDGAR predicts large C_2H_4 releases from the megacity of Beijing, which are not really captured by IASI. This occurs for other megacity hotspots worldwide. In urban environments, the potential C_2H_4 emission sources are many (e.g., road traffic, domestic heating), but typically of lesser intensity than the concentrated fluxes emitted from industrial areas. Consequently, the C_2H_4 releases in urban area are more diffuse and more difficult to detect from space.

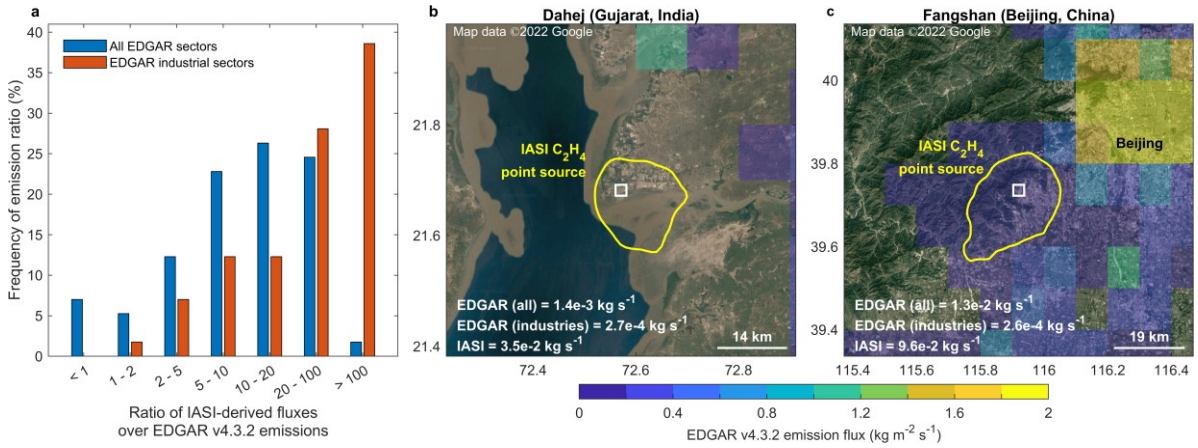

Figure 3-14 Comparison between IASI-derived and EDGAR v4.3.2 emission fluxes of C2H4 (taken from [RD.23])

Figure 3-15 shows the comparison between C2H4 annual emissions derived with IASI and estimated with HERMESv3 for the refinery and petrochemical industrial complexes of Puertollano and Tarragona, respectively. IASI annual emissions were computed by assuming that the satellite-based emission flux is constant throughout the year. For the comparison we considered the HERMESv3 bottom-up industrial emissions within a radius of 15km around the latitude-longitude coordinates of each IASI-derived point source. This choice was made since IASI-derived point sources detected in Spain have typically a spatial extent of 20-25km with the satellite data. Results show a very good agreement between emission estimates in the Puertollano area (3% differences), whereas discrepancies are significant in the case of Tarragona, IASI reporting approximately 4 times more emissions than HERMESv3. The larger differences observed in Tarragona could be related to the variety of industries that are in this complex when compared to Puertollano, where only a refinery is operating, and a larger uncertainty in the underlying emissions and speciation profiles considered. The total amount of NMVOC emissions estimated by HERMESv3 in Tarragona is 5740 t/year, which is almost equals to the total amount of C2H4 derived with IASI (5456 t/year).

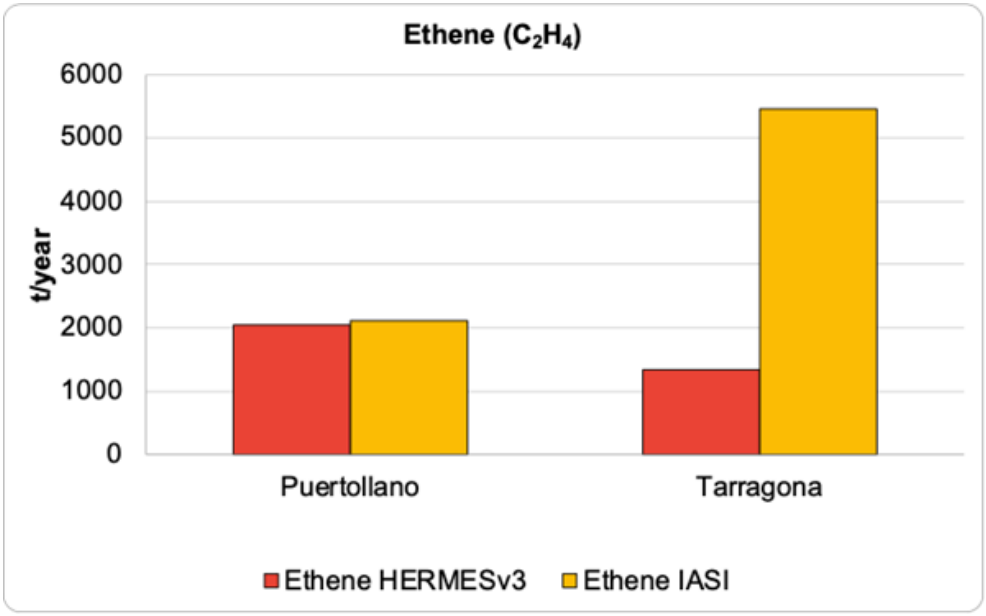

Figure 3-15 Comparison between IASI-derived and HERMESv3 annual emissions of C2H4 in the point sources of Puertollano and Tarragona (Spain).

3.4.1.1. SUMMARY

Table 3-7 Inter-comparison assessment table: C_2H_4 - point source emissions

C_2H_4 – point source emissions	
Species	Point source
Target level region	Global and Spain
Target geographic region	Qualitative and quantitative
Type of Validation	Location and emission strength
Parameter(s) to be validated / Test objective	Points will be compared one-for-one, statistics will be generated on the % of missing or excess point source emissions in the inventory.
Validation description/Method	EDGAR v4.3.2 anthropogenic inventory (https://edgar.jrc.ec.europa.eu) , HERMESv3
Validation data	Starting in 2008, as an average over the entire multi-year time period, depending on the availability of the EDGAR data
Time period	
Extrapolation to other regions	No
Comments	
Results	– The IASI-based fluxes of C_2H_4 have been calculated for 57 point sources, including primarily industrial point sources (e.g., petrochemical clusters, steel plants and coal-related industries). – The comparison with the EDGAR emissions reveals that ~50% of the IASI hotspots are underpredicted by at least one order of magnitude in the bottom-up inventory. The discrepancy is even larger for a comparison involving only the industrial sectors of EDGAR; ~75% and ~38% of the hotspots are underestimated, respectively, by at least one and two orders of magnitude. – For 66% of the industrial C_2H_4 hotspots detected by IASI and studied here, EDGAR predicts no or negligible industrial fluxes. – C_2H_4 releases in urban area are more diffuse and more difficult to detect from space. As a result, a limitation of the top-down emissions is that IASI does not capture well the more diffuse emissions from megacities such as Beijing, where EDGAR predicts large C_2H_4 releases. – The comparison for Spain against HERMESv3 bottom-up estimates indicates a very good agreement in one of the two identified point sources (differences of 3%) and large discrepancies in the other one (IASI-derived emissions 4 times larger than bottom-up estimates)

3.4.2.ACETYLENE (C2H2) POINT SOURCE EMISSIONS

Using the EDGAR v4.3.2 emission fluxes of C_2H_2 available for different sectors, the same type of analysis has been performed for the C_2H_2 hotspots detected by IASI. Due to the long lifetime of C_2H_2 and to the highly challenging retrieval of this species from satellite observations, only 17 point sources of C_2H_2 have been detected and identified with IASI. Moreover, the IASI-based fluxes could have been derived for only 13 of these point sources. As a result, no robust statistics can be extracted from the top-down vs. bottom-up comparison for C_2H_2.

Nonetheless, all the detected point sources are located in China and associated with the presence of coal-related industries (e.g., coal-fired power plants, coal mining and coke plants). Therefore, the following comparison offers a good assessment of the IASI-based fluxes of C_2H_2 using the EDGAR emissions (Figure 3-11). On average, the top-down emissions are one order of magnitude higher than the bottom-up emissions, suggesting a significant underestimation of the industrial EDGAR emissions for this species or point sources missing in the bottom-up inventory.

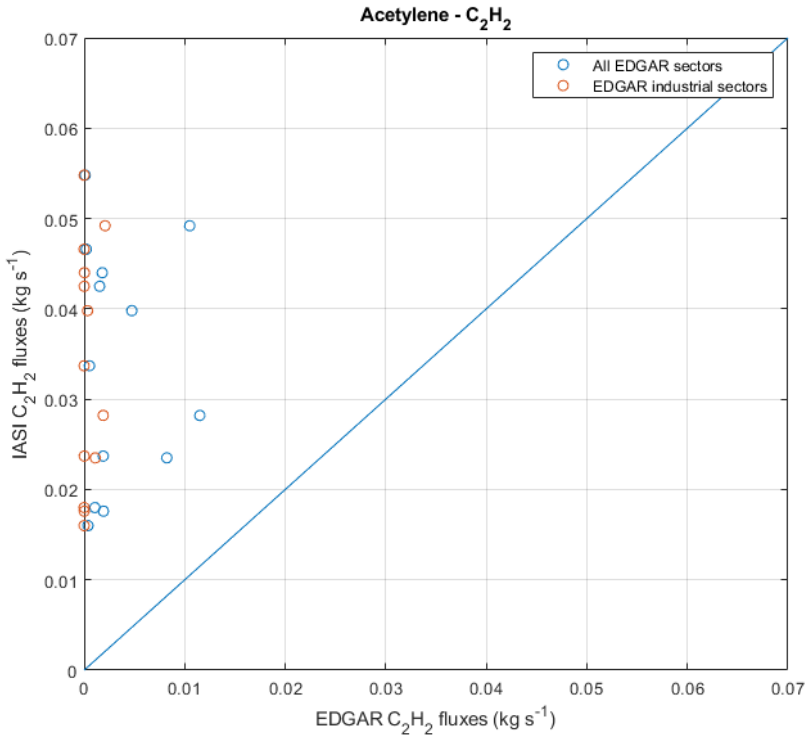

Figure 3-16 Comparison between IASI-derived and EDGAR v4.3.2 emission fluxes of C_2H_2.

3.4.2.1. SUMMARY

Table 3-8 Inter-comparison assessment table: C_2H_2 - point source emissions

C_2H_2 – point source emissions	
Species	C_2H_2
Target level region	Point source
Target geographic region	China
Type of Validation	Qualitative and quantitative
Parameter(s) to be validated / Test objective	Location and emission strength
Validation description/Method	Points will be compared one-for-one, statistics will be generated on the % of missing or excess point source emissions in the inventory.
Validation data	EDGAR v4.3.2 anthropogenic inventory (https://edgar.jrc.ec.europa.eu)
Time period	Starting in 2008, as an average over the entire multi-year time period, depending on the availability of the EDGAR data
Extrapolation to other regions	No
Comments	Considering the uncertainties associated with such bottom-up inventories for C_2H_2, this task should be considered as an inter-comparison. To our knowledge, only EDGAR applies speciation of the NMVOC at the global scale.
Results	– The IASI-based fluxes could have been derived for only 13 of point sources of C_2H_2 – All the detected point sources are in China and attributed to coal-related industries – On average, the top-down fluxes are higher by one order of magnitude than the EDGAR emissions, suggesting significant missing industrial emissions in the inventory.

3.4.3.AMMONIA (NH_3) POINT SOURCE EMISSIONS

3.4.3.1. SELF-CONSISTENCY CHECK

For each point source, the total average flux is reported, which is an average over the period 2008-2022 across the three different IASI instruments (onboard Metop-A, -B and -C). Yearly flux values are also reported. The total average is based on a windrotated supersampling approach [RD.49]. As this method is only suitable for very large datasets, we use the normal oversampled (but windrotated) average for the yearly fluxes. A consequence of using different calculation methods is, however, that the average of the yearly flux might deviate from the reported total average. Fortunately, it turns out that, except for a few outliers, the difference between the two is in fact small (mostly below 15%), as shown in the scatter plot and histogram below.

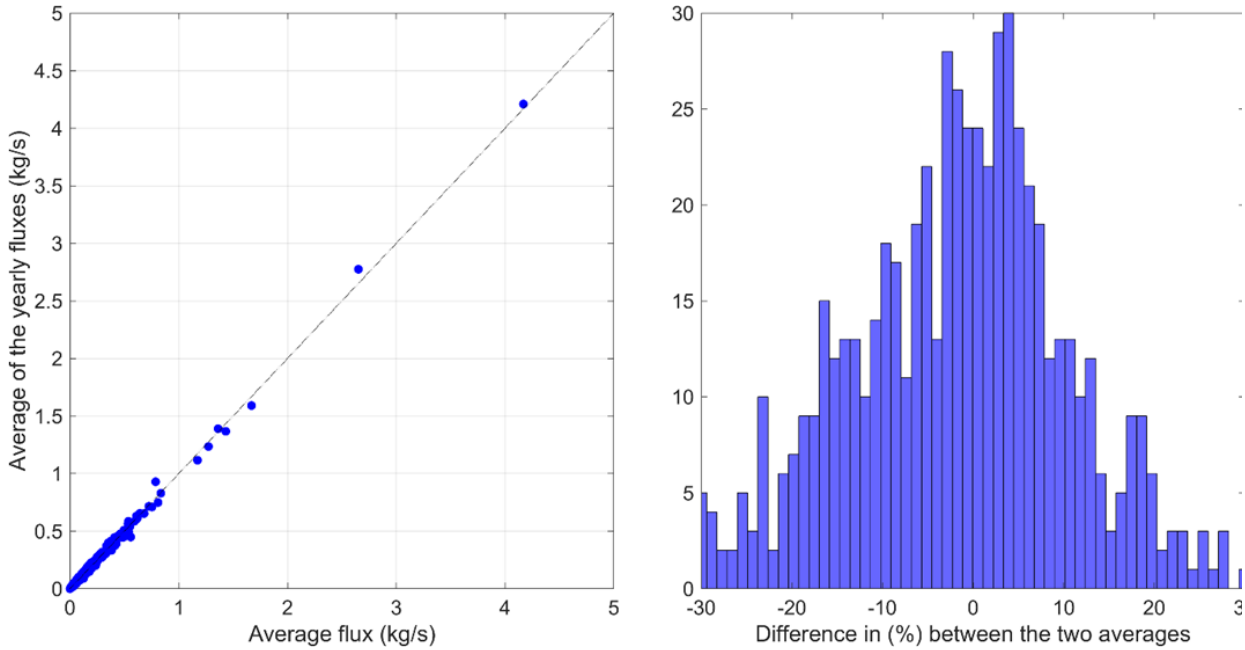

Figure 3-17 Comparison between total average flux values, and the average of the yearly flux values for all the reported IASI NH_3 point sources.

3.4.3.2. COMPARISON WITH THE E-PRTR INVENTORY

Validation data, in the form of independent measurement data, is extremely scarce. As for the regional emissions, we compare here the IASI derived NH_3 fluxes with a bottom-up inventory. For point-sources in Europe, there is the unique E-PRTR register (European Pollutant Release and Transfer Register). Both industrial and agricultural point sources are contained within. However, for the agricultural point sources, reporting across different European countries varies greatly. In addition, IASI's agricultural point sources consist mostly of a regional cluster of farms due to IASI's large footprint (~12-30 km). For that reason, we limit the comparison to industry related to chemical fertilizer production. These are the single largest industrial sources of NH_3 and known to be underestimated in bottom-up inventories [RD.16].

For the comparison, we selected from the European point sources identified by IASI, those categorized as "fertilizer industry". Their fluxes were then compared to the sum fluxes of all "chemical industry" E-PRTR point sources within the category in a 15 km radius. The result of the comparison is shown below. A weak correlation of R=0.33 is found, and as expected the reported fluxes are below the ones estimated by IASI (up to a factor 10). A similar comparison was conducted on a global scale with the EDGAR bottom-up inventory in [RD.16]. There, even larger differences were found, especially outside Europe, where many point sources were several orders of magnitude underestimated.

Note that for World Emission, the IASI point sources fluxes were calculated utilizing an atmospheric lifetime of NH_3 of 6 hours. There is a large uncertainty on this parameter, and the actual lifetime might

be as small as a few hours [RD.46]. The relation is inversely linear, so that a lifetime of e.g., 3 hours would result in a doubling of the estimated emissions (this is reflected in the error bars on the data points in the scatter plot below).

For one point source, SKW Stickstoffwerke Piesteritz (Germany), independent measurements are available from two aircraft surveys [RD.47]. They were estimated to be of the order of 0.05-0.07 kg/s. Considering the uncertainty on the NH_3 lifetime, these are in good agreement with the satellite-based estimates of 0.037 kg/s. The E-PRTR fluxes vary slightly from year to year but are significantly lower with a mean around 0.01 kg/s.

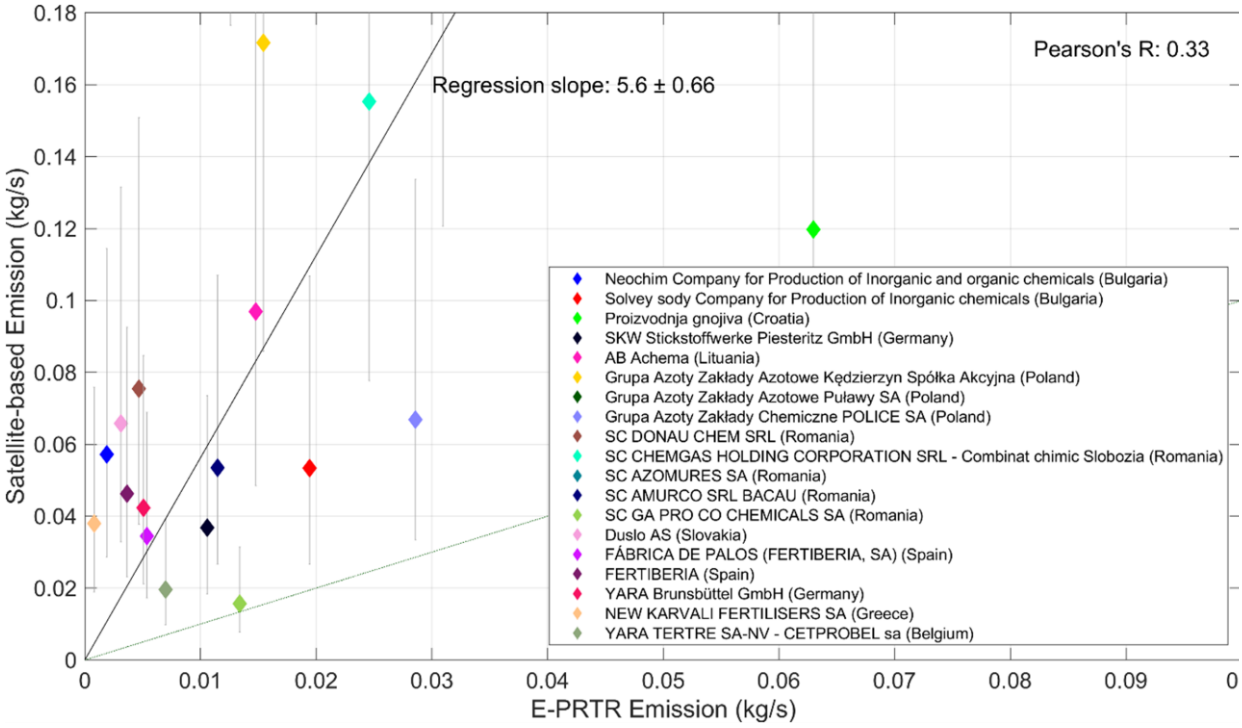

Figure 3-18 Comparison of IASI derived emission fluxes and EPRTR emission fluxes for fertilizer industry in Europe. Pearson's R and regression slope is also reported.

3.4.3.3. SUMMARY

Table 3-9 Inter-comparison assessment table: NH_3 - point source emissions

NH_3 – point source emissions	
Species	NH3
Target level region	Point source
Target geographic region	European
Type of Validation	Qualitative and quantitative comparison
Parameter(s) to be validated / Test objective	Emission strength
Validation description/Method	Points will be compared one-for-one, statistics will be generated on the % of missing or excess point source emissions in the inventory. For those point source emissions in common, numerical statistics will include parameters such as bias and standard deviation.
Validation data	European E-PRTR inventory (https://industry.eea.europa.eu/)
Time period	Selected year after 2008 depending on the availability of E-PRTR
Extrapolation to other regions	No

NH_3 – point source emissions	
Comments	Considering the uncertainties associated with such bottom-up inventories for NH3, this task should be considered as an inter-comparison.
Results	As expected the fluxes reported in the E-PRTR database are below the ones estimated by IASI, up to a factor 10. For one point source where fluxes derived from aircraft data are available, the IASI-derived emission estimate is in reasonable agreement, while E-PRTR also report lower values at that site

3.4.4. METHANOL (CH_3OH) POINT SOURCE EMISSIONS

Regarding the inter-comparison of methanol with independent emission estimates, as explained previously for C_2H_4 and C_2H_2, the only existing bottom-up inventory providing anthropogenic emissions of individual NMVOCs at the global scale is EDGAR v4.3.2. However, no fluxes specific to CH_3OH are available so far, only emissions for all the alcohol species lumped together are. Considering that methanol is the most abundant alcohol compound in the atmosphere, the top-down CH_3OH fluxes have been compared with the EDGAR emissions for all the alcohol species.

A limited number of CH_3OH point sources (32) are available for the derivation of emission fluxes from IASI. Those are mainly associated with the presence of chemical and petrochemical industries, and megacities. These top-down fluxes have been calculated from the averaged IASI data over the 2007-2020 time period following the method described earlier for C_2H_4. For these point source emissions, we calculated the alcohols emission fluxes prescribed by EDGAR v4.3.2, considering successively all the EDGAR emission sectors and only the industrial sectors (using the same method as for the other IASI-based products).

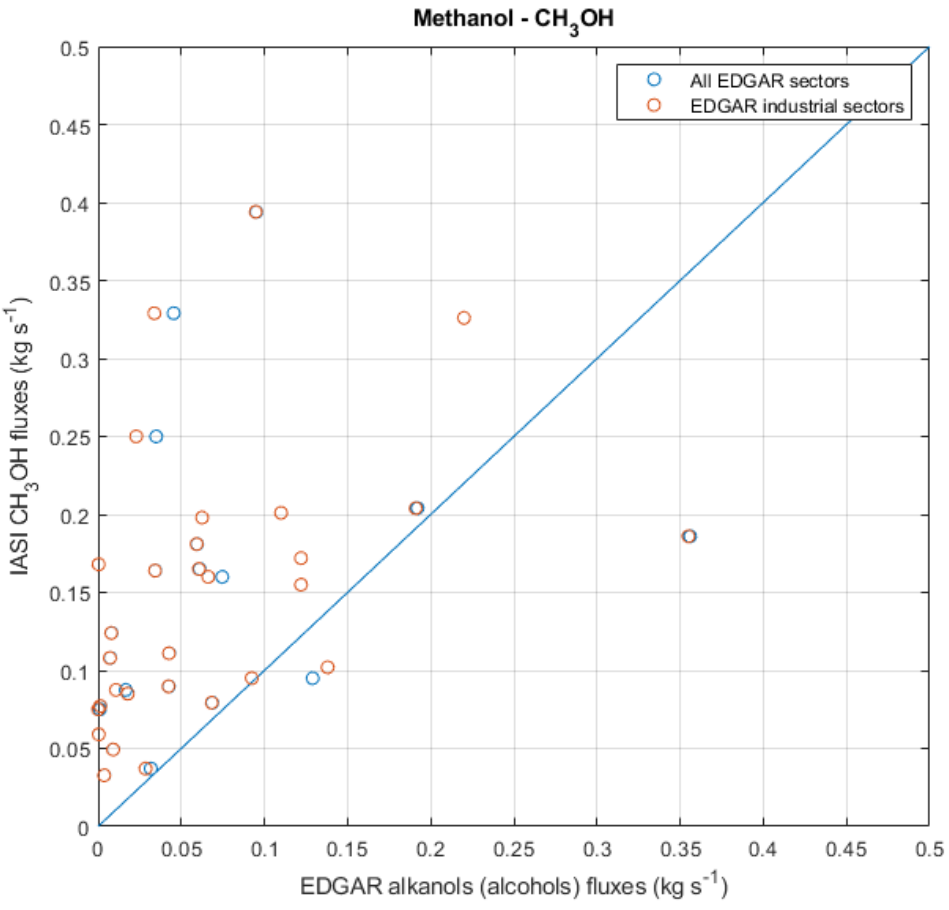

Figure 3-19 Comparison between IASI-derived and EDGAR v4.3.2 emission fluxes of CH_3OH.

3.4.4.1. SUMMARY

Table 3-10 Inter-comparison assessment table: CH_3OH - point source emissions

CH_3OH – point source emissions	
Specie	CH_3OH
Target level region	Point source
Target geographic region	Global, with a focus on point source emissions in Asia (China and India)
Type of Validation	Qualitative and quantitative
Parameter(s) to be validated / Test objective	Location and emission strength
Validation description/Method	Points will be compared one-for-one, statistics will be generated on the % of missing or excess point source emissions in the inventory.
Validation data	EDGAR v4.3.2 anthropogenic inventory (https://edgar.jrc.ec.europa.eu)
Time period	Starting in 2008, as an average over the entire multi-year time period, depending on the availability of the EDGAR data
Extrapolation to other regions	No
Comments	Considering the uncertainties associated with such bottom-up inventories for CH_3OH, this task should be considered as an inter-comparison. To our knowledge, only EDGAR applies speciation of the NMVOC at the global scale. The EDGAR v4.3.2 only provides emissions for the alcohol family as a whole, and not for CH3OH specifically. Methanol being by far the most abundant alcohol species in the atmosphere, the IASI-based CH3OH fluxes will be compared to this EDGAR dataset.
Results	- There is a limited number of CH_3OH point sources (32) with IASI-based fluxes available for comparison, making it difficult to derive robust statistics. – Top-down fluxes are significantly larger than EDGAR emissions for isolated industrial point sources – There are smaller discrepancies over urban areas, with IASI-based fluxes even significantly lower than EDGAR emissions over megacities such as Mexico City and Manila. – The discrepancies results from IASI being more sensitive to concentrated industrial fluxes, while the EDGAR emissions of alcohol species are dominated by non-industrial emissions.

4. VALIDATION OF REGIONAL SOURCE INVERSION INVENTORIES

4.1. REGIONAL SOURCE INVERSION FOR METHANE (CH4)

4.1.1. COMPARING TOTAL EMISSIONS PER REGION TO INVENTORIES

Regional-level total methane emissions by sector can be derived from gridded bottom-up emission inventories, such as EDGARv6 [RD.33] and GFEIv2 [RD.32]. Also, as our validation process focuses on the Permian basin (US shale oil and gas basin), [RD.30] provide a total emissions estimate based on a TROPOMI inversion to compare with. This inversion is based on observations from May 2018 to March 2019, from which a yearly figure has been derived. Our TROPOMI-based inversion produces yearly estimate from 2019 to 2021. As EDGARv6 accounts for year 2018, GFEIv2 for year 2019, and [RD.30] is based on years 2018 and 2019, these figures should be compared to our 2019 estimates, so that we avoid comparing pre-covid with covid-influenced emissions. Covid lockdowns disrupted the full oil and gas supply chain, and it is very likely that it had a great impact on oil and gas related methane emissions in the Permian basin. On the contrary, TROPOMI-based inversions for 2019 can be compared to gridded inventories for 2018 and 2019, as there has not been any major changes in oil and gas activities in the Permian basin between these two years.

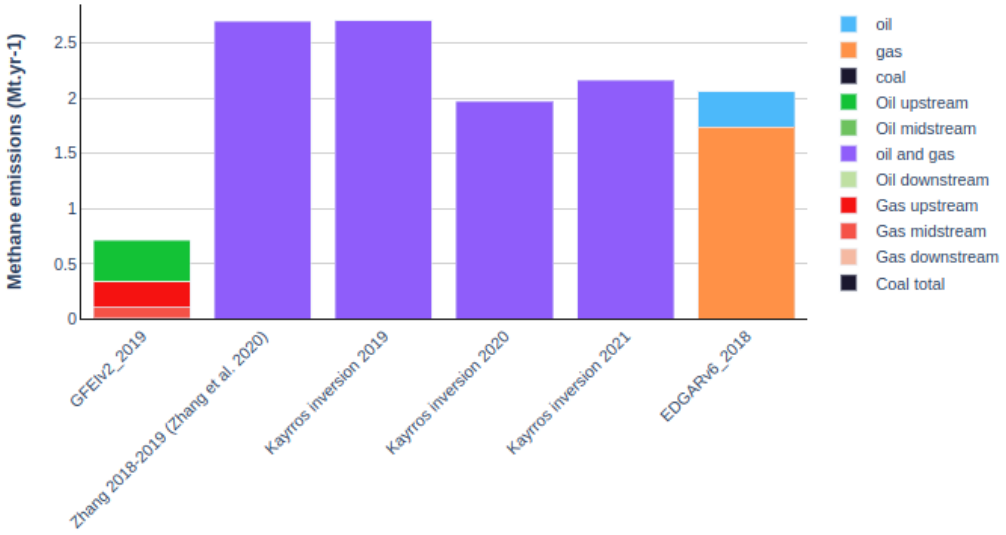

Figure 4-1 Comparison of bottom-up and top-down inventories in the Permian basin

Our inversion for 2019 is very consistent with [RD.30] (<1% relative difference).

TROPOMI-based inversions have a relative difference of 24% with respect to the EDGARv6 estimate for 2018. For GFEI v2, the difference between spaceborne inversions and the bottom-up approach varies by a factor of 4. The differences between top-down and bottom-up approaches do not invalidate our measures but highlight possible methodology issues in the bottom-up stocktakes as significant differences between inversions and reported inventories (with factors above 2) are frequent in the scientific literature [RD.30].

4.1.2. COMPARING REGIONAL EMISSION FACTOR WITH COUNTRY-LEVEL EMISSION FACTORS

Basin-level inventories are not common. It is possible to extract basin data from gridded and sectorized bottom-up inventories. Yet, country-level inventories are more common and remain interesting data points for comparison. To obtain comparable measures, we compare country-wide emission factors (total emissions divided by the number of barrels of oil equivalent produced). Also, to avoid spurious comparisons, as the methane emissions measured in the Permian basin are related to

the upstream oil and gas activities (production), we compute country-level emission factor taking into account upstream emissions only. The US EPA [RD.31] and GFEI v2 [RD.32] provide an inventory for upstream methane emissions. We compute all emission factors by using oil and gas production figures provided by the IEA. Figure 4-2 depicts this comparison.

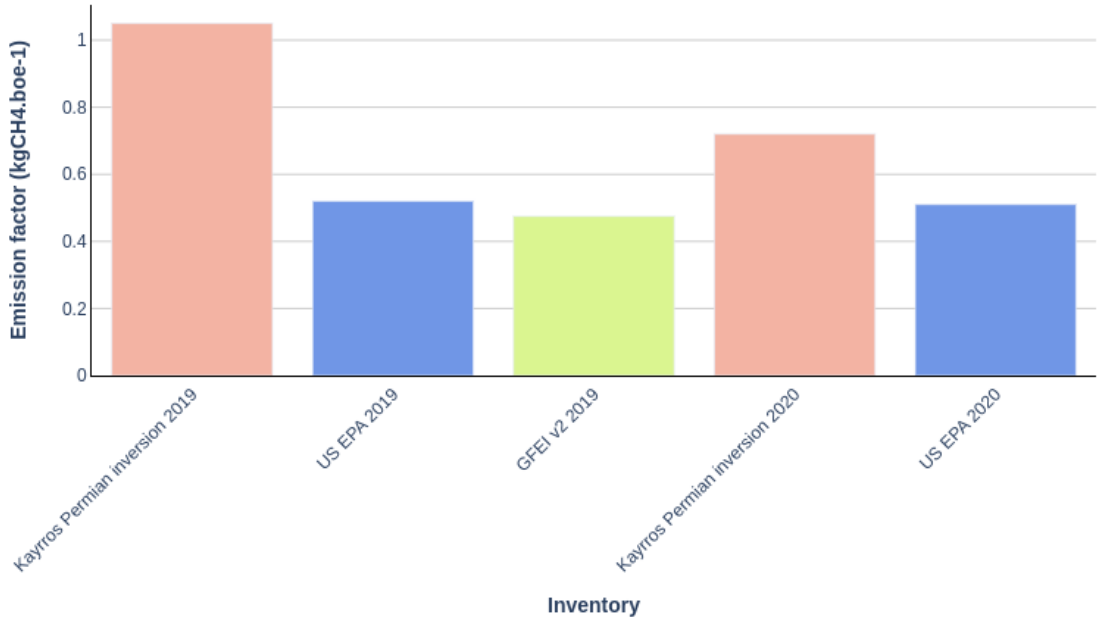

Figure 4-2 Comparison of emission factors derived from country-level inventories and basin-level inversions.

We find a multiplicative factor of 2 for between the emission factors of the US EPA or GFEI v2 and our inventory for the Permian basin in 2019, and a factor of approximately 1.5 for 2020. This is significant but in line with similar research studies [RD.30]. Bottom-up inventories themselves show significant discrepancies (e.g., EDGARv6 and GFEIv2 in Figure 4-1) and are not sufficient comparison points to conclude regarding the validity of our space-borne inversion inventory.

4.1.3. CORRELATION OF RETRIEVED GRIDDED FLUX RATES WITH BOTTOM-UP INVENTORIES

Previous paragraphs show that comparing absolute flux rates does not constitute a reliable validation as significant gaps between remote-sensing based inversions and bottom-up inventories are frequent in the scientific literature.

Our penalized regression-based inversion is, by construction, poorly spatially constrained. If successful, we expect a strong correlation spatial correlation between our posterior estimates and bottom-up gridded inventories. Indeed, although bottom-up inventories like EDGARv6 are based on an inventory of ground infrastructure to which an emission factor is applied. Although top-down inversion challenges the emission factors used in bottom-up inventories, the mapping of the infrastructure should still show a large correlation with the actual emissions.

For this comparison, we use EDGARv6 for year 2018, which we compare to our posterior for year 2019. Comparing to years 2020 or 2021 would be pointless due to the large influence of the covid crisis on methane emissions in the Permian basin. Our inversion produces gridded flux rates on a regular latitude-longitude grid with a resolution of about 0.091 degrees, whereas EDGARv6 provides gridded flux rates with a regular 0.1 degrees step. To avoid reprojection artifacts due to the interpolation when reprojecting our grid on the EDGAR grid, we reproject both inventories on a coarser, 0.2*0.2 degrees grid.

Figure 4-3 shows both gridded inventories, in metric tons per hour emitted in each grid cell. Our inversion lacks spatial constraint to clearly identify emission hotspots, but still clearly identify shale oil and gas sub-basins, namely the Delaware and the Midland basin, are clearly visible as methane emission hotspots. Although the absence of emission prior is a strength to provide inversions in areas

where bottom-up inversions are not reliable or not up-to-date, this figure show that pixel-level emission rate should be rather spatially aggregated to provide region-level figures.

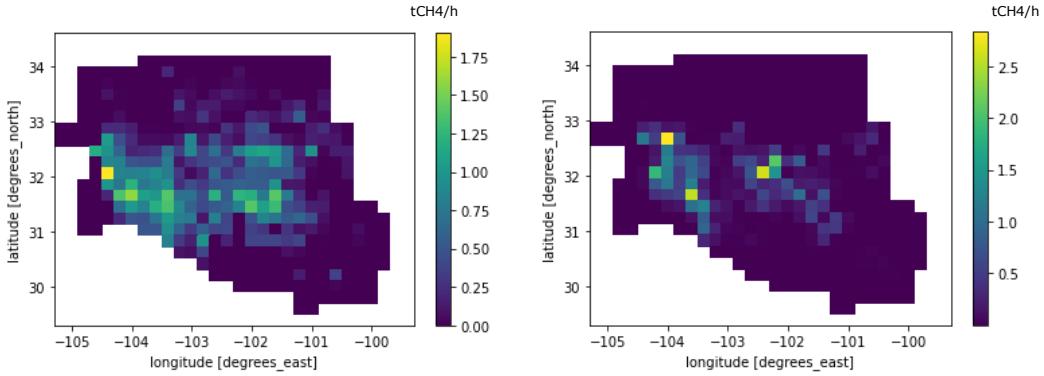

Figure 4-3 Comparison of our inversion posterior (left) with EDGARv6 oil and gas methane emissions (right)

Figure 4-4 shows a scatter plot of a pixelwise comparison of our posterior with EDGARv6. The correlation is 0.48. Although this correlation is weak, this is a strong and satisfying result as we do not use prior emission rates and do not penalize the difference between bottom-up inventories and inversions.

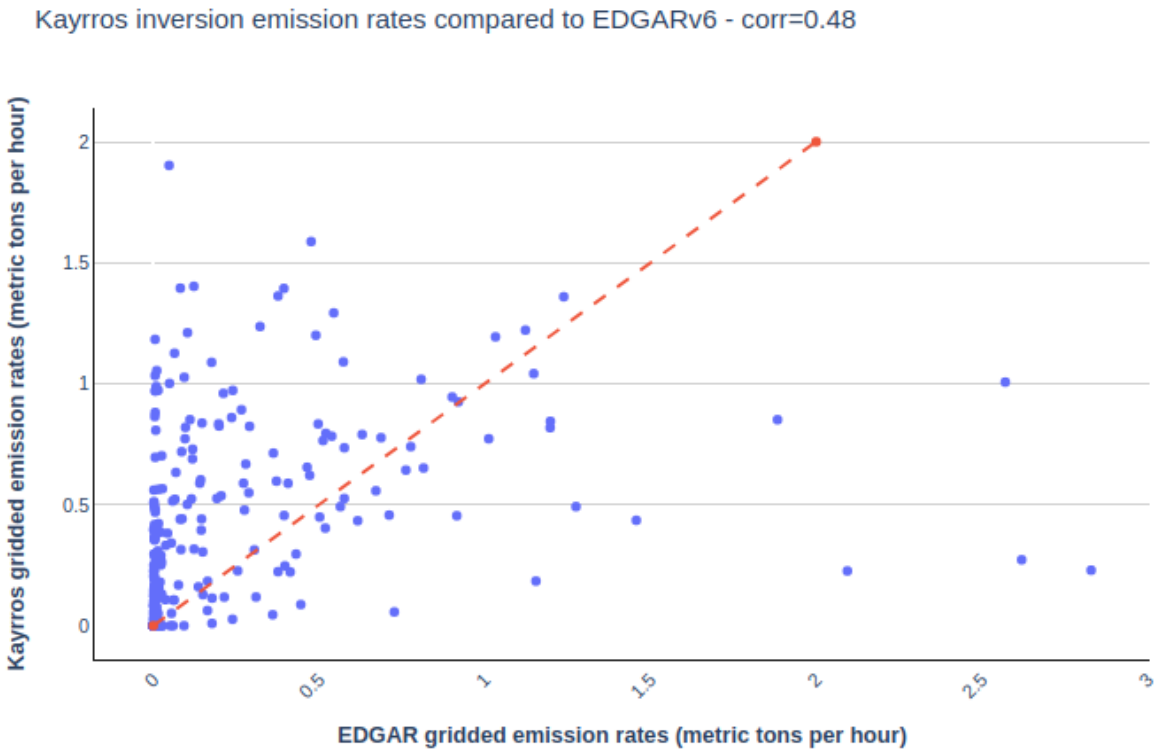

Figure 4-4 Scatter plot comparison of grid cell emission rates for EDGARv6 and our inventory

Although have no spatial constraint *by design*, our inversion results manages to identify the two main methane emission hotspots in the Permian basin, corresponding to the two main sub-basins, the Delaware and Midland shale plays.

4.1.4. SUMMARY

Table 4-1 Inter-comparison assessment table: CH_4- regional

CH_4- regional	
Specie	CH_4
Target level region	Regional (basin-scale)
Target geographic region	Permian oil and gas basin, USA
Type of Validation	Qualitative and quantitative
Parameter(s) to be validated / Test objective	Gridded flux rate, total basins emissions
Validation description/Method	The validation will consist in comparing (bias, standard deviation) the retrieved gridded flux rates with gridded inventories (EDGAR v6.0). Total basin emissions will also be compared with emission inventories (IEA, US EPA) and alternative inversions [RD.30]. Regional emission intensities will also be compared to national inventories.
Validation data	EDGAR v6.0, US EPA, Zhang et al. 2020, IEA. GFEI
Time period	2018 for EDGAR, US EPA and Zhang et al., 2020 and 2021 for IEA
Extrapolation to other regions	Yes, the very same method can be extrapolated to other fossil fuel production basins.
Comments	Top-down regional estimates are expected to be higher than bottom-up inventories, therefore validation will be used for comparisons rather than ground truth.
Results	Overall, our inversion for 2019 is very consistent with [RD.30] (<1% relative difference). TROPOMI-based inversions have a relative difference of 24% with respect to the EDGARv6 estimate for 2018. For GFEI v2, the difference between space-borne inversions and the bottom-up approach varies by a factor of 4. The differences between top-down and bottom-up approaches does not invalidate our measures as significant differences between inversions and reported inventories (with factors above 2) are frequent in the scientific literature [RD.30]. Country-level emission factor for upstream oil and gas activities derived from the US EPA and GFEI inventories can be compared to inversion-based emission factors. Similarly, to the comparison to gridded inventories, multiplying factors from 1.5 to 2 can be found between bottom-up and top-down emission factors, which is consistent with results from [RD.30]. Wide discrepancies are also found between bottom-up inventories themselves (for example EDGARv6 and GFEI in the 2 previous figures). Although interesting to pinpoint the wide difference between bottom-up and top-down inventories, these metrics are not sufficient to validate our inversion-based inventories. We then analysed the correlation between our inventories and bottom-up approaches (namely EDGARv6). In spite of the lack of spatial constraint in our model, we find a satisfying correlation of 0.48 and a visual confirmation that both the Midland and the Delaware methane emission hotspots have been well identified by the model.

4.2. REGIONAL SOURCE INVERSION FOR AMMONIA (NH3)

4.2.1.COMPARISON WITH EDGAR V6.1

NH_3 regional emission fluxes have been derived from IASI satellite observations for a selection of coherent emission regions (e.g., Po Valley, Central US) determined by [RD.16]. These regions represent areas with enhanced NH_3 columns, but with no clear, well-defined point sources, and correspond to, e.g., crop fields, biomass burning areas, mixed sources, larger point sources or several neighbouring ones. More details on the regional source emissions of NH_3 can be found in [RD.16].

Satellite-derived emission fluxes based on 2018 IASI/Metop-A and -B data have been confronted to EDGAR v6.1 bottom-up emission inventory for the same year. Considering the uncertainties associated with such bottom-up inventories for NH_3, this task should be considered as an inter-comparison. The figure below shows that most of the emission fluxes derived are consistent with the EDGAR inventory. Reported top-down emission fluxes are overall higher, which could be partly due to the estimated atmospheric lifetime of 12h used for the calculation of the IASI fluxes. Other lifetimes have been considered and resulting flux estimates are shown as error bars in the figure below. Note that some regions are affected by NH_3 emissions from biomass burning, including the Great Salve Lake (Canada), Central-Yaounde (Cameroon), Central African Republic, Western Africa. NH_3 emissions from fires, however, are not included in EDGAR, and it is therefore not surprising that these regions are the ones for which the largest differences are found.

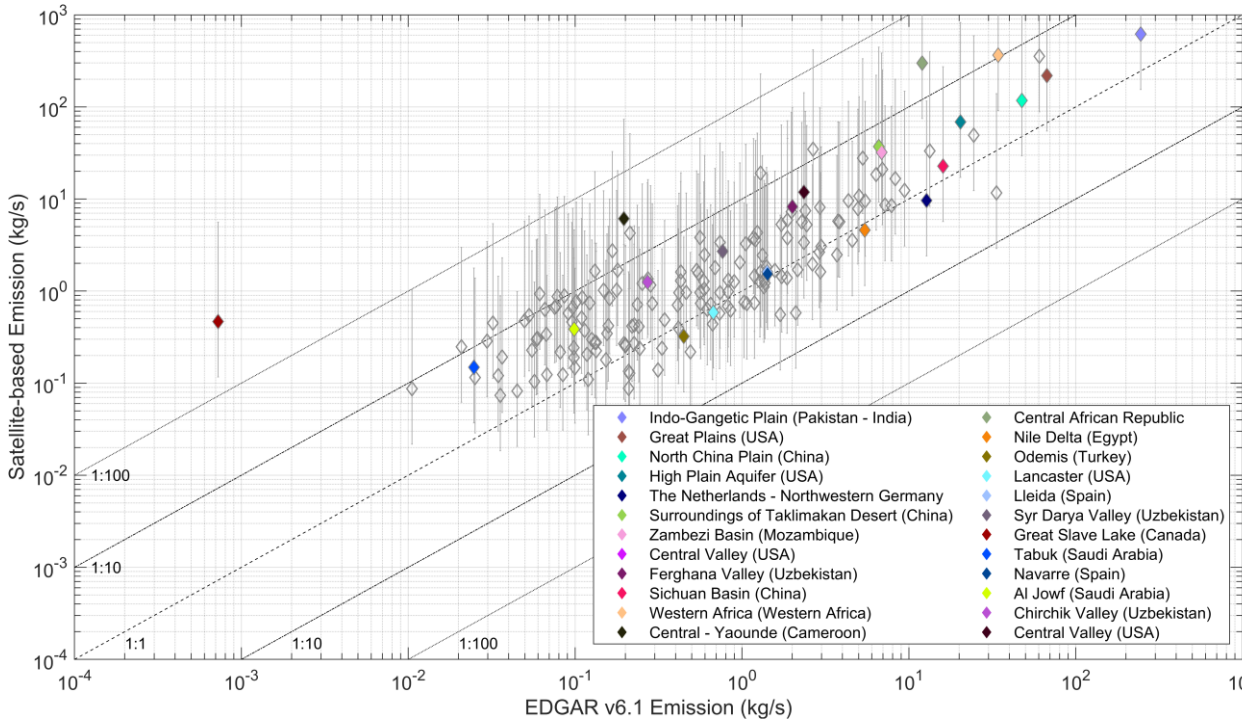

Figure 4-5 Satellite-based emission estimates (in kg/s) for a selection of regions compared with the EDGAR v6.1 emission inventory. The dashed, dash-dotted and dotted black lines represent ratios of EDGAR emission to satellite-based emission of 1:1, 1:10 or 10:1, and 1:100 or 100:1, respectively. The coloured symbols are for selected source areas. Fluxes are calculated assuming a baseline NH3 atmospheric lifetime of 12 h; the error bars correspond to upper- and lower-bound flux estimates based on a lifetime of 1 h and 48 h, respectively.

Regions affected by fires can be filtered out based on the MODIS fire detection product [RD.48]. Putting a threshold of 1×10^{-3} fires per square kilometre in 2018, we excluded 15 regions. From the remaining regions, 58% of the EDGAR emission fluxes agree within a factor two with the top-down estimates derived from IASI. 93% agree within a factor 10.

4.2.2. SUMMARY

Table 4-2 Inter-comparison assessment table: NH_3 - regional

NH_3 – regional	
Specie	NH3
Target level region	Regional
Target geographic region	Selected regions spread over the globe
Type of Validation	Qualitative and Quantitative

NH_3 – regional	
Parameter(s) to be validated / Test objective	Regional emission estimates (annual mean)
Validation description/Method	Numerical statistics will include parameters such as bias and standard deviation.
Validation data	Global bottom-up inventories (EDGAR v6.1)
Time period	Selected years depending on the availability of the bottom-up inventories
Extrapolation to other regions	No
Comments	Considering the uncertainties associated with such bottom-up inventories for NH3, this task should be considered as an inter-comparison.
Results	Comparison between bottom-up EDGAR v6.1 and top-down IASI-derived NH3 emission fluxes for a selection of consistent source regions show a good consistency. Future work could be dedicated to assessing biomass burning emission against fire inventories

4.3. REGIONAL SOURCE EMISSIONS FROM INVERSION MODELS FOR CARBON DIOXIDE (CO_2), NITROGEN OXIDES (NO_X), AND CARBON MONOXIDE (CO)

In the frame of the first phase of the project, the regional NO_x, CO and CO_2 emission estimates have been derived for Europe only. These inversions for Europe have been updated during the second phase: the following documents results from this update. Estimates for Eastern China are about to be provided in the course of the second phase of the project. The sequence of computations for the estimate of the regional NO_x, CO and CO_2 emissions in Europe follows the approach by [RD.34] and consists in:

1) the atmospheric inversions of maps of the NO_x or CO emissions during 2019-2022 at 1-day and 0.5° resolution. These inversions are based on the coupling between the variational mode of the Community Inversion Framework (CIF, [RD.18]), the CHIMERE regional atmospheric chemistry transport model ([RD.22]) and the adjoint code of this model ([RD.20]). This CIF-CHIMERE regional mesoscale variational inversion framework is close to the system described by [RD.20]. The current NO_x and CO inversions assimilate respectively atmospheric NO_2 and CO products from spaceborne instruments: NO_2 satellite data from OMI ([RD.21]) and TROPOMI ([RD.35]) and CO data from MOPITT ([RD.19]). Future inversions should also assimilate CO data from TROPOMI. They apply 0.5°/1-day resolution corrections to the maps of anthropogenic emissions from a gridded product coupling the Carbon Monitor and the CEDS inventories of the NO_x, CO and CO_2 emissions and to the maps of biogenic emissions of NO_x from the MEGAN global model ([RD.36]) to better fit these assimilated observations. This calculation is performed by LSCE in collaboration with LISA, a partner laboratory of the IPSL.

2) for each country in Europe: the conversion of the monthly maps of NO_x or CO anthropogenic emissions from these inversions into monthly maps at 0.5° resolution and national scale estimates of the fossil fuel CO_2 emissions for five large groups of sectors of emitting activities. This conversion relies on the sectoral maps of emissions from the three species and, implicitly, on the emission ratios between the species for each sector, country and month from the Carbon Monitor - CEDS inventory.

The CO_2 regional product is thus derived from the NO_x and CO regional emission inversions. At this stage, the validation is mainly focused on that of the NO_x and CO regional inversions.

4.3.1. QUALITY CONTROL WITH THE INTERNAL DIAGNOSTICS OF THE INVERSIONS

Traditional internal diagnostics of the variational inversions are used to evaluate the atmospheric inversions of the maps of NO_x and CO emissions. In particular, the norm of the gradient of the cost function J, whose minimum is searched for with the iterative limited-memory quasi-Newton minimization algorithm M1QN3 algorithm [RD.37], and which is used by the inversions to find the optimal emission maps, is reduced by more than 95% in all cases.

The level of reduction of the misfits to the assimilated data by the inversion (compared to the misfits obtained when using the prior estimate of the emissions given by the Carbon Monitor - CEDS inventory) was relatively satisfying for the CO inversions in Phase I, as the use of CO emissions from the inversions strongly improved the CO simulations compared to the use of the emissions from the Carbon Monitor - CEDS inventory.

For NO_2, the use of the NO_x emissions from the inversions raised concerns and revealed the need for further analysis in Phase II, particularly for the comparison of the modelled NO_2 concentrations to the TROPOMI-PAL observations over highly polluted areas, since these misfits often increased for individual aggregates of the observations at 0.5° resolution, and even over larger spatial scales. The new configuration of the NO_x inversions (see D3_v3) now allows a better reduction of the misfits to the assimilated NO_2 data by the inversion over polluted areas (compared to the misfits obtained when using the prior estimate of the emissions given by the Carbon Monitor - CEDS inventory, Figure 4-6).

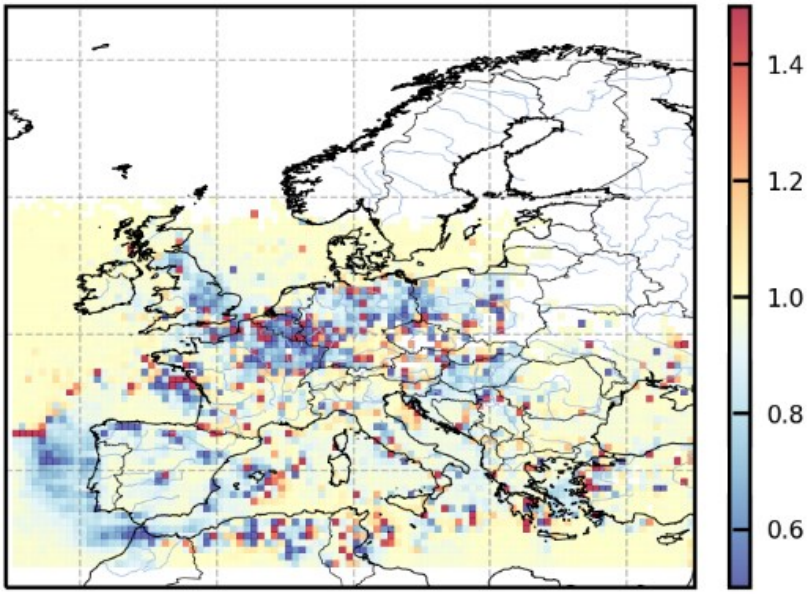

Figure 4-6 Relative change (ratio between the values from the inversion and from the simulations with the Carbon Monitor - CEDS inventory) of the biases between NO_2 monthly mean tropospheric columns from CHIMERE and the TROPOMI observations (aggregated at 0.5° resolution) due to the NO_x emission inversion, in January 2019. All ratios lower than 1, in blue, indicate improvements due to the use of emission estimates from the inversion compared to the use of emission estimates from the Carbon Monitor- CEDS.

There is currently no estimate of the uncertainties in the NO_x and CO emission maps from these inversions. Such uncertainties emerge from the combination of the uncertainties in the atmospheric chemistry-transport modelling, in the satellite NO_2 and CO products and in the prior estimate of the emissions. While different techniques (e.g., Monte Carlo ensemble techniques) allow, in theory, to derive estimates of these uncertainties for variational inversions, the corresponding computational cost is large and raises challenges.

4.3.2. QUALITY CONTROL THROUGH COMPARISONS TO INDEPENDENT INVENTORIES

The monthly NO_x and CO emissions estimates for the European Union + United Kingdom (EU-27+UK) area are compared to the values given by the most recent TNO inventory (the TNO-GHGco-v3 inventory) for the year 2019. This inventory is relatively independent from the Carbon Monitor - CEDS inventory used here as prior estimate by the inversions. This comparison will be extended to the CO_2 emission estimates. The NO_x emission estimates are also compared to the CAMS-REG COVID-19 emission inventory dataset for 2020. At finer scale, the NO_x and CO estimates are compared to the Catalonia HERMESv3 inventory for 2019 by BSC (to which the inversion results have been transferred). Finally, the NO_x and CO_2 emission estimates are compared to the Cyprus inventory at fine scale over 2019-2021 by the Cyprus Institute (to which the inversion results have also been transferred).

Figure 4-7 shows that the TNO inventory presents a seasonal cycle of the CO emissions in the European Union + United Kingdom (EU-27+UK) area in 2019 similar to that of the Carbon Monitor - CEDS inventory and to that of the CO emission estimates from the inversion. The annual budgets of CO emissions from TNO and from the inversions are consistent over the EU-27+UK area and in 2019, TNO providing a higher value by about 3.4%.

Figure 4-7 shows that the TNO inventory gives larger NOx emission estimates than the Carbon Monitor - CEDS inventory for the EU27+UK area. The inversion estimates of the NO_x emissions using the TROPOMI observations correspond to strong corrections to the Carbon Monitor - CEDS inventory . The inversion therefore brings the emission estimates closer to the TNO inventory.

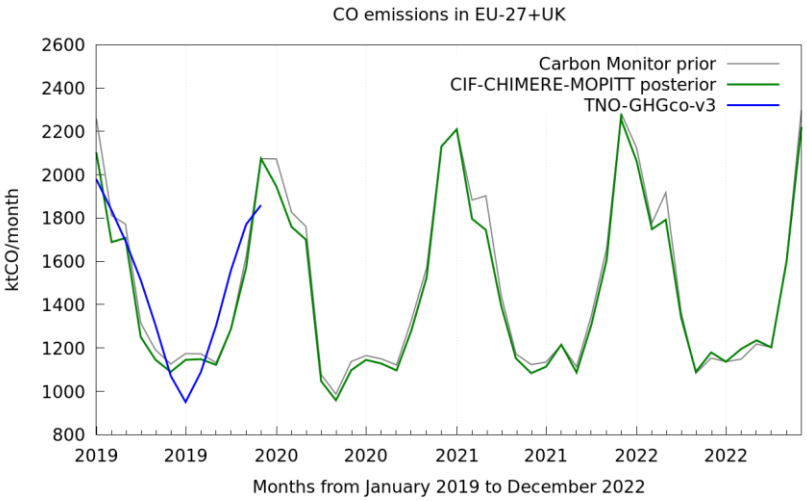

Figure 4-7 Estimates of the monthly budgets of CO emissions from 2019 to 2022 for the EU27+UK area from the Carbon Monitor - CEDS inventory (in grey), from the regional inversions assimilating MOPITT CO surface observations (in green) and from the TNO-GHGco-v3 inventory for 2019 (in blue), in ktCO/month.

Figure 4-8 Estimates of the monthly budgets of NO_x anthropogenic emissions from 2019 to 2022 for the EU27+UK area from the Carbon Monitor - CEDS inventory (in grey) from the regional inversions assimilating TROPOMI-PAL observations (in green), and from the TNO-GHGco-v3 inventory for 2019(in blue), in $ktNO_2$/month.

The monthly NOx emission estimated for the European Union + United Kingdom (EU-27+UK) area for the year 2020 were compared to the bottom-up CAMS-REG COVID-19 emission inventory dataset, which provides daily estimates of anthropogenic emissions for Europe for 2020 including the impact of the COVID-19 restrictions [RD.45]. The comparison focusses on the relative monthly cycles reported by

each dataset at the EU-27 + UK level and for individual countries. The aim is to compare the COVID-19 effect on the monthly distribution of NOx emissions as seen by satellite-based and bottom-up estimates.

Figure 4-9 Estimates of monthly cycles of NOx anthropogenic emissions for 2020 for EU27+UK and individual countries from the CAMS-REG inventory (in red) and the regional inversions assimilating TROPOMI-PAL observations (in blue). Values represent monthly weight factors (sum up to 12).Figure 4-9 shows that the CAMS-REG and the inversion estimates consistently report important drops in NOx emissions during April 2020, coinciding with the implementation of lockdowns and mobility restrictions. The drops are larger in countries where restrictions were stronger, such as Spain, Italy or France, while in countries where the restrictions were softer (e.g., Sweden, Finland or Hungary) both the CAMS-REG and inversion monthly cycles tend to be flatter. The CAMS-REG estimates tend to report slightly larger drops of NOx emissions during April. A high correlation is observed between the bottom-up and top-down monthly cycles (0.8 at the EU27+UK level), especially in the countries that were most affected by the COVID-19 infections (0.93 for Spain, 0.87 for Italy and 0.91 for Italy) Oppositely, the inversion estimates tend to show larger drops of NOx during October, when the second wave of COVID-19 spread occurred. Actually, the drops reported by the inversion estimates for October tend to be larger than the ones estimated for April.

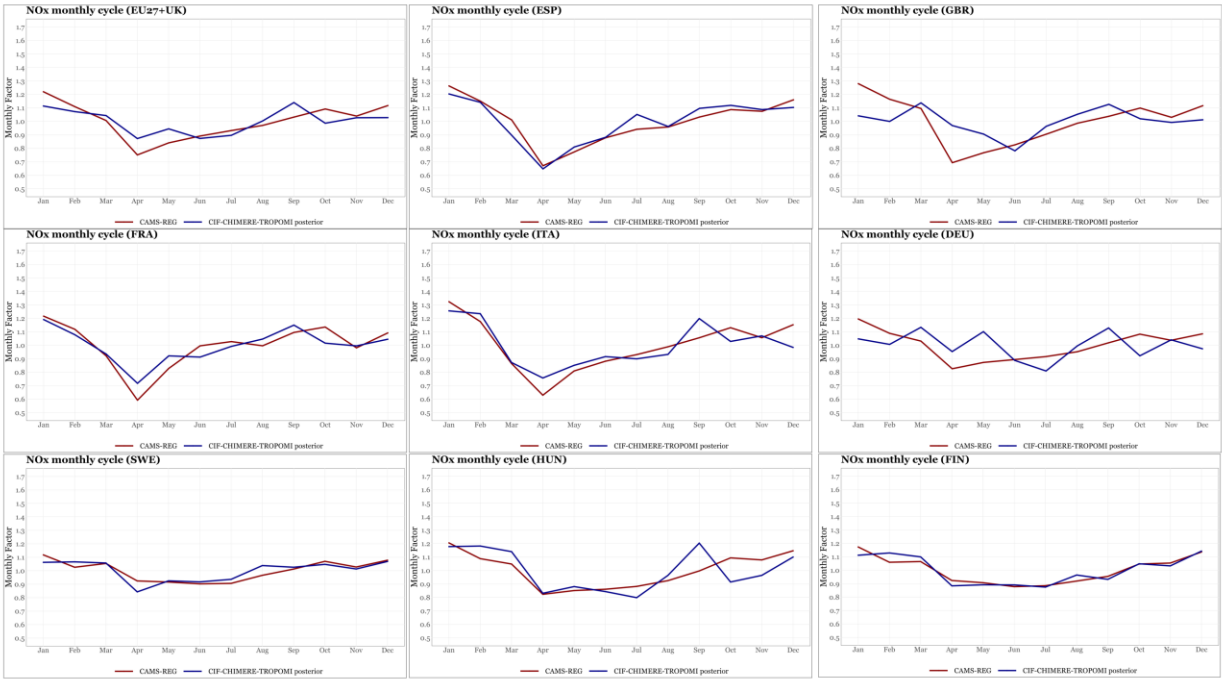

Figure 4-9 Estimates of monthly cycles of NO_x anthropogenic emissions for 2020 for EU27+UK and individual countries from the CAMS-REG inventory (in red) and the regional inversions assimilating TROPOMI-PAL observations (in blue). Values represent monthly weight factors (sum up to 12).

The monthly estimates of NO_x and CO anthropogenic emissions for the region of Catalonia (Spain) and the year 2019 were compared against the bottom-up inventory produced by the High-Elective Resolution Modelling Emission System (HERMESv3; [RD.43]).

Figure 4-10 and Figure 4-11 show the results of the intercomparison for NOx and CO, respectively. For both species HERMESv3 estimates are fairly in line with the inversion results. Overall, for NO_x HERMESv3 (80 kt NO_x/year) reports -12% less emissions than the satellite-based inventory (91 kt NO_x/year). The total annual NO_x estimates reported by HERMESv3 are closer to the estimates provided by the official Spanish emission inventory for the same region (70 kt NO_x/year; MITERD, 2023). Discrepancies between results mainly occur during the beginning and end of the year, while for the rest of the months results are very much in line. Concerning the monthly distribution of NO_x emissions, a large discrepancy exists between the seasonalities reported by each dataset. Of note is that the comparisons at European and national scales to CAMS-REG in 2020 and at regional scale to HERMESv3 in 2019 seem to highlight, together, a tendency of the inversions to overestimate of the NOx emissions in September. There is, however, no reason to assume that the inversions could be biased by a specific chemistry-transport modeling bias or by specific biases in the TROPOMI NO2 observations during this specific month every

year. Oppositely, the CO seasonalities reported by HERMES and the inversion results are very in line (r = 0.86), with maximum values occurring during winter-time, and minimum emissions reported during summer. As shown for NO_x, CO emissions reported by HERMES v3 are slightly lower than the inversion estimates assimilating MOPITT observations (-23%).

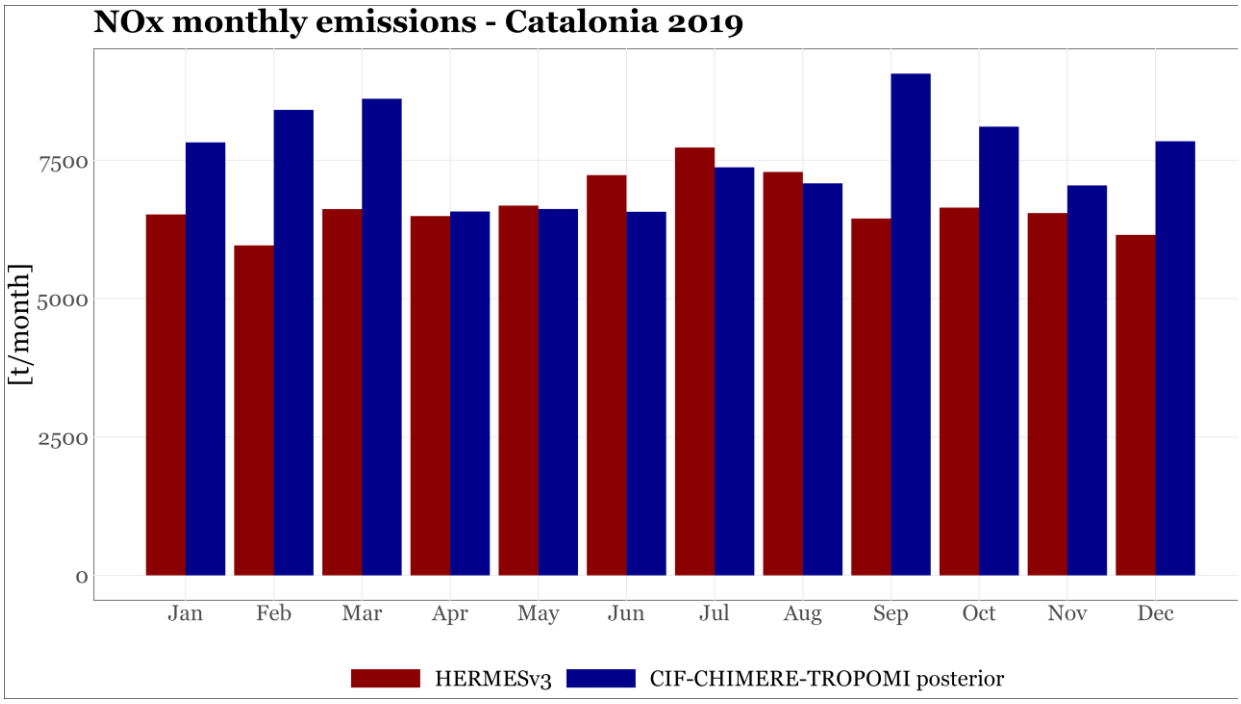

Figure 4-10 Estimates of monthly NOx anthropogenic emissions [t/month] for 2019 for Catalonia (Spain) from the HERMESv3 bottom-up inventory (in red) and the regional inversions assimilating TROPOMI-PAL observations (in blue).

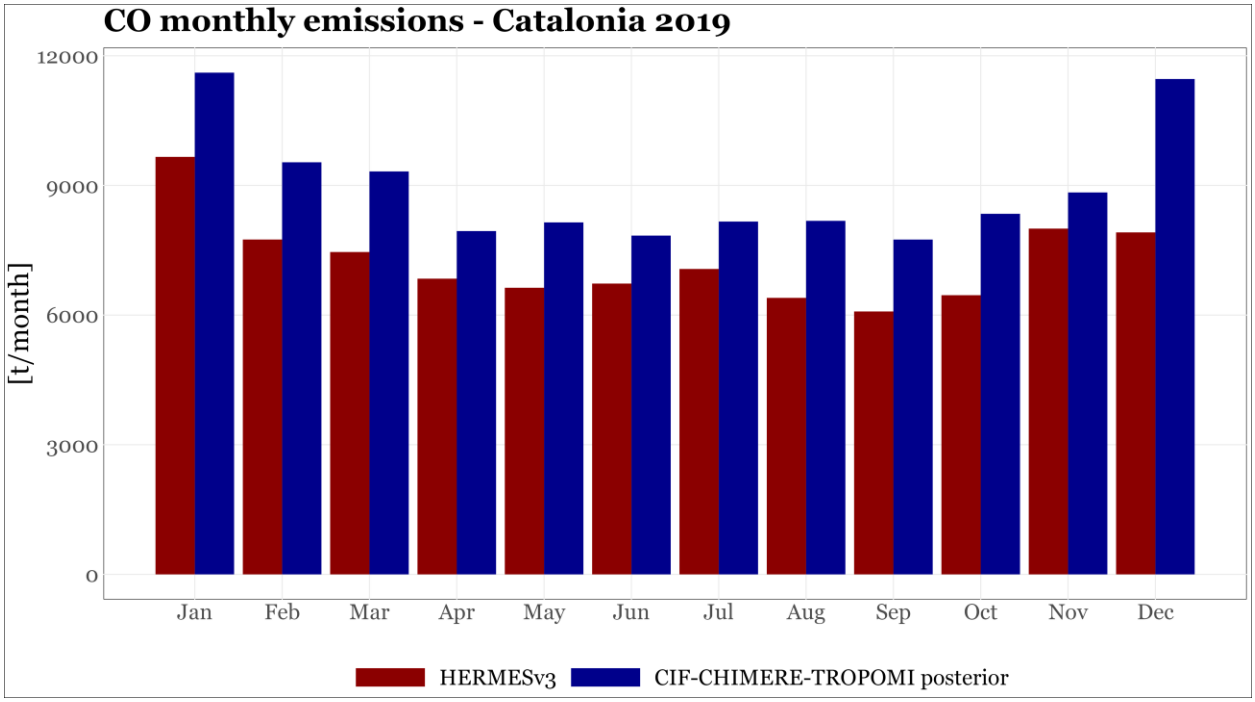

Figure 4-11 Estimates of monthly CO anthropogenic emissions [t/month] for 2019 for Catalonia (Spain) from the HERMESv3 bottom-up inventory (in red) and the regional inversions assimilating TROPOMI-PAL observations (in blue).

An intercomparison exercise for NO_x and CO_2 has also been performed over Cyprus for the latest version of the regional inversions, i.e., comparing the 4-year NO_x and CO_2 regional inversion product used and shared during the Phase II of World Emission and the emissions reported officially by Cyprus in the National Inventory Report (NIR 2023) and the Informative Inventory Report (IIR 2023). The time series 2019-2022 data has been compared for the CO_2 and NOx total emissions as well as by sector.

Discrepancies were found between the total reported emissions from the National Inventory and project CO_2 emissions for the whole timeseries 2019-2022, with the project emissions being significantly lower than the nationally reported emissions (NIR).

Figure 4-11 (top plot) shows the comparison between the total reported CO2 emissions (including LULUCF, i.e. ~-300ktCO2 per year) VS the projects emissions (which do not include LULUCF, but it is not significant compared to the differences between the two types of estimates) for the time series 2019-2022. The exact values of emissions are presented in Table 4-3. Per sector comparison is further provided in table 2 for the year 2020.

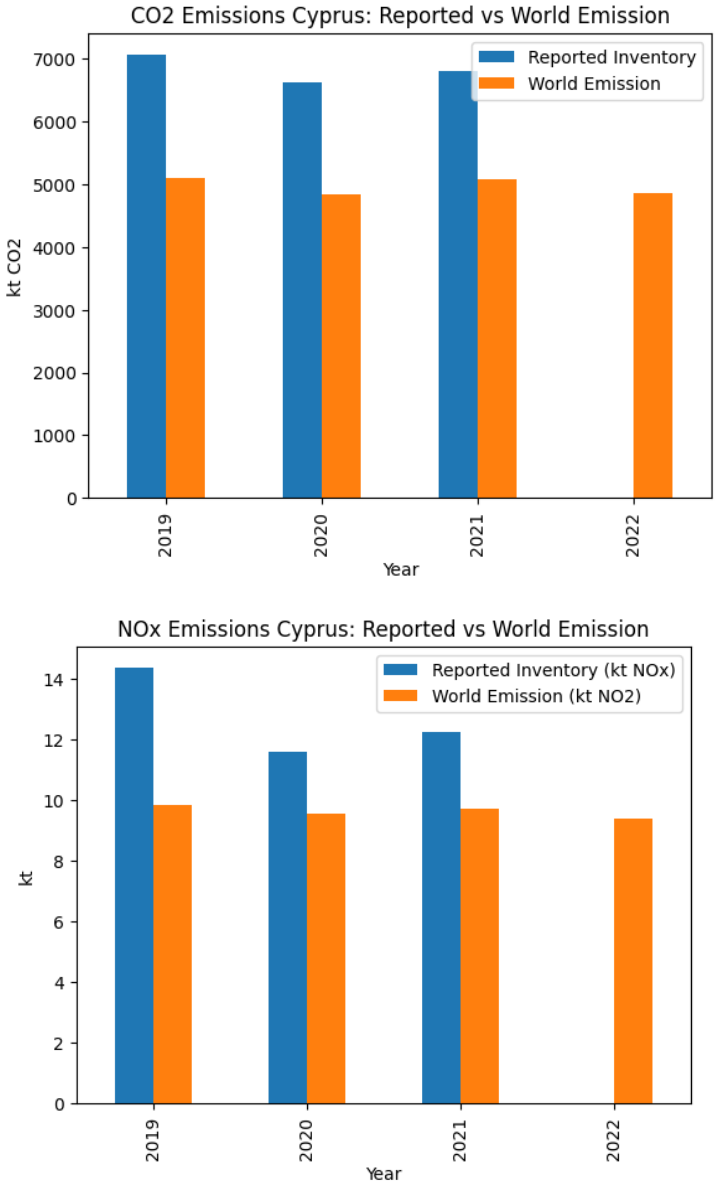

Figure 4-11 Total reported a) CO2 (top) and b) NOx (bottom plot) emissions for Cyprus (blue bars) versus estimates from the regional inversions assimilating TROPOMI-PAL observations (orange bars)

The same analysis has been carried out for the NO_x emissions comparing the reported emissions (IIR 2023) with the inversion estimates and more specifically with the World Emission project gridded information from these inversions. Here, the NOx emissions reported in the gridded regional inversions data are lower than the national inventory ones. The annual national totals from the reported inventory and platform estimates are depicted in Figure 4-11 (bottom plot).

Table 4-3 Total annual CO2 emissions at country level (Cyprus) from national inventory and project estimates

Year	Reported Inventories		World Emission-grids	
	(kt CO2)	(kt NOx)	(kt CO2)	(kt NO2)
2019	7,043.58	14.34	5,094.60	9.84
2020	6,610.54	11.59	4,824.24	9.55
2021	6,784.63	12.25	5,072.95	9.71
2022			4,861.55	9.40

Table 4-4 CO2 and NOx emissions by sector (NIR, World Emission)

Species (Year)	Source	Units	ENERGY	INDUSTRY	RESIDENTIAL	ROAD TRANSPORT	OTHER	TOTAL
CO_2 (2020)	**World Emission**	kt CO2	1,633.10	1,149.23	431.45	1,558.24	52.21	4,824.24
	Reported	kt CO2	3,023.11	1,461.16	197.64	1,901.92	26.71	6,610.54
NOx (2020)	**World Emission**	kt NO2	1.64	2.25	0.64	4.20	0.83	9.55
	Reported	kt NOx	2.92	1.80	0.57	4.40	1.88	11.59

4.3.3. SUMMARY

Table 4-5 Inter-comparison assessment table: CO_2- regional

CO_2 - regional	
Specie	CO_2
Target level region	Regional
Target geographic region	Wallonia, Catalonia, Ile de France, Ruhr region, Cyprus, European countries (EU-27+UK), Eastern China
Type of Validation	Qualitative and quantitative comparison
Parameter(s) to be validated / Test objective	Emission budgets at monthly to annual scale **Consistency of thematic information (only for Wallonia, Catalonia, Ile de France, Ruhr region, Cyprus)**
Validation description/Method	Statistics of the misfits between the inversions and the inventories
Validation data	Bottom-up emission inventories: regional inventories for Catalonia (HERMESv3 model) and Cyprus (national inventory, bottom-up approaches for three power plants in Cyprus), and EDGAR-v6.1 over the globe
Time period	2019-2021
Extrapolation to other regions	-

CO_2 - regional	
Comments	The spatial resolution of the regional inversions is 0.5° and some downscaling (e.g., with Carbon Monitor- CEDS) may be needed to attempt at making proper comparisons with regional inventories. More generally, the spatial resolution of the European-scale inversions may not be suitable for comparisons for small European administrative regions. These comparisons are thus challenging and exploratory.
Results	The CO2 regional product is derived from the NOx and CO regional emission inversions. At this stage, the validation is focused on that of the NOx and CO regional inversions. However, a first comparison between the CO2 regional product and the Cyprus national inventory has been conducted.

Table 4-6 Inter-comparison assessment table: NO_x - regional

NO_x – regional	
Specie	NO_x
Target level region	Regional
Target geographic region	Wallonia, Catalonia, Ile de France, Ruhr region, Cyprus, European countries (EU-27+UK), Eastern China
Type of Validation	Qualitative and quantitative comparison
Parameter(s) to be validated / Test objective	Emission budgets at monthly to annual scale **Consistency of thematic information (only for Wallonia, Catalonia, Ile de France, Ruhr region, Cyprus)**
Validation description/Method	Statistics of the misfits between the inversions and the inventories
Validation data	Bottom-up emission inventories: regional inventories for Catalonia (HERMESv3 model) and Cyprus (national inventory, bottom-up approaches for three power plants in Cyprus) and EDGAR-v6.1 and CAMS-REG over Europe
Time period	2019-2021
Extrapolation to other regions	N/A
Comments	The spatial resolution of the regional inversions is 0.5° and some downscaling (e.g., with Carbon Monitor- CEDS) may be needed to attempt at making proper comparisons with regional inventories. More generally, the spatial resolution of the European-scale inversions may not be suitable for comparisons for small European administrative regions. These comparisons are thus challenging and exploratory.
Results	At this stage, the validation consists in (i) checking internal diagnostics (e.g., level of decrease of the cost function) of the NOx regional inversions (ii) comparisons at national and 1-month scale to the most recent TNO inventory of CO2, CO and NOx emissions in 2019 (the TNO-GHGco-v3 inventory) (iii) comparisons at national and 1-month scale to the CAMS-REG COVID-19 inventory in 2020 (by BSC) (iv) comparisons at regional and 1-month scale to the Catalonia HERMESv3 inventory for 2019 (by BSC) (v) comparisons at regional, annual and sectoral scale to the Cyprus national inventory (by the Cyprus institute) The TNO inventory tends to show larger emission estimates than the Carbon Monitor - CEDS inventory. The inversion estimates of the NOx emissions assimilating the TROPOMI-PAL observations apply strong corrections to the Carbon Monitor - CEDS inventory, getting closer to the TNO inventory in 2019. Both the CAMS-REG inventory and inversion estimates consistently report significant drops in NO_x emissions during April 2020, specially in those countries where COVID-19 restrictions were stronger, such as Spain, France or Italy. As a result, a large correlation exists between the bottom-up and top-down monthly emission profiles estimates for 2020. The comparison between the inversion and independent bottom-up estimates using HERMESv3 for the region of Catalonia and the NIR inventory for Cyprus indicates a consistency between results, the satellite-based emissions presenting larger emissions at the beginning and end of the year than HERMESv3 when analysing the monthly estimates in Catalonia, and slightly smaller emissions than the NIR inventory in Cyprus.

Table 4-7 Inter-comparison assessment table: CO - regional

CO – regional	
Specie	CO
Target level region	Regional
Target geographic region	Wallonia, Catalonia, Ile de France, Ruhr region, Cyprus, European countries (EU-27+UK), Eastern China
Type of Validation	Qualitative and quantitative comparison
Parameter(s) to be validated / Test objective	Emission budgets at monthly to annual scale **Consistency of thematic information (only for Wallonia, Catalonia, Ile de France, Ruhr region, Cyprus)**
Validation description/Method	Statistics of the misfits between the inversions and the inventories
Validation data	Bottom-up emission inventories: regional inventories for Catalonia (HERMESv3 model) and Cyprus (national inventory, bottom-up approaches for three power plants in Cyprus) and EDGAR-v6.1 over Europe
Time period	2019-2021
Extrapolation to other regions	N/A
Comments	The spatial resolution of the regional inversions is 0.5° and some downscaling (e.g., with Carbon Monitor) may be needed to attempt at making proper comparisons with regional inventories. More generally, the spatial resolution of the European-scale inversions may not be suitable for comparisons for small European administrative regions. These comparisons are thus challenging and exploratory.
Results	At this stage, the validation consists in (i) checking internal diagnostics (e.g., level of decrease of the cost function) of the CO regional inversions (ii) comparisons at national and 1-month scale to the most recent TNO inventory of CO2, CO and NOx emissions in 2019 (the TNO-GHGco-v3 inventory), (iii) comparisons at regional and 1-month scale to the Catalonia HERMESv3 inventory for 2019 (by BSC). Contacts have been made with the Cyprus Institute for analysis at finer scales with theCyprus NIR inventory. The TNO inventory presents a seasonal cycle of the CO emissions in Europe similar to that of the Carbon Monitor - CEDS inventory used here as a prior estimate by the inversions and to that of the CO emission estimates from the inversion. The annual budgets of CO emissions from TNO and from the inversions are consistent over the EU-27+UK area and in 2019, TNO providing a higher value by about 3.4%. The comparison between the inversion and independent bottom-up estimates using HERMESv3 for the region of Catalonia indicates a consistency between results, both datasets reporting very similar seasonality (r = 0.86) and the bottom-up results being slightly lower (-23%).

5. VALIDATION OF GLOBAL SOURCE INVERSION INVENTORIES

5.1. GLOBAL SOURCE INVERSIONS FOR METHANE (CH4)

We evaluated the global CH4 inversion results using independent aircraft and AirCore vertical profiles and total column measurements of CH4 from TCCON network that were not assimilated in the inversion. The CH4 aircraft vertical profiles were collected from IAGOS vertical profiles as well as data from regular research aircraft profiles mainly operated by NOAA, plus additional data for AOA in the north western pacific and Manaus in Brazil (Figure 5-1) We also used vertical profiles from Aircore systems which are passive samplers of the atmospheric concentration on board of dedicated small balloons going from the boundary layer to the lower stratosphere (20 to max 30 km), periodically launched and recuperated on the ground for CH4 concentration analysis (Figure 5-1).

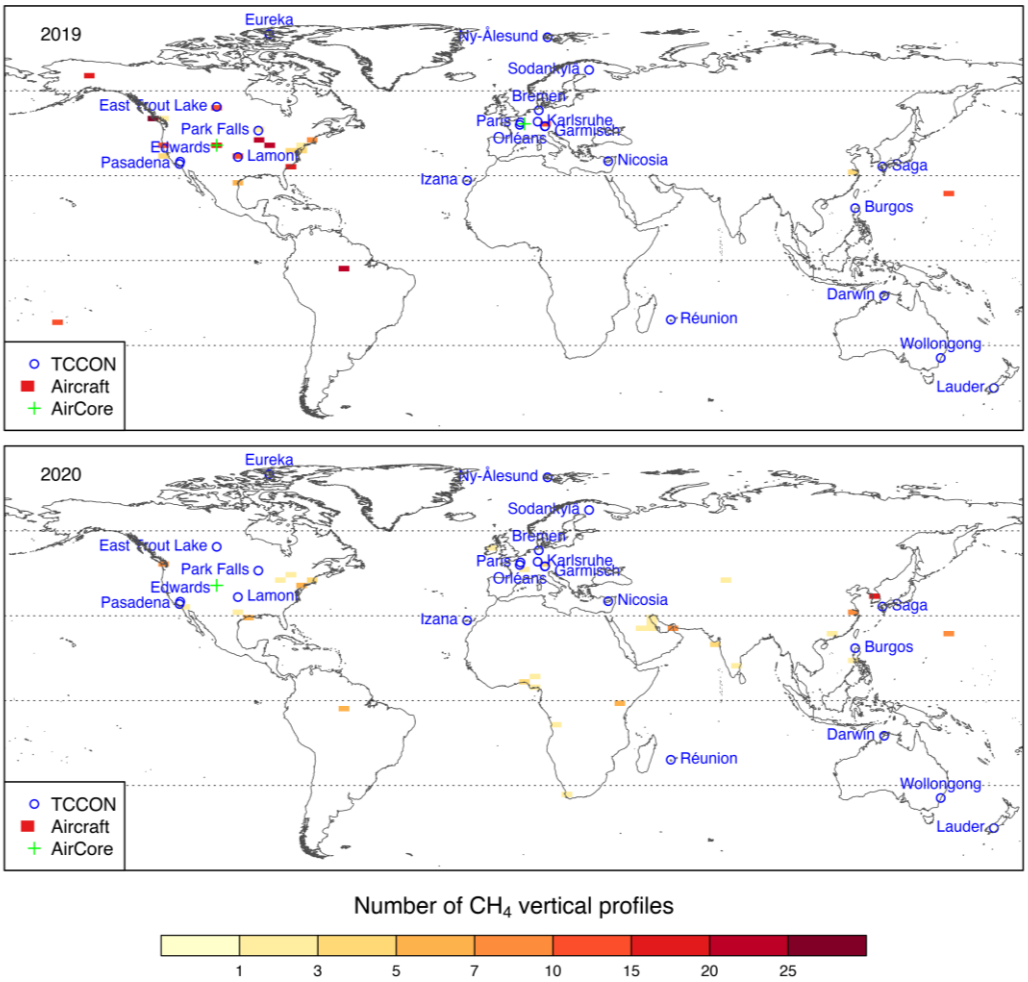

Figure 5-1 Map of sites from multiple observing platforms and networks used for independent evaluation of global CH4 inversion. For the Total Carbon Column Observing Network (TCCON), only sites with data available in the GGG2014 version of the data retrievals for both 2019 and 2020 are presented. The aircraft CH4 vertical profiles are compiled from data products from NOAA's GGGRN, the In-service Aircraft for a Global Observing System and Japan Meteorological Agency and mapped on the model grids of the global inversion system (1.9°x3.75°), coloured by the number of CH4 vertical profiles. The AirCore samplings are obtained from NOAA AirCore campaigns, which are available at Boulder, US and Traînou, France in 2019 and are only available at Boulder, US in 2020.

Figure 5-2 presents the modelled versus observed latitudinal gradients in XCH4 anomalies between 2020 and 2019. The posterior model states broadly capture the overall patterns during January–March (JFM), April–June (AMJ), and July–September (JAS). During October–December (OND), a much better model-observation agreement is found for the posterior model states (red dots) than the prior (blue

dots) in terms of the magnitude of XCH4 anomalies over all latitude bands, even though the posterior XCH4 anomalies are still smaller than the observed ones (black dots) at Lauder in the Southern Hemisphere and the sites in the Northern Hemisphere North of 40°N.

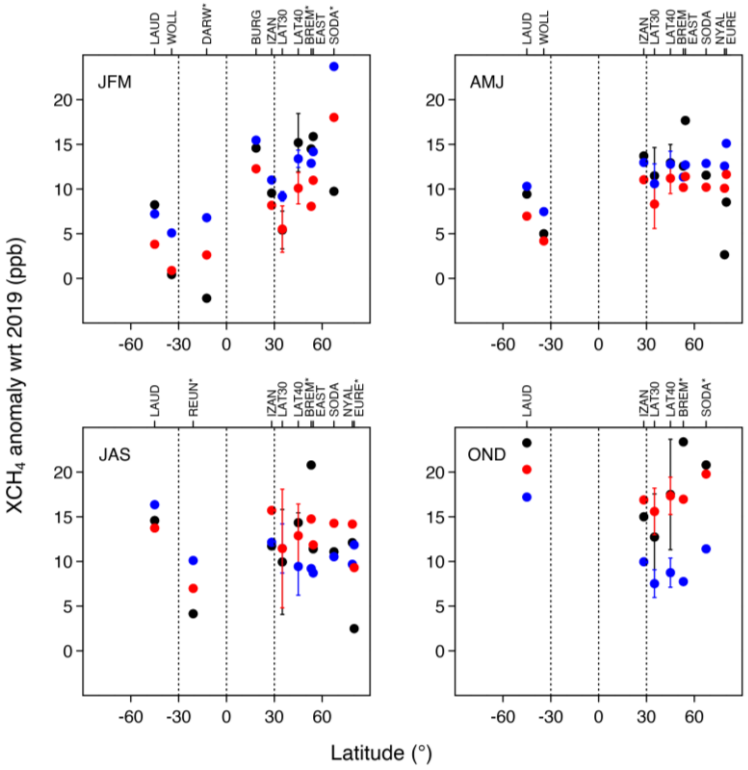

Figure 5-2 The change in XCH4 between 2019 and 2020 for January–March (JFM), April–June (AMJ), July–September (JAS), and October–December (OND) at TCCON sites. Black dots are observations, Blue dots prior and red dots are posterior data. Note that values at sites between 30°N–40°N and 40°N–50°N are averaged (denoted as "LAT30" and "LAT40" respectively) for better visualization. The GGG2014 version of the TCCON retrievals is used for evaluation (site abbreviations: BREM–Bremen; BURG–Burgos; DARW–Darwin; EAST–East Trout Lake; EURE–Eureka; IZAN–Izana; LAUD–Lauder; NYAL–Ny-Alesund; REUN–Réunion Island; SODA–Sodankyla; WOLL–Wollongong; also see Figure 5-1 for site locations).

Regarding the CH4 vertical profiles from aircraft sampling networks and campaigns, Figure 5-3 demonstrates that the posterior model states can capture well the north-south gradients of vertical CH4 differences between 1- and 4 km for all seasons during 2019–2020, reflecting the robustness of the global CH4 inversion in representing large-scale atmospheric mixing (both horizontally and vertically) and separating latitudinal emissions. Note that there are a few cases (e.g., JFM and JAS in 2020) where the vertical CH4 difference is overestimated in the Northern Tropics while underestimated in the neighboring mid-latitude bands, possibly suggesting biases in source allocation between these latitude bands due to sparse data coverage in certain regions.

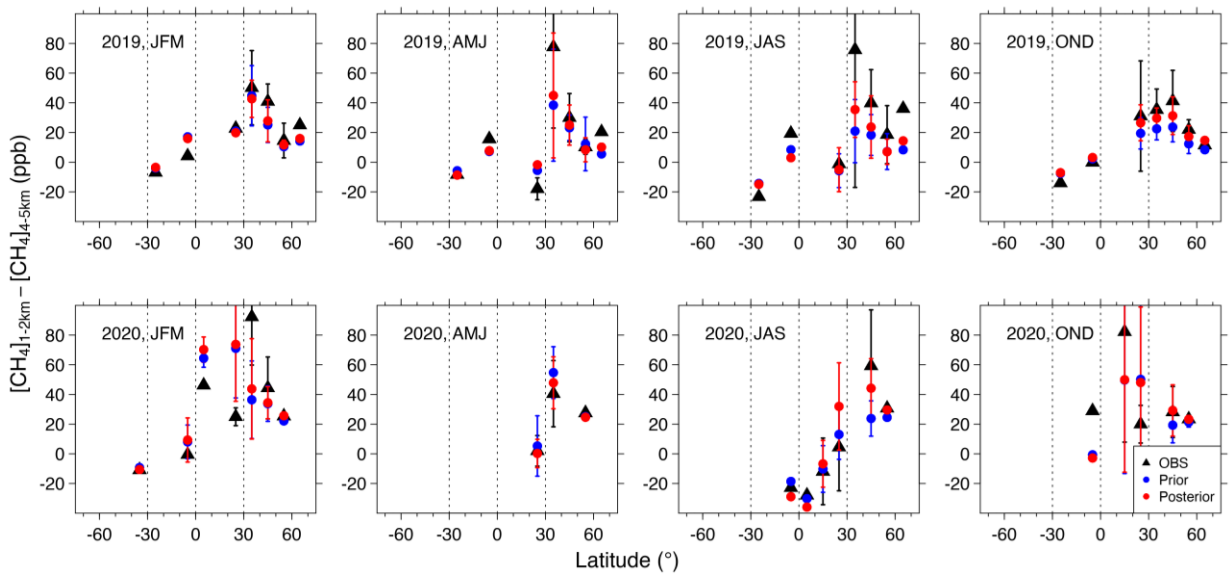

Figure 5-3 The latitudinal gradients of simulated versus observed vertical CH4 differences between 1–2 km and 4–5 km altitude bins for January–March (JFM), April–June (AMJ), July–September (JAS), and October–December (OND) during 2019–2020. The CH4 vertical profiles were obtained from various aircraft sampling networks and campaigns (see Fig 4.1 for locations of sampling sites). For each panel, the simulated or observed vertical CH4 differences across sampling sites were averaged by latitude bands of 10°. Error bars denote one standard deviation of the estimates across sites within a latitude band.

Figure 5-4 shows a comparison for CH4 vertical profiles up to 25 km between Aircores and the model simulations with the LMDZ INCA model prescribed with prior fluxes and with optimized fluxes after assimilation of GOSAT XCH4 and in-situ stations data for the years 2019 and 2020. The model was sampled at the location and time of the Aircore measurements.

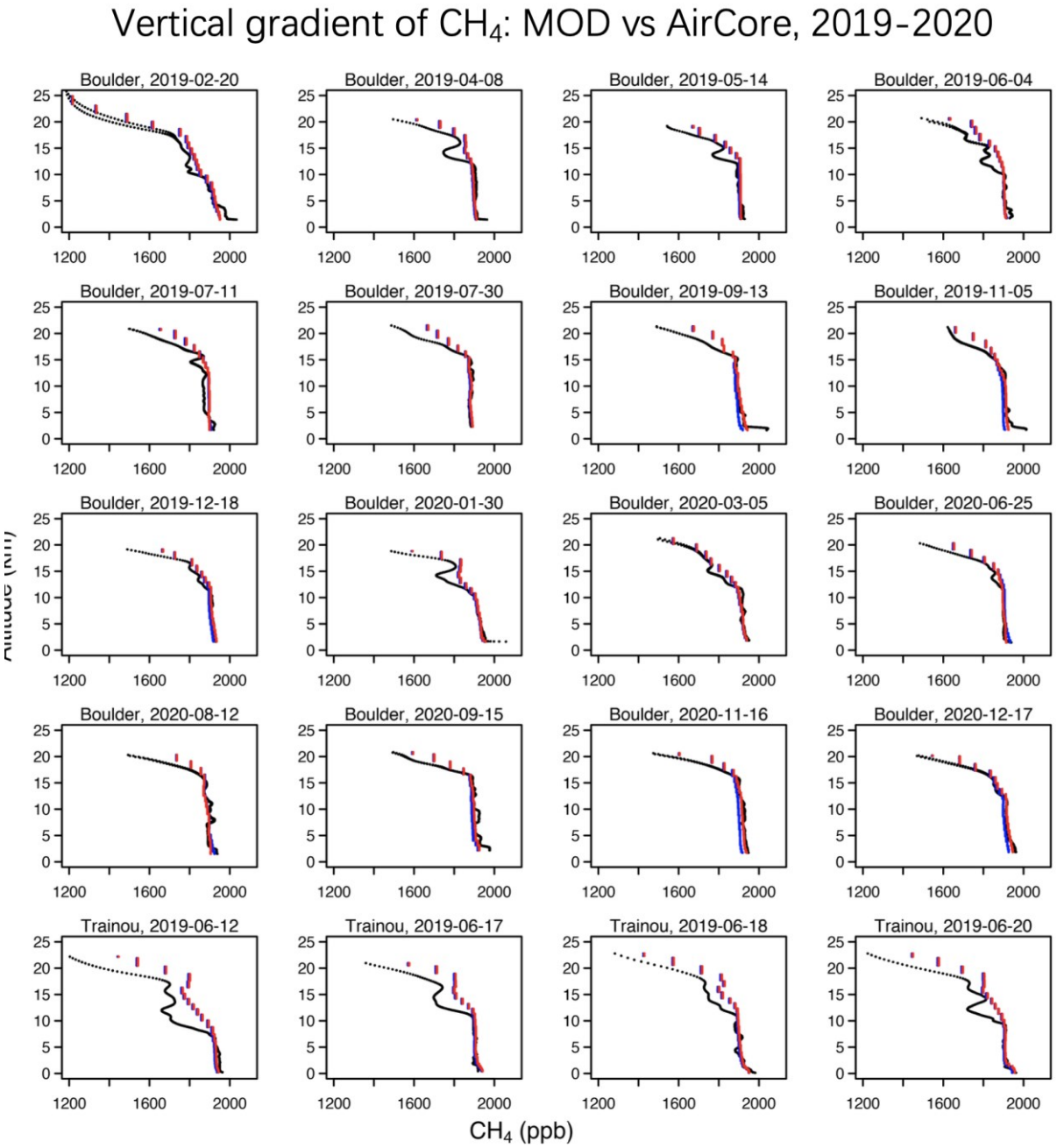

Figure 5-4 Comparison of vertical CH4 profiles in the troposphere and lower stratosphere between in-situ Aircore sampling (black points) and the simulations of the LMDZ INCA model

The results shown in indicate no systematic bias of the model but significant deviations in the stratosphere due to the limited vertical resolution of the model and possibly unresolved transport processes in the stratosphere, a bias that should not impact the diagnostic of surface fluxes. Taking further advantage of the availability of a long time series of Aircores measurements at Boulder (NOAA) Colorado, we also compared the model simulations with frequent Aircores data for different altitude bins in Figure 5-5. Although we observe the previous tendency to underestimate stratospheric CH4 values, the bias was small in the troposphere and the optimized simulations (red) improved the model fit to the independent Aircore time series.

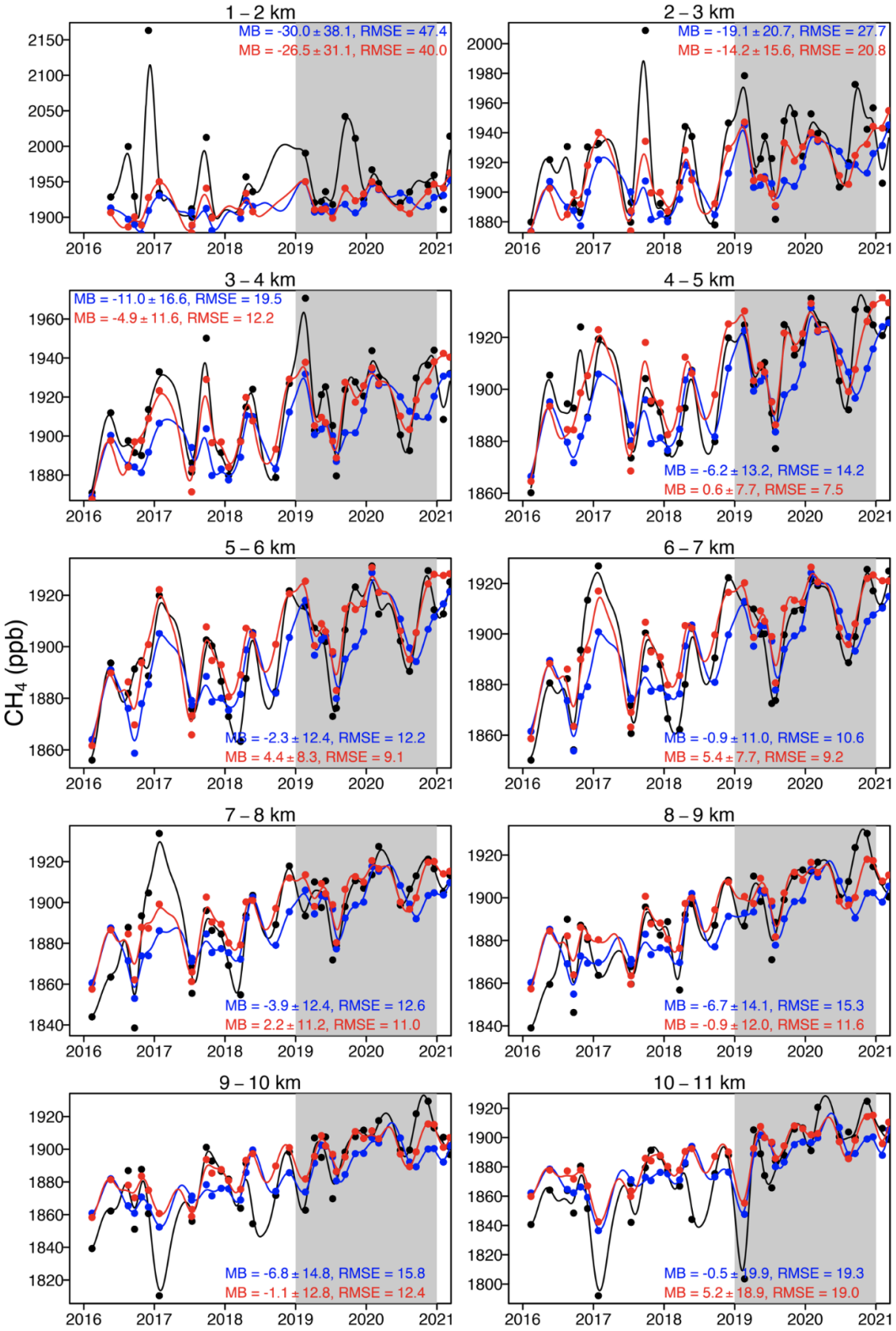

Figure 5-5 Comparison between modeled a priori (blue) and posterior optimized after GOSAT assimilation (red) concentrations against independent Aircore measurements at different altitude bins collected by Aircore data in Boulder Colorado. The grey area is the period of analysis of the WOREM project.

5.1.1. SUMMARY

Table 5-1 Inter-comparison assessment table: CH_4 - global

CH_4 – global	
Specie	CH_4
Target level region	Global
Target geographic region	Wetland emitting regions have been analyzed with ancillary data
Type of Validation	Evaluation of optimized fluxed against independent atmospheric concentration measurements : TCCON, Aircore, aircraft Comparison of wetland emissions with bottom-up ecosystem models
Parameter(s) to be validated / Test objective	the Objective of test 1 is to evaluate the concentration simulated by the 3D atmospheric model against independent observations. The Objective of test 2 is to compare with a totally independent emission estimate but we do not know which one is true
Validation description/Method	Transport simulation and sampling / comparison at atmospheric observation sites
Validation data	TCCON, Aircore, aircraft Wetland emissions from models
Time period	Since 2019
Extrapolation to other regions	atmospheric observations provide a global validation. wetland emissions have been sampled for ≈ 9 global wetland complexes
Comments	N/A
Results	The model with optimized fluxes is consistent with independent concentration data. For wetlands, the inversion gives a higher emission increase after 2019 than the wetland models

5.2. GLOBAL SOURCE INVERSIONS FOR NITROGEN DIOXIDE (NO2)

We utilized daily (as 10-day running mean) total tropospheric column densities of NO_2 over polluted regions from TROPOMI PAL (S5P) and OMI (OMNO2.003) data products to estimate anthropogenic NOx (=NO+NO_2) at 1.27°×2.5° (latitude × longitude) horizontal resolution for 2020 and 2021. In order to estimate anthropogenic NO_x over polluted grids, we adapted a specific inversion system as described in [RD.23] and mass-balance method as described in [RD.39, 40]. Here, we present the result from mass-balance method which does not consider the smearing effect i.e., one grid does not influence other. The posterior fluxes are derived by calculating two components. First, we calculated the gridded local sensitivity of concentrations due to changes in the emission which will encounter the non-linear response of NO2. Second, relative differences between observations and model simulated NO2 for a year of interest (e.g., for 2019 or 2020 or 2021). The monthly global anthropogenic emission inventories from open-source Community Emissions Data System (CEDS) [RD.25] for 2019 with a horizontal resolution of 0.5°×0.5° are used to simulate the global atmospheric NO_2 and are also considered as prior to estimate global NO_x in our inversion study.

At this stage, we compared the estimated daily (10-day running mean) anthropogenic NO_x emissions from our inversion results with bottom-up inventories i.e., CEDS.

The high-quality observations from both the satellites are utilized for estimating the anthropogenic NO_x emissions. Further, we selected polluted grids based on the criteria mentioned in previous studies [RD.29] from the satellite. Therefore, many grids are left out by imposing the selection criterion. Furthermore, we performed the inversion to estimate the total NO_x using common grids from satellite and bottom-up inventories. Finally, we scaled the unconstrained grids of region of interest by the monthly ratio of posterior and prior emission of that region.

5.2.1. COMPARING TOTAL EMISSIONS OF SELECTED REGIONS TO INVENTORIES

We compared the regional total NO_x emission constrained by total column NO2 from TROPOMI over some regions such as US, Europe, China, India, and Middle East. Figure 5-6 shows a comparison of daily (10-day running mean) total NOx from bottom-up inventories (i.e., CEDS) and estimated emission from TROPOMI for 2019 and 2020 over those selected regions. China and India contribute the largest share in total NO_x emission with an annual mean of ~ 6.38 Tg-N/year (~5.13 Tg-NO_2/year) for China and ~3.55 Tg-N/year (2.24 Tg-N/year) for India using TROPOMI (CEDS). The 2020 emission is smaller than the 2019 emission during COVID lockdown period (i.e., January-April) over China. Over US TROPOMI constrained total NO_x emissions for 2019 and 2020 showed the similar magnitude (~3.51 Tg-N/year). The estimated emission (~3.51 Tg-N/year) is large compared to CEDS inventory (~ 1.90 Tg-N/year). Both the estimated emission for 2019 and 2020 over Europe are similar trend but show large magnitude than CEDS inventory. The global annual mean 2020 emission are smaller than 2019 emission over Europe (~ -0.3 Tg-N/year). The annual mean TROPOMI constrained NO_x emission for 2020 are less than 2019 emission by ~8.39%. We computed a relative reduction of 18.76% over China during COVID lock-down period (from 23 January 2020 to 8 April 2020) compared to a 21.9% reduction was reported by [RD.23]. Over India, the TROPOMI constrained NO_x emission showed a reduction of 21.73% from 25 March 2020 to 31 May 2020.

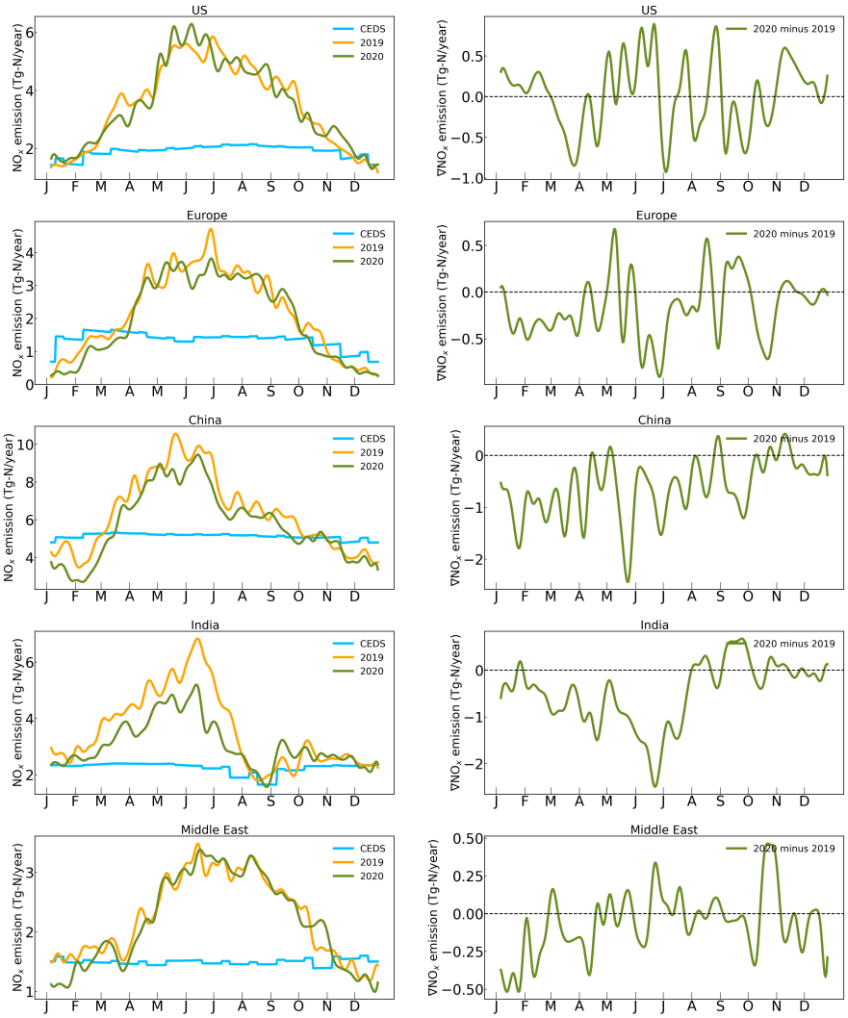

Figure 5-6 Left column: Daily time-series (10-day running mean) total constrained NOx (orange and green solid line for 2019 and 2020) over selected regions using TROPOMI observations and mass-balance method, and CEDS bottom-up inventories (blue solid line) for 2019. Right column: Daily time-series of difference between estimated fluxes for 2020 and 2019 from mass-balance method.

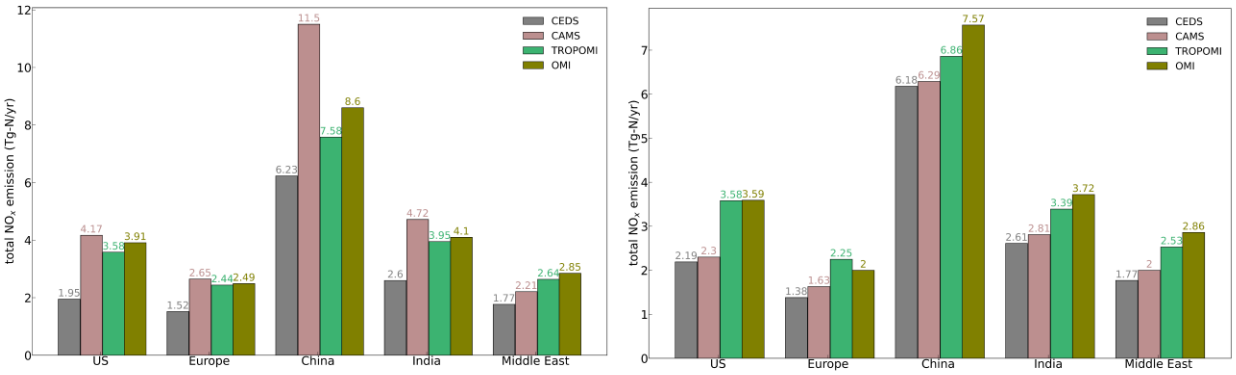

Figure 5-7 Annual mean NOx fluxes for CEDS, CAMS, TROPOMI and OMI calculated over US, Europe, China, India and Middle East for (a) 2019 and (b) 2020 (unit: Tg-N/yr).

Figure 5-7 presents the comparison of annual mean prior (i.e., CEDS), estimated fluxes using TROPOMI and OMI observations, and an independent inventory (i.e., CAMS) for 2019 and 2020. The posterior emissions were about 3.58 (3.91) Tg-N/yr constrained by TROPOMI (OMI) for 2019 for US. However, TROPOMI and OMI showed a similar emission (~3.58 Tg-N/yr) over US for 2020. Moreover, the TROPOMI showed similar emission for 2020 (3.58 Tg-N/yr) as 2019. OMI showed ~9% reduction of NO_x emission during 2020 (3.59 Tg-N/yr) than 2019 (3.91 Tg-N/yr) over US. The CEDS show ~12% increase in 2020 NO_x emissions than 2019 over the same region. CAMS indicated ~45% reduction of 2020 emissions (2.3 Tg-N/yr) than 2019 (4.17 Tg-N/yr). The 2020 emission reduced by ~8% and ~20% than 2019 for TROPOMI and OMI, respectively, over Europe. The CEDS inventory indicated ~9% reduction in 2020 emission than 2019. CAMS showed total emission over Europe for 2019 and 2020 are 2.65 Tg-N/yr and 1.63 Tg-N/yr. The annual mean estimated emission for 2019 using TROPOMI and OMI are 7.58 Tg-N/yr and 8.6 Tg-N/yr, respectively, and that of for 2020 were 6.86 Tg-N/yr and 7.57 Tg-N/yr. The TROPOMI indicated relatively less emission than OMI for both the year. The 2020 emission reduced by ~10% and ~12% than 2019 for TROPOMI and OMI, respectively. CAMS showed a relatively large emission by ~52% and ~34% than the estimated total emission using TROPOMI and OMI, respectively for 2019. However, CAMS emission (6.29 Tg-N/yr) are comparable with CEDS emission (6.18 Tg-N/yr) for 2020. The TROPOMI and OMI showed similar emission over India for 2019 (~3.95-4.1 Tg-N/yr). However, CAMS indicated a ~19% and ~15% more emission in case of TROPOMI and OMI, respectively. Moreover, the CAMS emission was reduced by ~17% and ~24% in case of TOPOMI and OMI, respectively, for 2020. The annual total emission from CEDS remained same for both of the years (2019 and 2020) over Middle-East (1.77 Tg-N/yr). The CAMS and TROPOMI showed a reduction in the 2020 emission than 2019 by ~9% and ~4%, respectively. However, a similar emission (~2.85 Tg-N/yr) was estimated for both of the years (2019 and 2020) using the observation from OMI.

5.2.2.SUMMARY

Table 5-2 Inter-comparison assessment table: NO_x - global

NO_x – global	
Specie	NO_x
Target level region	Global
Target geographic region	Selected regions (US, Europe, China, India, Middle East) spread over the globe
Type of Validation	Qualitative and Quantitative
Parameter(s) to be validated / Test objective	Emission budgets at daily to monthly scale seasonal spatial distributions of emissions over the globe
Validation description/Method	Statistics of the misfits between the inversions and the inventories
Validation data	Global bottom-up inventories: CEDS
Time period	2019 - 2020

NO_x – global	
Extrapolation to other regions	Global
Comments	We may compute anthropogenic NOx emission using OMI observation and compare with TROPOMI constrained NOx emission. Further, we may utilize CAMS inventory to compare with our estimates. Furthermore, we may interpolate/extrapolate beta with some appropriate method to constrain all grids other than anthropogenic.
Results	TROPOMI based inversions of the global total NO2 emissions are consistent.

5.3. GLOBAL SOURCE INVERSIONS FOR CARBON MONOXIDE (CO)

The inversion of global CO sources has been previously evaluated against a) independent vertical profiles of CO collected by IAGOS (previously MOZAIC) aircraft (regular passenger flights) and HIPPO campaigns in the Pacific Ocean, TCCON sites and ground-based networks that were not used in the inversion of the MOPITT data, and various bottom-up inventories for anthropogenic emissions. We also performed evaluations against independent GFED inventories for fire emissions. The location of atmospheric evaluation sites is in Figure 5-8.

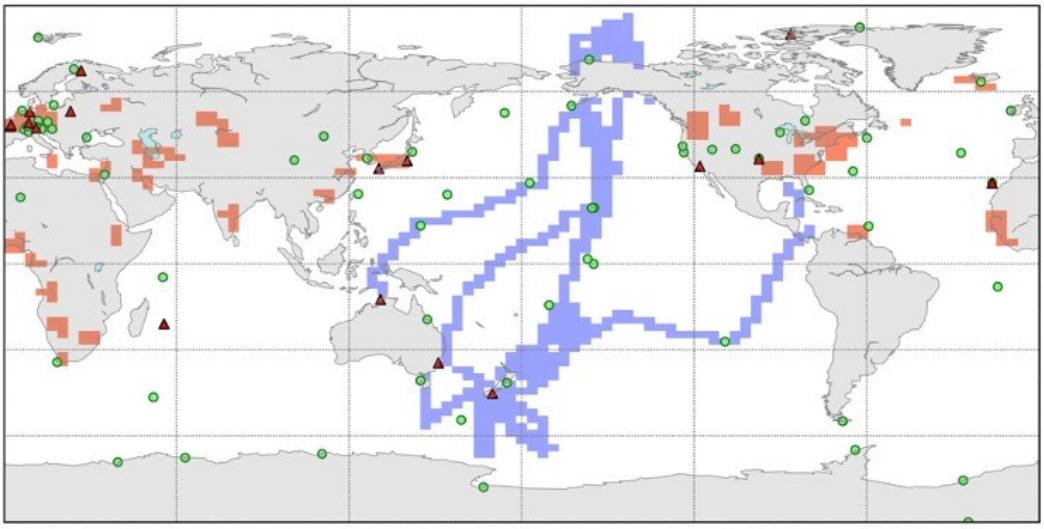

Figure 5-8 Spatial distribution of the independent measurements. The TCCON stations are shown with rectangles, the surface stations are shown in green circles, the MOZAIC quasi-profile overages are shown at the model grid in orange, the HIPPO profile coverage is shown at the model resolution in blue.

The comparison with independent CO measurements in Figure 5-9 shows a bias in the latitudinal CO gradient for different versions of the model of up to 20 ppb.

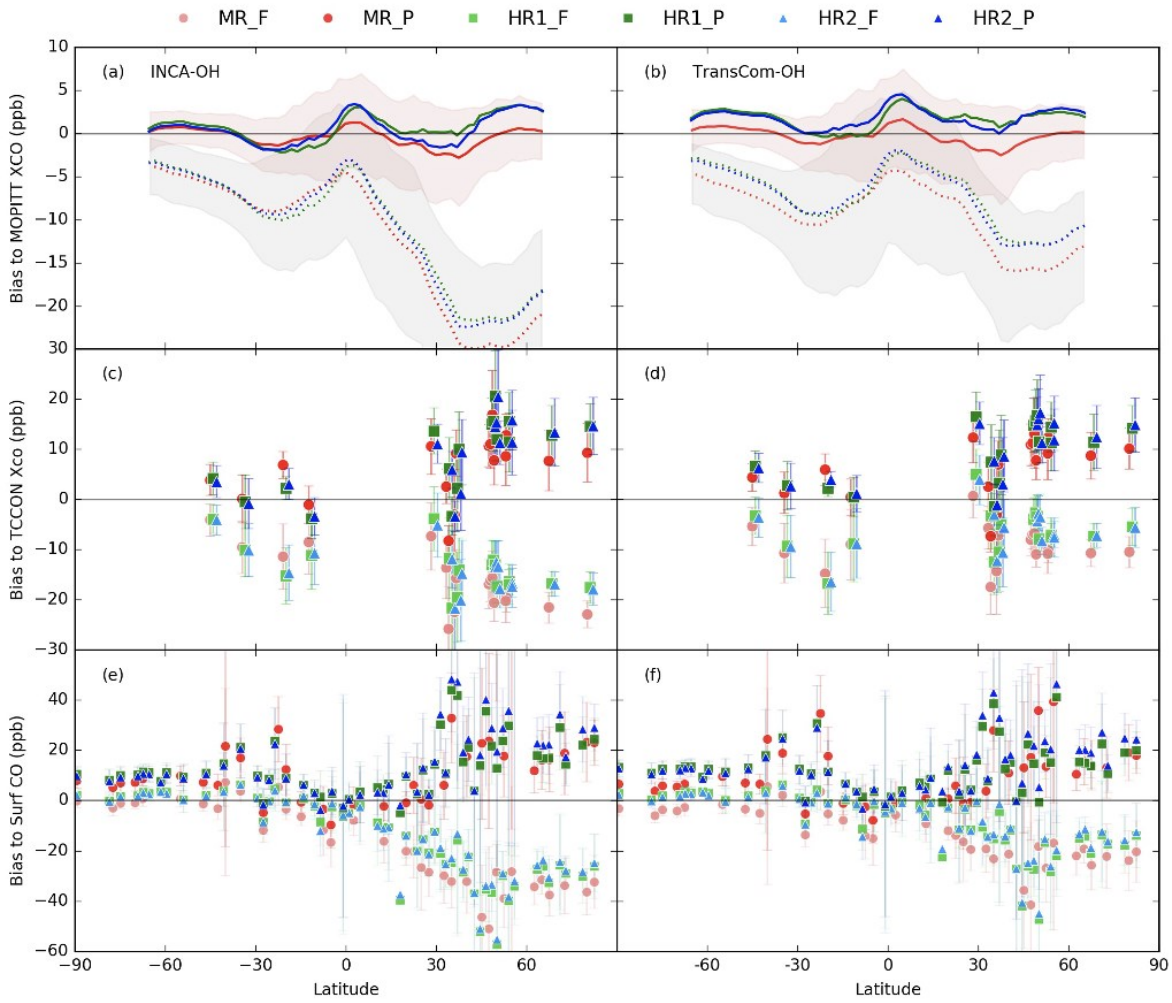

Figure 5-9 Model-data biases along the latitudes. (a) and (b) present model biases to MOPITT Xco using INCA-OH and TransCom-OH, respectively. Dashed and solid lines represent forward and posterior model results, respectively, while color codes correspond to model versions shown in the legend. (c) and (d) present model biases to TCCON Xco measurements using INCA-OH and TransCom-OH respectively. (e) and (f) show model biases compared to ground measurements from surface network using INCA-OH and TransCom-OH respectively. Note the ordinates are different for the three observation types.

Comparison with MOZAIC aircraft data show a good fit to the observations in Figure 5-10 yet an underestimation in the southern high latitudes and in the northern high latitudes for the HIPPO flights in the lower troposphere.

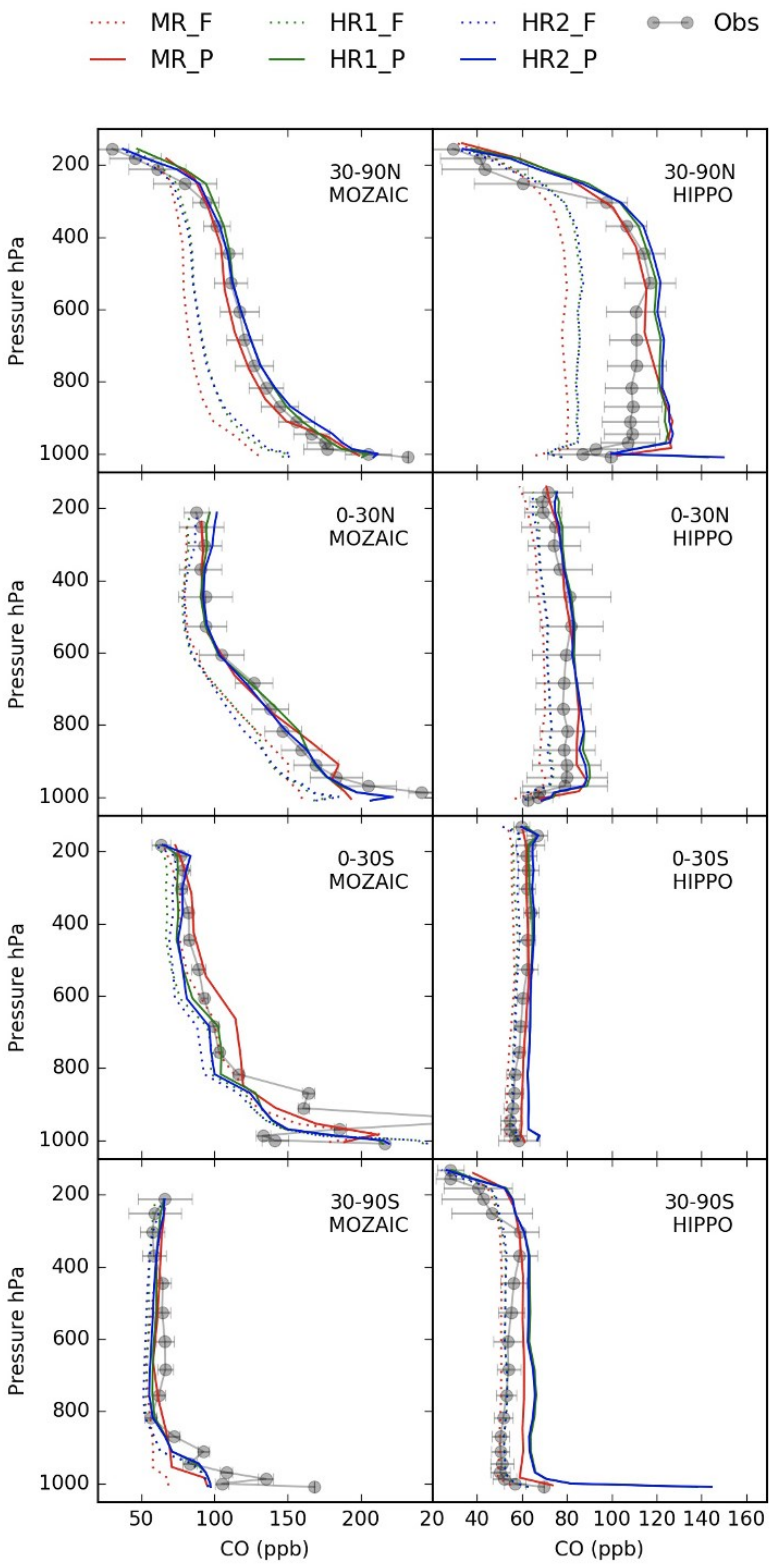

Figure 5-10 Zonal averages of the model bias in the vertical CO profiles. The left column shows results against MOZAIC measurements, and the right column shows results against HIPPO measurements. The error bars indicate the standard variation of the measurements. Results associated with INCA-OH are presented.

5.3.1. SUMMARY

Table 5-3 Inter-comparison assessment table: CO - global

CO– global	
Specie	CO
Target level region	Global
Target geographic region	The validation by atmospheric cross validation is global
Type of Validation	independent CO concentration measurements not used in the inversion: surface network, TCCON, MOZAIC passenger aircraft
Parameter(s) to be validated / Test objective	optimized CO emissions and global OH sink of CO
Validation description/Method	The transport chemistry model was run with optimized emissions and sampled at the locations of observations
Validation data	surface network, TCCON, MOZAIC passenger aircraft
Time period	Since 2000
Extrapolation to other regions	N/A
Comments	N/A
Results	The optimized model is consistent cross validation data but shows a bias with vertical profiles in particular in the southern high latitudes

5.4. GLOBAL SOURCE INVERSIONS FOR SULPHUR DIOXIDE (SO2)

We estimated daily global anthropogenic SO2 emissions at 1.27°×2.5° (latitude × longitude) spatial resolution over polluted regions for three years 2019, 2020, and 2021 using satellite SO2 total vertical column densities (TVCDs) obtained from TROPOMI-COBRA (refereed as TROPOMI afterwards) and OMI SO2 (OMSO2.003) data products. In order to estimate the anthropogenic SO_2 emissions from the satellite observations, we used a mass-balance inversion approach [RD.29] using LMDZ-INCA model simulations. The inversion approach combines the gridded local sensitivities of the TVCDs to the perturbed anthropogenic SO_2 emissions and the relative change of the observed satellites and the modelled TVCDs to derive the anthropogenic SO_2 emissions of the inversion years. We utilized monthly global anthropogenic emissions from open-source Community Emissions Data System (CEDS) for 2019 for model simulations and also as a priori for the inversions.

At this stage, our assessment of the reliability of the anthropogenic SO2 emission estimates is based:

1) on comparisons to two global bottom-up inventories of the SO2 anthropogenic emissions (i) CEDS, which is used as a basis for the inversions, and (ii) CAMS, which is an independent emissions estimates; this comparison is indicative of the reliability of the amplitude of the departure from the CEDS inventory to better fit the satellite data

2) on comparisons between inversions based on the TROPOMI and OMI data, checking the consistencies between the emission estimates from the two sets of inversion at large scale; this comparison gives indications on the level of robustness and consistency of the constraint from the different satellite datasets

For the inter-comparisons, we re-gridded the global anthropogenic SO2 emission from the bottom-up inventories on the grids (1.27°×2.5°) of the estimated emission. We used a minimum 10-days threshold to calculate the monthly emissions from the daily estimated SO2 emissions from the inversions. As we utilize only the high-quality observations from the satellite retrievals and some of the grids are also discarded based on some filtering criteria for the anthropogenic emissions and to avoid extreme or negative unrealistic estimates from the inversions, we leave many grids where we do not have the satellite observations constrained emissions from the inversions. Therefore, for this preliminary comparison analysis, we sub-sampled the emissions from the bottom-up inventories on the common grids corresponding to the satellite observations constrained emissions only.

5.4.1. COMPARING TOTAL EMISSIONS TO INVENTORIES

We first inter-compared the daily anthropogenic SO2 emissions derived from the inversions of two different satellites SO2 data products TROPOMI and OMI for three years, 2019, 2020 and 2021. Figure 5-11 shows a comparison of TROPOMI and OMI constrained SO2 emissions over selected regions. As OMI constrained emission estimates has comparatively smaller global coverage compared to the TROPOMI after applying different filtering criteria on TVCDs and gridded local sensitivity of concentrations to emission changes (β) in inversions, for this comparison, we sub-sampled the daily emissions on common grids where the estimates from both the TROPOMI and OMI observations are available. These sub-sampled estimates are also compared with the corresponding bottom-up anthropogenic SO2 emissions from CEDS inventory (). The daily variation of the estimated emissions from both the TROPOMI and OMI retrievals are consistent to each other. For example, TROPOMI and OMI constrained annual emissions over Indian region in 2019, 2020 and 2021 differ by only ~2% to ~5% .

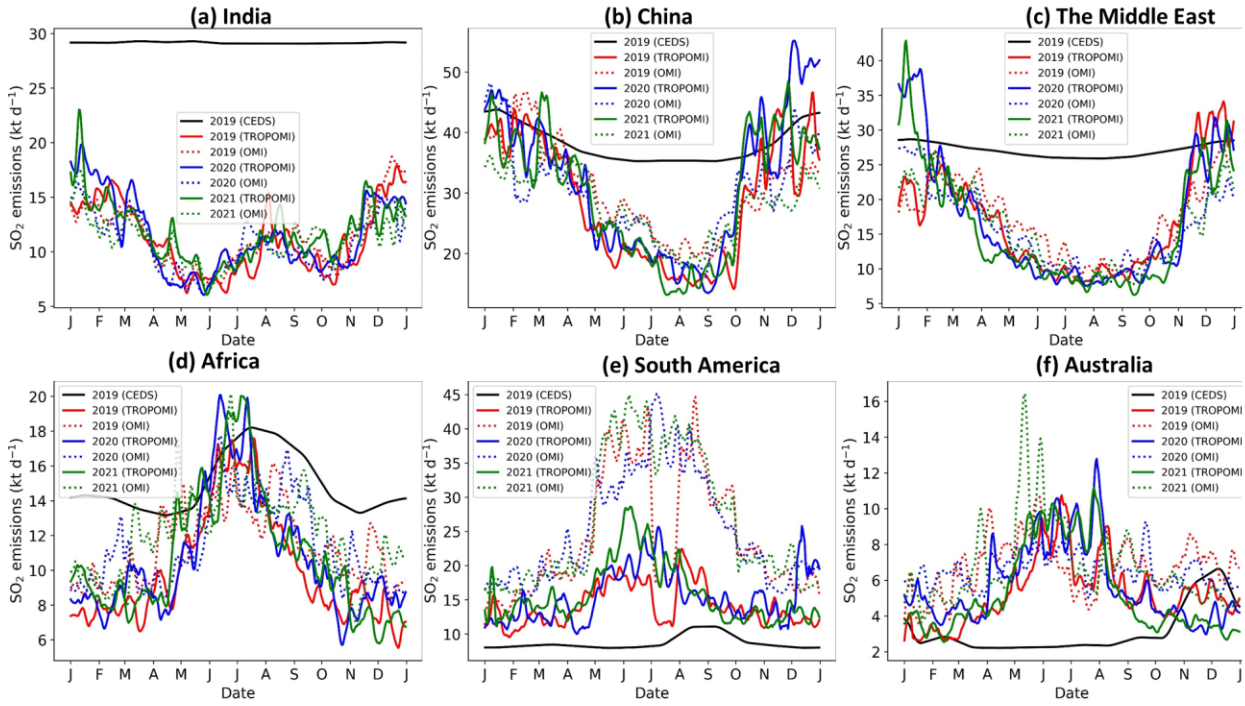

Figure 5-11: Comparison of the daily variation of the estimated anthropogenic SO2 emissions over selected regions (sub-sampled on the common grids) using TROPOMI and OMI observations for 2019, 2020, and 2021.

Figure 5-12 shows a comparison of the monthly global anthropogenic SO2 emissions aggregated from the daily estimates using TROPOMI and OMI retrievals with the monthly CEDS and CAMS bottom up SO2 anthropogenic emissions sub-sampled on the common grids for 2019, 2020, and 2021. TROPOMI constrained annual global anthropogenic SO2 emissions are ~14%, ~10%, and ~12% smaller for 2019, 2020, and 2021, respectively compared to the CEDS emissions (~24%, ~20% and ~16% smaller for 2019, 2020, and 2021 respectively compared to the CAMS emissions). For OMI, the annual global constrained emissions are comparable for all years compared to the CEDS emissions and 8%, ~11%, and ~4% smaller for 2019, 2020, and 2021, respectively compared to the CAMS emissions. TROPOMI constrained annual global emissions for 2019, 2020 and 2021 are respectively ~17%, ~9%, and ~13% smaller compared to the OMI estimates. In Figure 5-13, spatial distributions of seasonal estimated emissions are compared with the CEDS and CAMS emissions. In winter months and at higher latitudes regions, we have smaller number of good quality satellite observations to constrain the emissions from inversions. Therefore, the smaller global emissions during winter months are mainly due to relatively smaller number of TROPOMI and OMI constrained emissions.

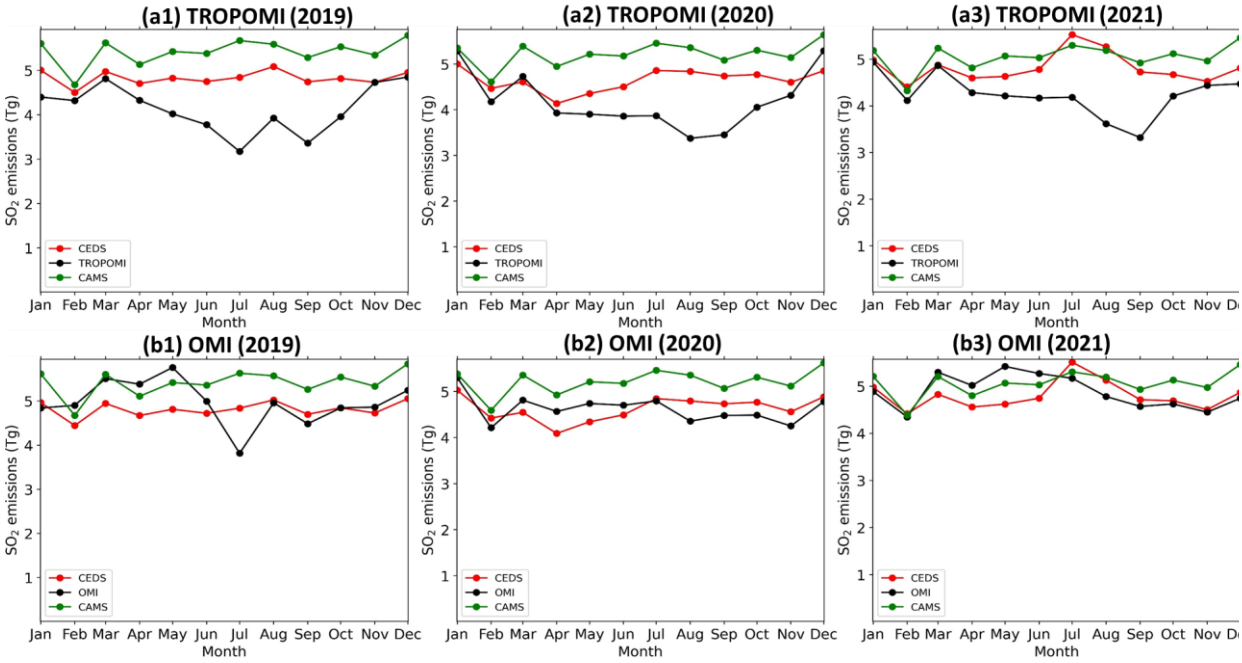

Figure 5-12: Comparison of the monthly global estimated anthropogenic SO2 emissions over the land using TROPOMI ((a) and (b)) and OMI ((c) and (d)) observations with the emissions from CEDS and CAMS bottom-up inventories sub-sampled on the common grids for 2020 and 2021.

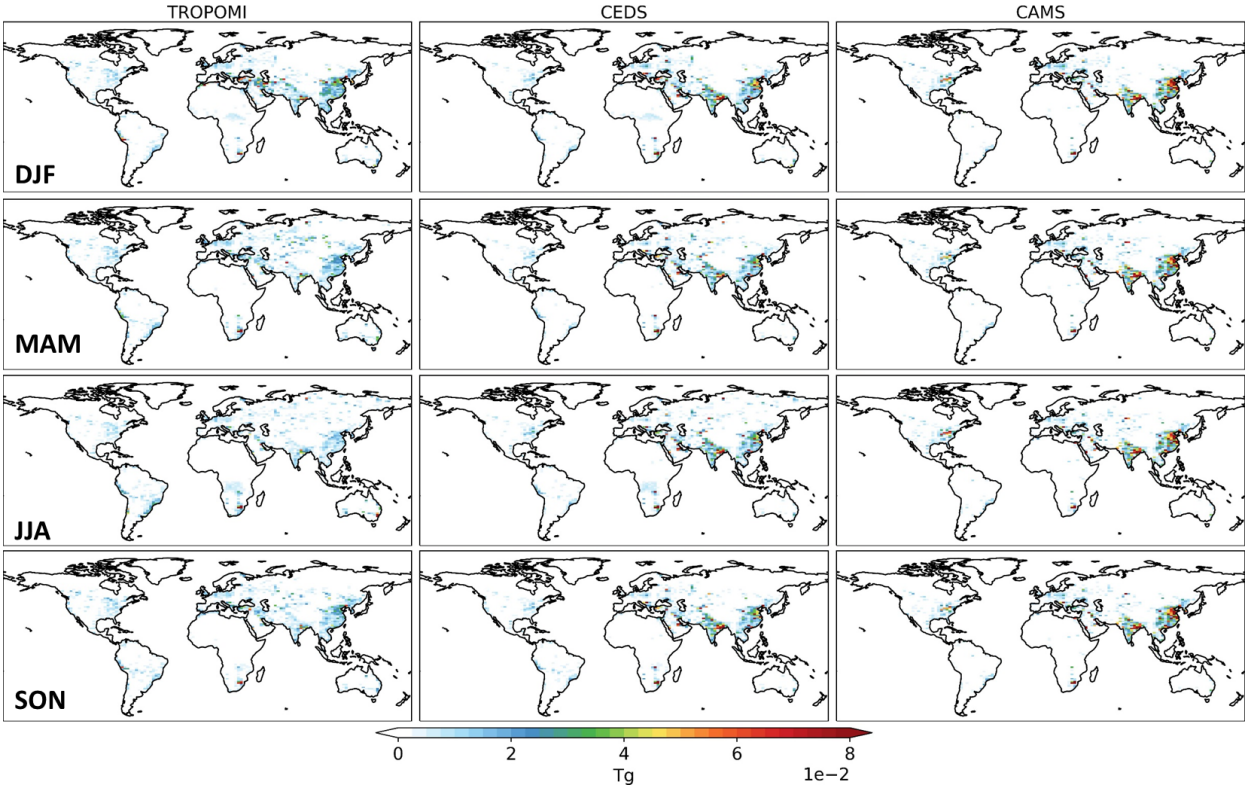

Figure 5-13: Spatial distribution of the seasonal anthropogenic SO2 emissions over the land estimated using the TROPOMI observations (left), and the corresponding sub-sampled emissions on the common grids from the CEDS (middle) and CAMS (right) bottom-up inventories for 2020.

5.4.2. COMPARING TOTAL EMISSIONS OF SELECTED REGIONS TO INVENTORIES

We compared the regional TROPOMI and OMI constrained anthropogenic SO2 emissions with the bottom-up emissions over the polluted regions China, India, the Middle East, Africa, South America and a lesser polluted region Australia. Figure 5-14 shows a comparison of the monthly TROPOMI constrained and bottom-up emissions over these regions and an inter-comparison of the annual regional emissions for each year is shown in Figure 5-14. Constrained SO2 emissions for Indian region (~4 Tg) is smaller compared to the CEDS and CAMS emissions. China and the Middle East account for the largest anthropogenic sources of SO2, with annual TROPOMI constrained emissions of ~10-11 Tg for China, and ~6 Tg for the Middle East. The annual TROPOMI constrained SO2 emissions for Africa, South America, and Australia are respectively ~4 Tg, ~5 Tg, and ~2 Tg for each year. The OMI constrained emissions for each region are comparable to the TROPOMI, except for South America where the OMI constrained emissions are larger than the TROPOMI. TROPOMI and OMI constrained monthly and annual regional SO2 emissions are mostly smaller compared to the CEDS and CAMS bottom-up emissions over India, China, the Middle East, and Africa (Figure 5-15), except for South America and Australia.

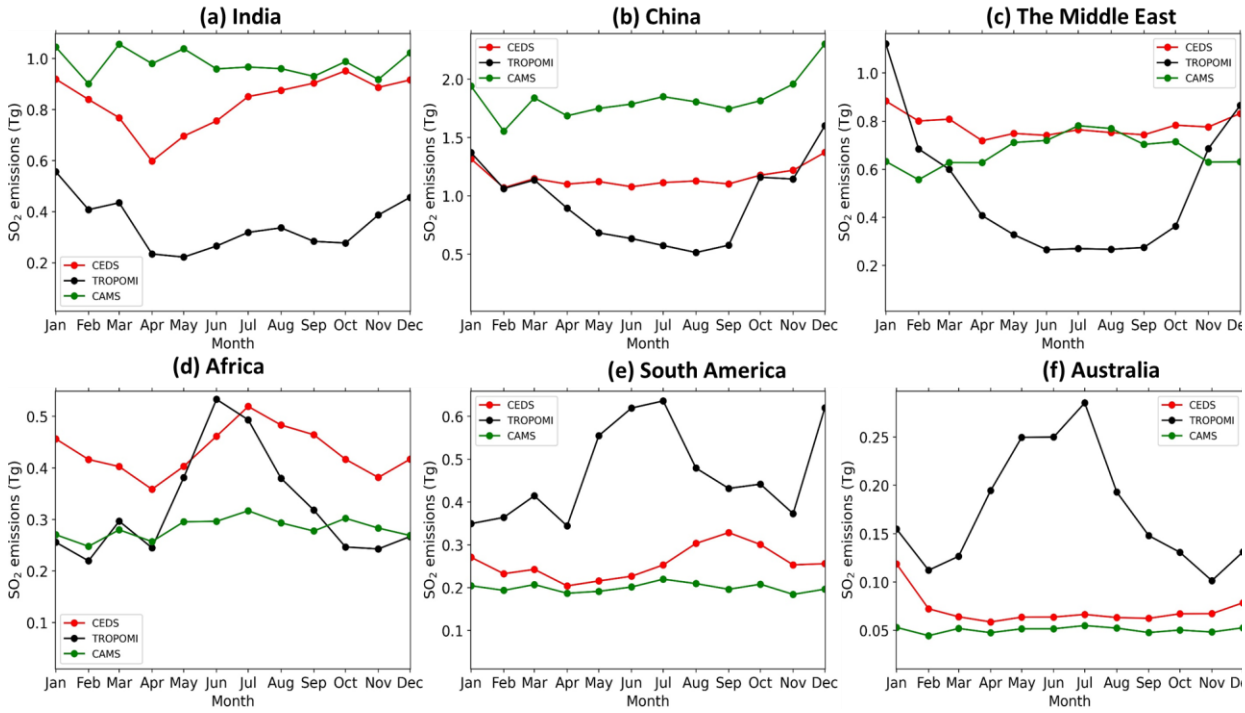

Figure 5-14: Comparison of the monthly regional estimated anthropogenic SO2 emissions over the land using TROPOMI observations with the emissions from CEDS and CAMS bottom-up inventories sub-sampled on the common grids for 2020.

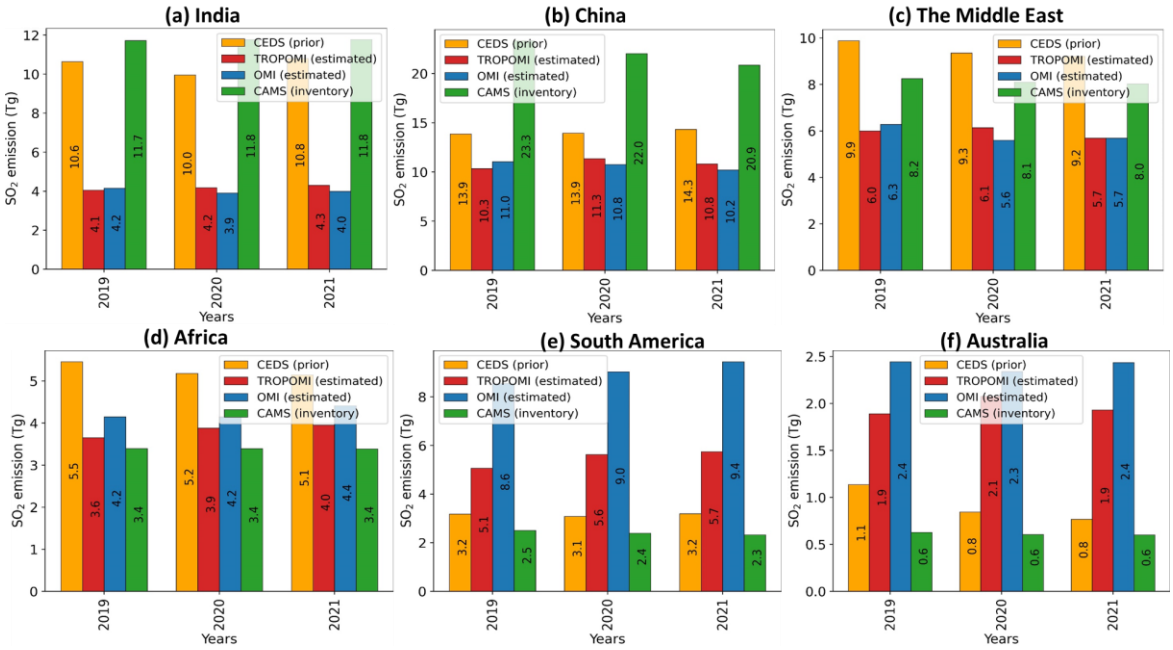

Figure 5-15: Comparison of the annual regional anthropogenic SO2 emissions estimated using TROPOMI ((a) and (b)) and OMI ((c) and (d)) observations with corresponding sub-sampled emissions on the common grids from the CEDS and CAMS bottom-up inventories for, 2019, 2020 and 2021.

5.4.3 Comparison of constrained emissions with the Catalogue point sources emissions.

We compared the TROPOMI and OMI constrained annual gridded SO_2 emissions with the collocated point source emissions from a catalogue reported by [RD.42] over the South Asia region (India, Pakistan, Bangladesh, Sri Lanka) for three years from 2019 to 2021. Figure 5-16 shows a comparison of these SO2 emissions with the catalogue emissions. The Pearson correlation coefficients between the TROPOMI constrained and the catalogue point sources emissions are found 0.59, 0.63, and 0.66 for 2019, 2020, and 2021, respectively. A similar order of correlation coefficients values was found between OMI constrained and catalogue point source emissions. The TROPOMI (OMI) constrained emissions are ~5% (~7%), ~14% (~5%), and ~15% (~4%) higher compared to the total co-located catalogue point source emissions over the South Asia region for 2019, 2020, and 2021, respectively. Overall, the annual TROPOMI and OMI constrained emissions corresponding to the collocated point sources agree well with the total point source emissions from the catalogue. We also compared our constrained emissions with the co-located catalogue point source emissions for other regions and our constrained emissions are mostly in good agreement with the point source emissions.

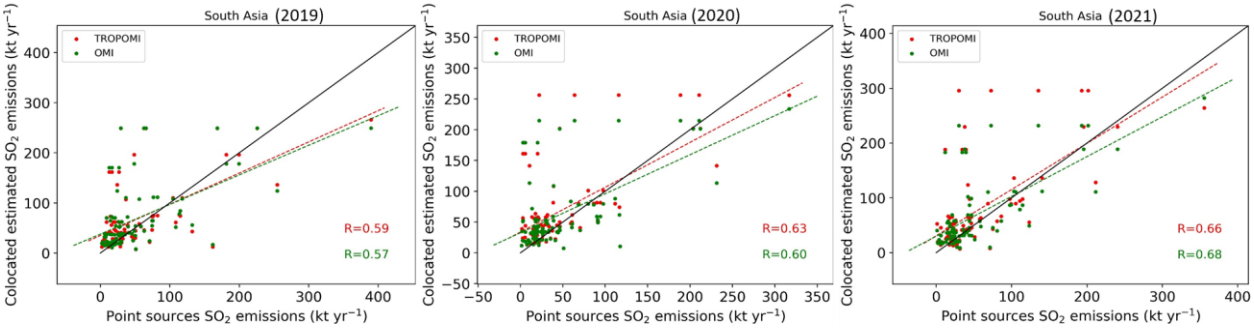

Figure 5-16: A comparison of TROPOMI and OMI constrained SO2 emissions with the co-located point source emissions from a catalogue reported in [RD.42].

5.4.3. SUMMARY

Table 5-4 Inter-comparison assessment table: SO_2 - global

SO_2 – global	
Specie	SO_2
Target level region	Global
Target geographic region	China, India, the Middle East, Africa, South America, Australia
Type of Validation	Qualitative and Quantitative
Parameter(s) to be validated / Test objective	Emission budgets at daily to annual scale seasonal spatial distributions of emissions over the glob
Validation description/Method	Statistics of the misfits between the inversions and the inventories
Validation data	Global bottom-up inventories: CAMS, CEDS
Time period	2019-2021
Extrapolation to other regions	No
Comments	
Results	TROPOMI and OMI based inversions of the global anthropogenic SO2 emissions are consistent. Comparing the constrained emissions to the emissions from the point sources catalog instils confidence in the constrained emissions.

5.5. GLOBAL SOURCE INVERSIONS FOR AMMONIA (NH3)

We estimated daily global anthropogenic NH3 emissions at 1.27°×2.5° (latitude × longitude) spatial resolution over polluted regions for two years 2020 and 2021 using NH3 total vertical column densities (TVCDs) obtained from IASI V3R.1.0 NH3 data product. For daily global NH3 inversions, we used the same approach as used for the global NOx and SO2 inversions. At this stage, we validate the estimated anthropogenic NH3 emissions from our preliminary inversion results with two monthly global anthropogenic NH3 emissions bottom-up inventories (i) CEDS, and (ii) CAMS. For the inter-comparison analysis, we used the same approach as used for the global anthropogenic SO2 emissions.

Figure 5-17 shows daily variation of the IASI constrained NH3 emissions over the selected regions India, China, Africa, Europe, South America, and North America. Over the years, the IASI constrained NH3 emissions mostly follow similar seasonality over each selected region. Over Indian and China regions, the seasonally of the constrained NH3 emissions are different from the bottom up CEDS emissions. For other regions, the constrained emissions almost follow CEDS seasonally. The constrained emission for each region is higher than the bottom up CEDS emissions.

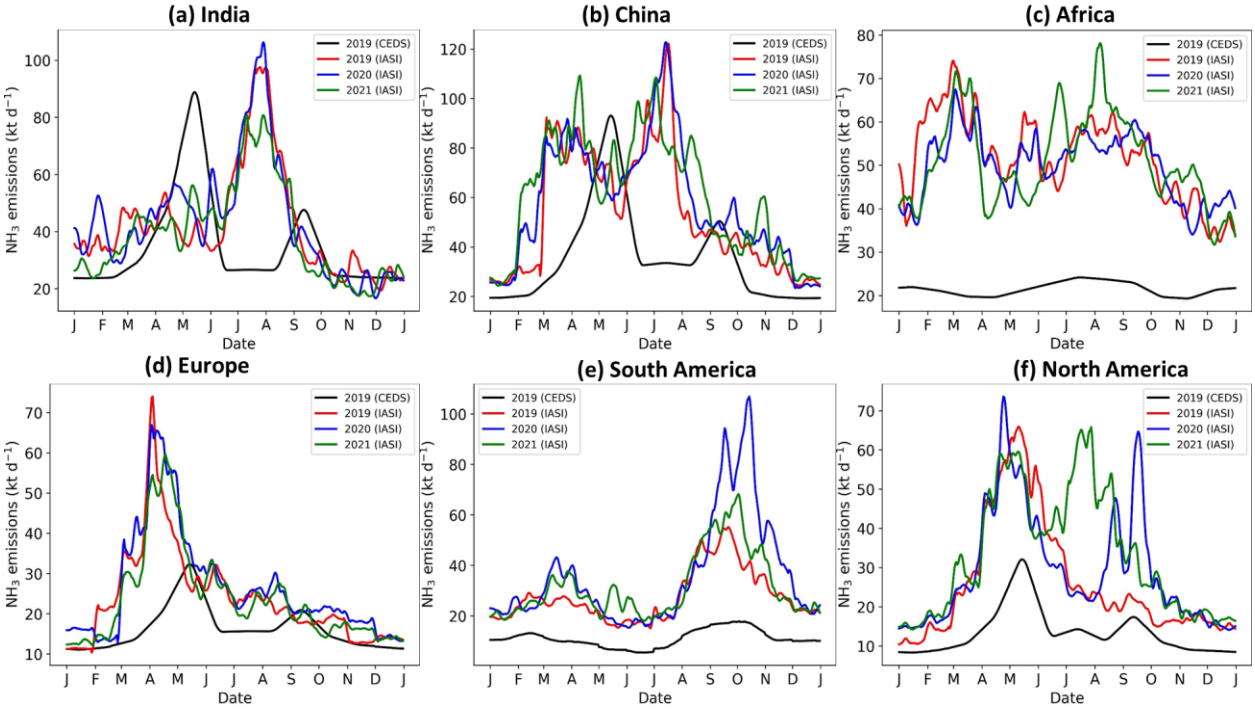

Figure 5-17 Daily variation of the IASI constrained NH3 emissions over the selected regions for 2019, 2020, and 2021.

5.5.1. COMPARING TOTAL EMISSIONS TO INVENTORIES

Figure 5-18 shows the monthly global anthropogenic NH3 emissions aggregated from the daily estimates from the inversions using IASI observations for three years, 2019, 2020 and 2021. The estimated NH3 emissions show high emissions in April/May and August/September compared to other months for each inversion years. These monthly estimated emissions are compared with the monthly global anthropogenic NH3 emissions from CEDS and CAMS bottom-up inventories sub-sampled on the common grids (Figure 5-18). The annual IASI constrained global NH3 emissions over the land are estimated ~89 Tg, ~94 Tg, and ~ 94 Tg for 2019, 2020 and 2021, respectively. These estimated annual global NH3 emissions for 2019, 2020, and 2021 are ~65% (~119%), ~78% (~131%), and ~71% (~129%) higher compared to the CEDS (CAMS) emissions, respectively.

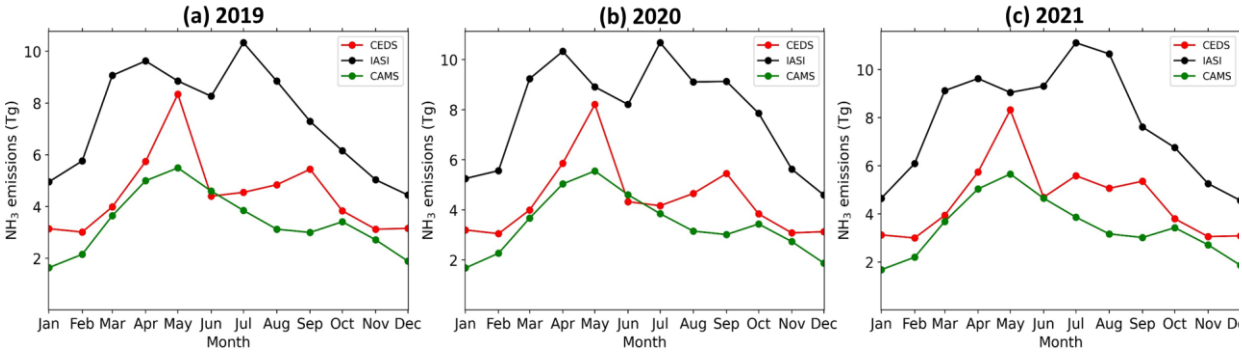

Figure 5-18: Comparison of the monthly global estimated anthropogenic NH3 emissions over the land using IASI observations with the emissions from CEDS and CAMS bottom-up inventories sub-sampled on the common grids for 2019, 2020, and 2021.

Figure 5-19 shows the spatial distribution of the seasonal IASI constrained anthropogenic NH3 emissions over the land and comparisons with the CEDS and CAMS emissions for 2020. The spatial distributions clearly show high ammonia emissions over the Indian and China regions which contribute

to a majority of the total global anthropogenic ammonia emissions. The estimated emissions are higher in March April May (MAM) and JJA compared to the other seasons which also agree with the CEDS and CAMS bottom-up emissions.

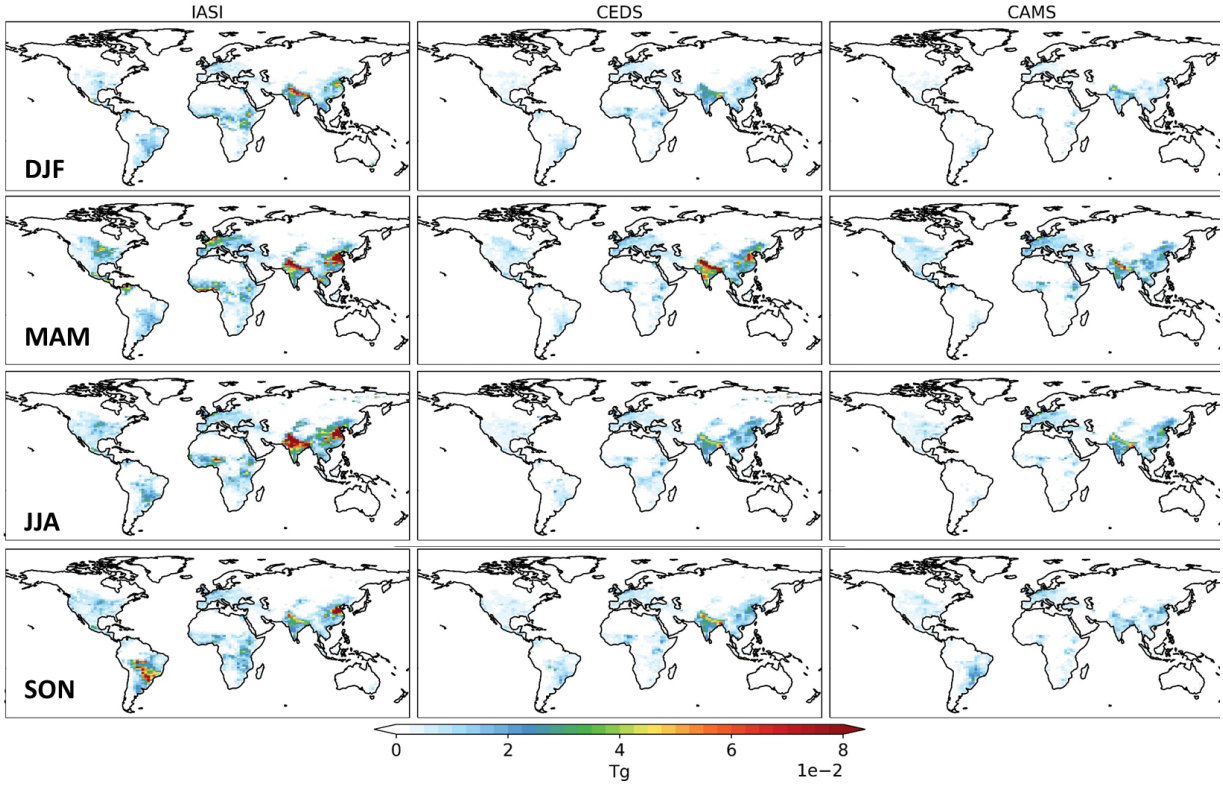

Figure 5-19: Spatial distribution of the seasonal global anthropogenic NH3 emissions over the land estimated using the IASI observations (left), and the corresponding sub-sampled emissions on the common grids from the CEDS (middle) and CAMS (right) bottom-up inventories for 2020.

5.5.2. COMPARING TOTAL EMISSIONS OF SELECTED REGIONS TO INVENTORIES

We selected major polluted regions India and China, and other regions Europe, Africa, North America and South America over the glob to analyse and compare the regional anthropogenic NH3 emissions for 2019, 2020 and 2021. Figure 5-20 shows the monthly IASI constrained NH3 emissions compared with the CEDS and CAMS emissions. Most of these selected regions shows two seasonal peaks, except for the African regions where the seasonal variation is less visible from the estimated and CEDS emissions (Figure 5-20). Annual anthropogenic emissions for the selected regions are shown in Figure 5-20. India and China contribute a majority of the total global ammonia emissions (mainly crop-specific emissions). For India (and China), the annual global IASI constrained anthropogenic NH3 emissions are ~16 Tg (~20 Tg), and ~16 Tg (~21 Tg), and ~14 Tg (~19 Tg) for 2019, 2020, and 2021. Compared to the CEDS emissions, the annual estimated emissions for India (and China) are higher respectively with ~21% (~50%), ~25% (~64%), and ~12% (~71%) for 2019, 2020, and 2021, respectively. For each inversion years, CAMS emissions are smaller compared to the CEDS for both India and China, and thus, we have even larger difference between the estimated and the CAMS emissions compared to the CEDS. The constrained NH3 emissions over Africa and South America regions are much higher than the CEDS and CAMS emissions. NH3 emissions from Biomass burning may be more contributing factor for the higher emissions over these regions and it needs to analyse further.

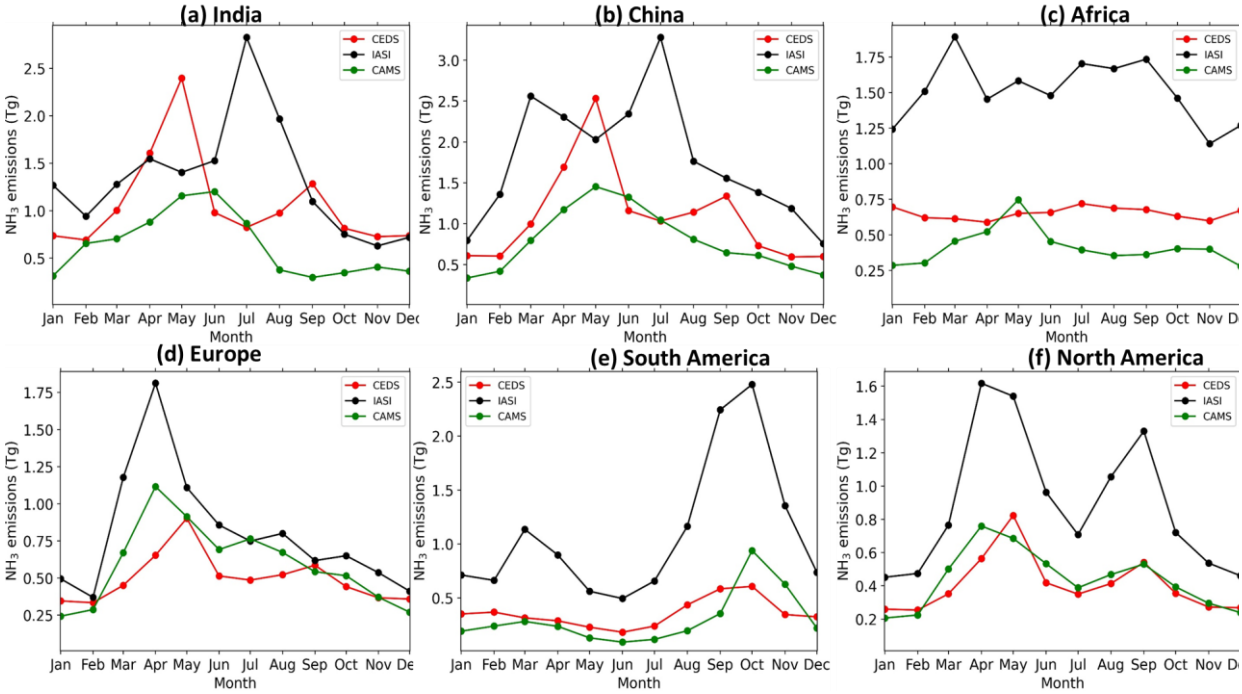

Figure 5-20: Comparison of the monthly regional estimated anthropogenic NH3 emissions over the land using IASI observations with the emissions from CEDS and CAMS bottom-up inventories sub-sampled on the common grids for 2020.

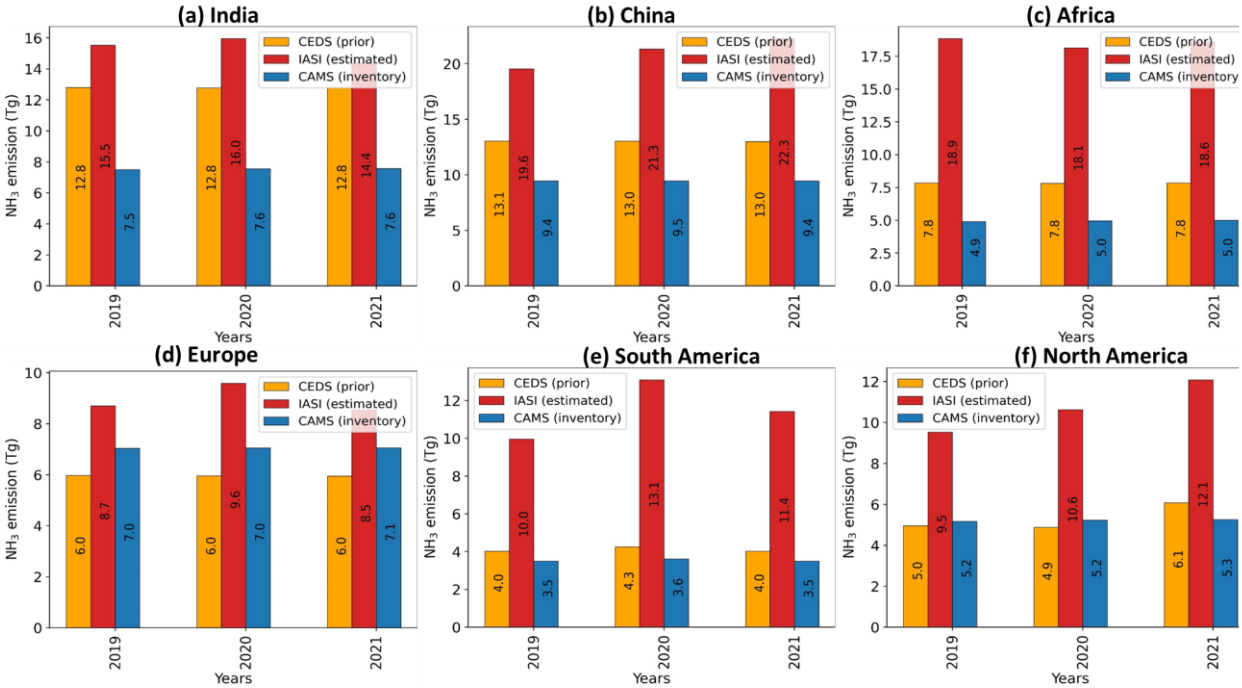

Figure 5-21: Comparison of the annual regional anthropogenic NH3 emissions estimated using IASI observations with corresponding sub-sampled emissions on the common grids from the CEDS and CAMS bottom-up inventories for 2020 and 2021.

5.5.3. SUMMARY

Table 5-5 Inter-comparison assessment table: NH_3 - global

NH_3 – global	
Specie	NH3
Target level region	Global
Target geographic region	India, China, Europe, Africa, North America, South America
Type of Validation	Qualitative and Quantitative
Parameter(s) to be validated / Test objective	Emission budgets at monthly to annual scale, seasonal spatial distributions over the glob
Validation description/Method	Statistics of the misfits between the inversions and the inventories
Validation data	Global bottom-up inventories: CAMS, CEDS
Time period	2019-2021
Extrapolation to other regions	NO
Comments	Current version of the IASI observations has higher noise in some regions which may led to the higher IASI constrained anthropogenic NH3 emissions and we may require to use some more post filtering criteria to the dataset to reduce the noise. We will use a new IASI NH3 version (v4), which also include the averaging kernel, for better constrain the NH3 emissions. Also, an appropriate gap-filling approach may need to apply to the unconstrained emissions unseen by the satellite observations.
Results	IASI constrained annual global anthropogenic NH3 emissions are higher compared to the emissions from CEDS and CAMS bottom-up inventories for all years, 2019, 2020 and 2021. Regional annual estimated emissions are also higher compared to the CEDS and CAMS. India and China contribute a majority of the total global anthropogenic NH3 emissions, and the other selected regions Europe, Africa, North America, and South America have a similar order of the magnitude of the estimated anthropogenic NH3 emissions.

END OF DOCUMENT

